Characterizing the relative biologic effectiveness following clinical and space-relevant ionizing radiation exposures and exploring curcumin nanoparticles as effective radiological countermeasures

By

ANGELA CLARE EVANS
DISSERTATION

Submitted in partial satisfaction of the requirements for the degree of

DOCTOR OF PHILOSOPHY

in

Pharmacology and Toxicology

in the

OFFICE OF GRADUATE STUDIES

of the

UNIVERSITY OF CALIFORNIA

DAVIS

Approved:

Matthew Coleman, Chair

Laura Van Winkle

Kermit Carraway

Committee in Charge

2022

Acknowledgements and Dedication

Firstly, I would like to thank my major professor, Dr. Matthew Coleman, for the opportunity to work on this dissertation project in his labs at both the University of California Davis in Sacramento, California, as well as the Lawrence Livermore National Laboratory (LLNL) in Livermore, CA. I am forever grateful for the opportunity to embark on this exciting research journey, and I will carry the skill sets and knowledge I have learned at UC Davis and LLNL with me for the rest of my life. Thank you for being an amazing mentor and for always looking out for my best interest.

Thank you also to Dr. Paul Wilson for being an encyclopedia of knowledge that I could always refer to for guidance on anything radiation-related, as well as the fun times and great food experiences during our travels to the Nasa Space Radiation Laboratory.

Thank you to Dr. Lissette Andrés, a patient and kind mentor from my undergraduate days at UC Berkeley, who inspired me pursue a Ph.D. and never give up. I am lucky to have you as a friend to this day.

I would also like to thank Dr. Kelly Martin, Dr. Wei He, Dr. Aimy Sebastian, and Dr. David Edmondson for your support and guidance with experimental setups and analyses. Your positive attitudes kept me enjoying the ride.

Furthermore, to Mr. Jordan, who has been there for me through it all, thank you for your endless support and words of encouragement.

Finally, to my mom, Mary, my dad, Lou, and by brother, Matthew, thank you all for your dedication and support over the years and for believing in me as I continue to push through each milestone in life. Thank you for inspiring me to achieve big things and to never give up.

Permission to Release to External Audiences

LLNL grants permission for this dissertation to be released to - External Audience (Unlimited).

IM release number is: LLNL-TH-834343

Table of Contents

Abstract

Ionizing radiation (IR) exposures accumulated throughout one's lifetime can lead to acute or latent toxicities, such as hematopoietic system depletion, leaky gut syndrome, as well as cancer. It is known that the biological effects following IR exposures depend on several factors, including the route of IR exposure (internal versus external), the rate of dose accumulation, as well as the type or quality of IR exposed. Currently, there remains a need to better understand the biological impact following various qualities of IR exposures and develop countermeasures to mitigate against IR-induced toxicities. Throughout this dissertation, IR exposures will be discussed in two formats: clinical and environmental. I will first describe ^{131}I-mIBG, an internalized radioactive iodine isotope that delivers targeted radiation therapy to children with high-risk neuroblastoma. I will then utilize gene expression fluctuations within this clinical study as a model for internalized ^{131}I exposures in children for purposes of biodosimetry, dose estimation, as well as developing potential biomarkers of patient toxicity and outcome. Secondly, I will introduce the production and characterization of nanolipoprotein particles (NLPs) loaded with curcumin as a potential countermeasure against clinical IR exposures. Thirdly, I will apply curcumin NLPs to human cell cultures and test their effectiveness as pharmaceutical countermeasures against both low and high doses of IR exposures, especially those IR qualities relevant to the deep space flight environment. Throughout this dissertation, transcriptomics will be utilized to reveal gene expression fluctuations and address biological pathway alterations following both internal and external IR exposures in humans or human cell model systems. Furthermore, this dissertation will introduce curcumin NLPs as promising countermeasures that may protect or mitigate against IR-induced toxicities in humans.

List of Figures

Chapter 1

Chapter 2

List of Tables

Chapter 1: Introduction

1.1 Radiation (Ionizing and Non-Ionizing)

Radiation, the emission or transmission of energy through matter, presents in the form of waves or particles and consists of non-ionizing and ionizing counterparts. Non-ionizing radiation, also known as low-energy radiation, cannot eject electrons from an outer orbital atom. Several types of electromagnetic radiation, including microwaves, visible light, and ultraviolet light are non-ionizing radiation. Ionizing radiation (IR), on the other hand, is high-frequency, high-energy radiation that ejects one or more electrons from an outer orbital atom, causing that atom to become positively charged (ionized) (Figure 1.1). IR can occur both naturally and artificially, but ultimately it is a result of the emission of high-energy waves or particles from unstable atoms. Upon energy release, the resulting high-energy emitted substance collides with cellular molecules, leading to broken atomic bonds and downstream cellular damage. There are two forms of ionizing radiation: electromagnetic and particulate (Table 1.1).

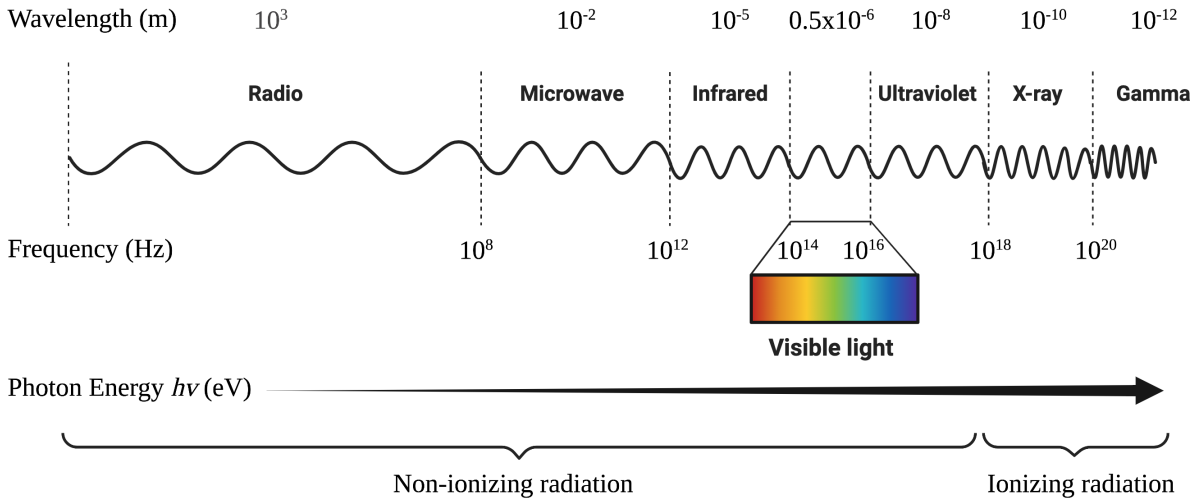

Figure 1.1: The electromagnetic spectrum. The electromagnetic spectrum consists of non-ionizing and ionizing radiation counterparts. X-rays and gamma rays are high-energy and are capable of ejecting electrons from an outer orbital atom.

Type of Ionizing Radiation		Method of Exposure
Electromagnetic	X-rays	Artificial (medical)
	Gamma rays (γ)	Artificial (medical/accelerator), Environmental (Radioactive decay)
Particulate	Alpha particle	Artificial (accelerator), Environmental (Radioactive decay)
	Beta-particle	Artificial (accelerator), Environmental (Radioactive decay)
	Proton	Artificial (accelerator), Environmental (deep space)
	Neutron	Fission, Environmental (Radioactive decay), Artificial (accelerator)
	Heavy ion	Artificial (Booster accelerator), Environmental (deep space)

Table 1.1: Types of IR and corresponding methods of exposure.

Electromagnetic ionizing radiation consists of waves and exists in two forms: x-rays and γ-rays. Both x-rays and γ-rays are part of the electromagnetic spectrum, but differ from other electromagnetic counterparts (such as visible light) in that they have much lower wavelengths, higher frequencies, and higher photon energies. Due to their higher energies, upon ionization events, x-rays and γ-rays can result in cellular damage. X-rays and γ-rays are similar in that they produce waves of electromagnetic energy, however, they differ in that x-rays are produced extranuclearly (via an outside source of electron excitation) and γ-rays are produced intranuclearly (by the nuclear decay of radioactive isotopes from within the atom) (1). Regardless, both x-rays and γ-rays have high penetrating power and can only be blocked by lead shielding. Interestingly, x-rays can also be thought of as photons, where the IR potential depends on the relative size of energy "packets" deposited, with ionizing potential thresholds >124 electron volts (eV) or a wavelength $<10^{-6}$ cm (1).

Particulate radiations are the second type of ionizing radiations. Similar to x-rays and γ-rays, particulate radiation can also lead to downstream biological damage due to its ionizing potential of nearby atoms. However, in contrast to electromagnetic radiation, particulate radiations are

naturally occurring "particles", such as α-particles, β-particles (electrons or positrons), protons, neutrons, or heavy ions. Particulate IR species may either eject from the parent atom by accelerating to high speeds artificially, as through a cyclotron or synchrotron, or may naturally occur through environmental exposures, such as radioactive decay (Figure 1.2). α-particles are a unique particulate IR species that can be artificially accelerated as well as emitted naturally through radioactive decay. Interestingly, neutrons can also be emitted as a byproduct of radioactive fission and are thus a major component in nuclear reactors. Furthermore, heavy ions are one of the most unique forms of ionizing radiation particles, as they have higher masses that have the potential to cause more biological damage than lower energy particle counterparts. Heavy ions are naturally found in deep space, but can also be artificially produced in specialized facilities when accelerated to extremely high energies, such as Brookhaven National Laboratory in Upton, NY.

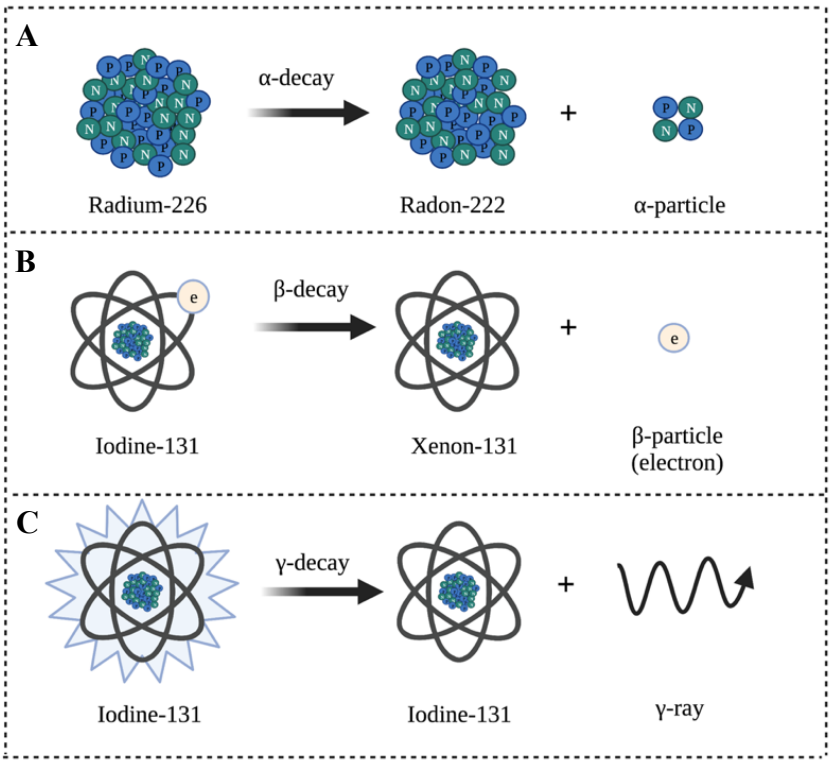

Figure 1.2: Various types of radioactive decay cause electromagnetic or particulate IR events. α-particles, β-particles, and γ-rays may be produced through natural radioactive decay processes. **A)** In α-decay, an element releases

an α-particle (2 protons and 2 neutrons) from its atomic nucleus, causing the parent element to change both atomic mass and atomic number. Here, the parent element ^{226}Ra decays to daughter element ^{222}Rn + alpha particle (^{4}He). α-particles are highly ionizing but have low penetrating power. However, they can be harmful if ingested or inhaled. **B)** β-decay can result from the emission of an electron or a positron from an atomic orbital. In this figure, ^{131}I decays primarily by β^- decay, losing an electron from its outer orbital. The resulting β-particle can penetrate a few centimeters into human skin. **C)** γ-decay results in the release of a γ-ray and is a second method of decay for radioactive ^{131}I. γ-rays have high penetrability and can pass through a human body unless protected by lead shielding.

1.2 Biological impact of IR

The biological impact of various qualities of IR depends on several factors, including the type of IR, the targeting tissue, as well as the linear energy transfer (LET).

After an atom has become ionized, either through electromagnetic or particulate IR, it has the potential to cause biological damage by interacting either directly or indirectly with the host DNA (2). In direct IR, the excited electrons hit the DNA and cause a DNA single strand break (SSB) or double strand break (DSB) firsthand. With indirect IR, stripped electrons can first interact with a nearby water molecule prior to hitting the DNA, inducing unstable hydroxyl radicals and other reactive oxygen species (ROS), which then collide with DNA to produce additional SSBs or DSBs (1). X-rays and gamma rays mostly result in indirect damage, whereas particulate radiation exposures generally result in a higher proportion of direct DNA damage (1) (Figure 1.3).

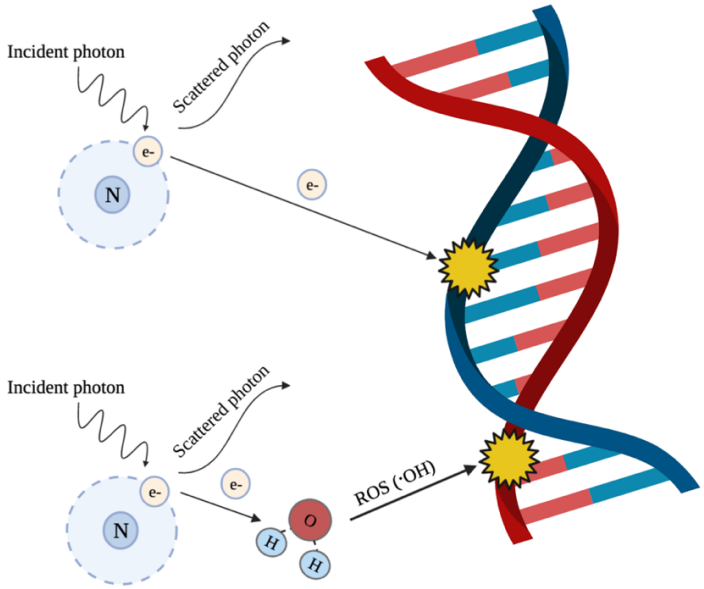

Figure 1.3: Direct and indirect damage caused by ionizing radiation. After an IR event (i.e. an x-ray exposure), DNA damage and DSBs can occur through direct contact with an excited electron or through indirect contact via free radical formation. In direct DNA damage, an excited electron hits a DNA molecule within the cell firsthand. Conversely, indirect DNA damage involves the excited electron first colliding with a surrounding water molecule, which in turn produces reactive oxygen species (ROS). The ROS then contributes to subsequent DNA damage.

It is well known that differing biological tissues have various sensitivities to IR exposures. In general, cells with high replicative capacity or high metabolism are more susceptible to IR toxicities. Particularly sensitive cell types include hematopoietic cell lineages (erythrocytes and lymphocytes) or gastrointestinal stem cells. Male spermatogonia and female oocytes are also susceptible to radiation. Cells less sensitive to IR include muscle cells and neurons, which have low replicative capacities (3).

Linear energy transfer (LET) is the energy deposited in the target material per unit distance traveled, also known as the retarding force. LET can be expressed as electron volts per micrometer (eV/μM), and it is an important factor to weigh-in when considering the biological damage to tissues after an IR exposure. It is known that various IR species of identical doses will elicit

different biological effects on the same target cells due to different LET levels (4). In general, species with higher energy demonstrate lower LET because they are moving so fast that the energy deposited per unit distance traveled in the biological tissue is much less than species with higher LET. In other words, high-LET species do not transverse through tissues as easily due to their high retarding force, allowing them to incubate with microstructures for a longer time which can cause more biological damage than lower-LET species. In general, neutrons, alpha particles, and heavy ions (such as ^{56}Fe) have higher LET than x-rays, gamma rays, and protons (1).

a. ***Signaling pathways induced by IR***

Once an atom has been stripped from its parent substance and becomes ionized, the particles or waves collide with surrounding DNA and initiate cellular damage through DNA SSB or DSBs (2). After DNA damage has been signaled, a cascade of pathways immediately activates and assesses the damage to determine cellular fate (Figure 1.4). Upon IR exposures, DNA DSBs are much more damaging than SSB. In the event of DNA SSB, the sister DNA strand provides a template which allows for more efficient repair and less consequential cell damage (5). However, in the case of DNA DSBs, increased cellular damage with more difficult repair mechanisms attributes to these lesions being the main drivers of IR-induced cellular toxicities (5).

The first responders to DNA damage include PI3-kinase regulated proteins such as Rad3-related protein (ATR), ataxia telangiectasia mutated (ATM), and DNA-dependent protein kinase (DNA-PK) kinases (6). ATR activates upon detection of DNA SSB, whereas ATM activates in response to DNA DSBs. ATR/ATM then phosphorylate and activate downstream checkpoint kinases (Chk1 and Chk2, respectively), as well as activate the tumor suppressor gene, BRCA1 (S/G2 phase) or 53BP1 (G1 phase). These phosphorylation events signal for the cell to undergo repair before progressing through the next phase of the cell cycle (6).

Another major responder induced after IR exposure and DNA DSB production is p53. p53 is a tumor suppressor protein involved in regulating cell cycle arrest, apoptosis, and DNA damage. Upon DNA DSB detection, ATM/ATR phosphorylate tumor suppressor protein p53, leading to cell cycle arrest in the G1 or G2 phases of the cell cycle (6-8). This may ultimately lead to apoptosis or senescence unless the cell can repair the IR-induced DNA damage.

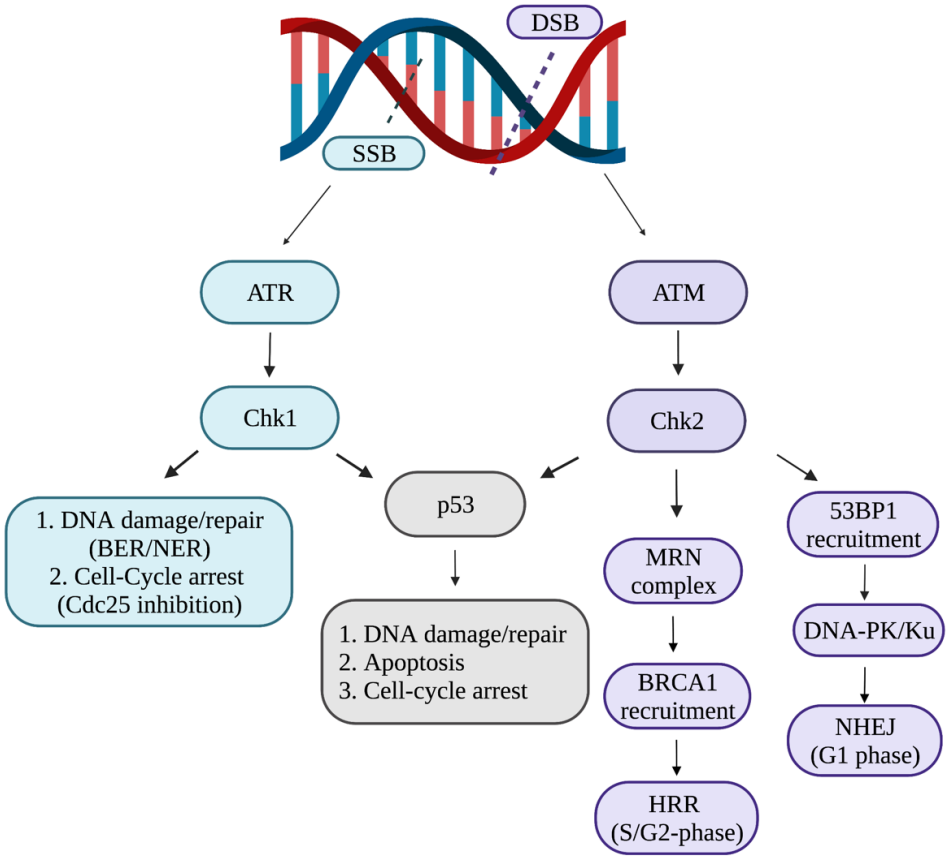

Figure 1.4: Activated pathways following IR-induced DNA damage. IR exposures lead to DNA SSB or DNA DSB through direct or indirect ionization events. Upon DNA damage, the cell attempts to repair the damage via ATR (SSB) or ATM (DSB) activation as well as the recruitment of DNA repair proteins. Upon a DNA SSB, the cell repairs itself predominantly through base-excision repair (BER) or nucleotide excision repair (NER) using the sister DNA strand as a template. Following DNA DSBs, DNA repair processes are dependent on the phase of the cell cycle and include homologous recombination repair (HRR) or non-homologous end joining (NHEJ). Tumor suppressor protein p53 is activated following IR exposures, particularly upon DNA DSBs. Upon activation of p53, the damage can be repaired, the cell will arrest, or the cell will die by apoptosis.

b. Mechanisms of DNA repair

Following IR exposure, signal transduction and intrinsic DNA damage and repair pathways will dictate whether the cell will repair itself, undergo senescence, or die by apoptosis or mitotic catastrophe (2). Upon DNA DSBs, the cell attempts to repair itself via two mechanisms: homologous recombination repair (HRR) or non-homologous end joining (NHEJ).

HRR is performed in S- and G2-phases of the cell cycle because it relies on an undamaged sister chromatid to supply the DNA template upon repair of the damaged strand following an IR exposure. The first step in HRR involves ATM phosphorylation and recruitment of the MRN (Mre11-Rad50-Nbs1) complex to the site of DNA damage. Upon ATM phosphorylation, BRCA1 is then recruited to the site of the DSB through recognition of the bound MRN complex. Through the MRN complex, Mre11 subsequently resects the damaged DNA and the 3' overhang results in the final recruitment of various HRR proteins, including BRCA2, Rad51, Rad52, and Rad54 which recruit the homologous sister chromatid to the site of repair, separate the strands, and fill in the complementary DNA gaps through "Holliday junction" crossover events (5, 6).

NHEJ is the predominant DNA DSB repair process that occurs primarily in the G1-phase of the cell cycle due to the absence of a complementary sister chromatid. Here, recruitment of ATM kinases occurs at the site of the DSB, and 53BP1 is recruited to the site of DNA repair. Once 53BP1 is recruited, this signals for the cell to undergo NHEJ rather than HRR. Subsequently, Ku70/Ku80 heterodimers recognize and bind to the ends of the DNA repair and recruit the initiation of additional DNA protein kinase catalytic subunits (DNA-PKcs) (6). Thirdly, an Artemis protein processes 5' and 3' overhangs to allow for DNA polymerase μ or λ to repair the DNA strand. In the final step, the newly repaired and synthesized DNA strand is ligated together through a PNK/XRCC4/DNA ligase IV complex (5).

c. TP53 as a regulator of cellular senescence or apoptosis

TP53 is a tumor suppressor gene that regulates p53, a tumor suppressor protein, and is involved in cell cycle arrest and apoptotic processes following genotoxic insult. Following IR exposures, mRNA expression of p53 is relatively unchanged, however, post-translational modifications of p53 protein, including phosphorylation and acetylation, prolong its stability within the cell and lead to activation of DNA damage/DNA repair or cell death processes (7, 8). As p53 becomes phosphorylated, its stability increases by displacing p53 from MDM2-targeted degradation, and this allows p53 to act as a positive transcriptional regulator of downstream apoptotic genes or cyclin dependent kinases, inducing cell death or cell cycle arrest, respectively (7, 8). Cyclin dependent kinase (Cdk) inhibitory protein 21 (p21/CDKN1A) is heavily activated following p53 phosphorylation and serves as a biomarker of cell cycle arrest in the G1-phase of the cell cycle. Apoptotic-regulated genes like BAX (pro-apoptotic), BCL2 (pro-apoptotic), and BCL2L1 (anti-apoptotic), as well as DNA damage responders, such as DDB2 and XPC, are additional examples of genes regulated by p53.

d. Relative Biological Effectiveness

The cell or tissue toxicities induced by a particular type of radiation exposure may differ based on several factors, including the radiation quality or LET, the cumulative dose and dose rate, as well as the biological system exposed (4). Taken together, the effect of IR on biological tissues is termed relative biological effectiveness (RBE) and is classified based on a quantitative ratio of ($D_{X\text{-}ray}/D_{IR}$), where $D_{X\text{-}ray}$ is the biological impact resulting from 250 keV x-rays relative to the effect from the unique IR species of interest (D_{IR}) (4). In general, IR species with higher LET have increased biological effectiveness up to about 100 keV/μM. After peaking at 100 keV/μM,

the RBE then decreases (4). It is known that at an LET of ~100 keV/μM is optimal to achieve a DNA DSB by the passage of a single charged particle, as this aligns with the diameter of a DNA double helix (4). In other words, at an LET of 100 keV/μM, there is an optimal amount of DNA damage per particle track, whereas particles with very high LET (>100 keV/μM) can lead to more than two ionization events per particle track, effectively delivering excess energy without increasing the biological damage per unit dose.

The RBE in cells and tissues also depends on the total dose received as well as the dose rate administered. It is well accepted that the higher the radiation dose, the higher the probability of biological damage, however, this can differ based on the biological system exposed. For example, total body IR of about 3.5-4.0 Gy is lethal in about 50% of the human population (9), but tumors themselves can be targeted in fractionated doses upwards of 50 Gy (10). In addition to the total dose received, the dose rate can also alter the RBE of IR species. For example, dividing a single dose into fractionated doses can provide time for the cell to repair sublethal damage and can lead to an increased tolerance of the cell type to absorb more total dose for the same net cell kill (11). This dose-rate effect is most evident in cell death between 0.01 and 1 Gy/min, but can be seen at higher doses as well. In the clinic, fractionated doses are primarily important for patients undergoing radiation therapy for solid tumors. In these cases, fractionated IR doses are favorable as they provide time for both the normal cells surrounding the tumor to potentially repair sublethal damage while also providing time for the tumor to reoxygenate. This reoxygenation of the tumor can lead to an increase in tumor cell kill due to the oxygen enhancement ratio (OER). With increased oxygen, IR increases ROS and free radicals which corresponds to increased DNA

damage. In the case of tumors, fractionated doses give time for the necrotic tumor tissue to re-oxygenate and become susceptible to another fraction of IR therapy (12) (Figure 1.5).

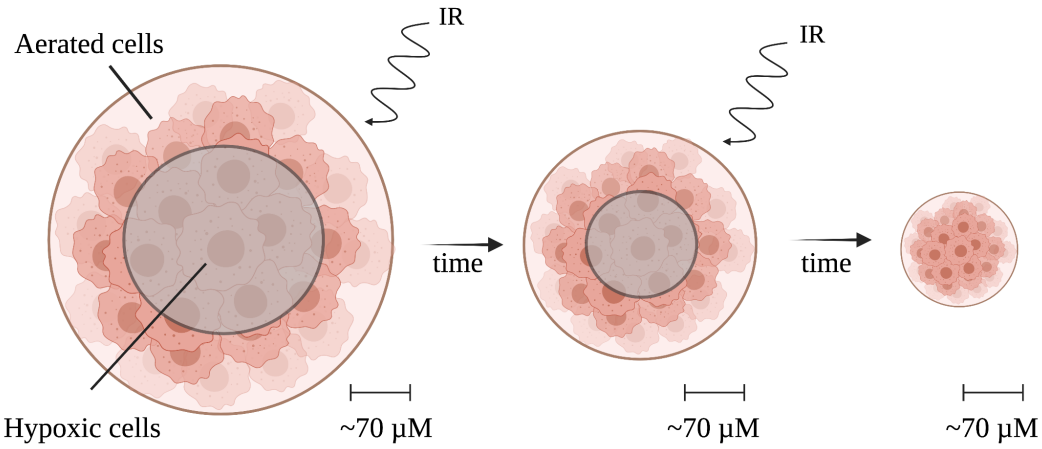

Figure 1.5: Fractionation of IR doses increases tumor cell kill while sparing normal tissues due to the oxygen enhancement ratio (OER). Here, a solid tumor is represented by oxygenated tissue (pink) and hypoxic/necrotic tissue (gray). In general, tumors only have about 70 µM of oxygenated tissue located on the periphery of the tumor, as blood vessels within the tumor are irregular and prevent proper oxygenation. As the tumor is exposed to IR therapy, the enhanced cell kill from oxygenated tissue leads to increased cell death/shrinkage of the outer layer of the tumor. As the tumor is exposed to fractionated doses of IR, time allows for former necrotic tissue to reoxygenate and be susceptible to a second fraction of IR therapy. After multiple fractions, the tumor will ideally be comprised of only oxygenated tissue, making it fully susceptible to IR.

RBE is also dependent on cell type, as it is known that various tissues are more susceptible to IR damage than others, with cells that have higher mitotic frequency (i.e. lymphocytes or gut epithelia) being more susceptible to IR than cells with lower replicative potential (i.e. neurons) (9). The stage of the cell cycle also affects overall cell kill per unit dose, as cells are more prone to lethal damage when targeted in late G2- or M-phases and most resistant in S-phase (where DNA replication is occurring and can be more easily repaired). The route of IR exposure can also have profound effect on overall RBE. For example, alpha particles are relatively heavy species that

cannot penetrate a thin sheet of paper if administered externally, however, if ingested, alpha particles are strongly ionizing and cause severe toxicity (13).

e. Side effects of IR

IR exposures can lead to a range of side effects dependent upon the total dose received as well as the RBE of the tissue(s) exposed. Mild radiation exposures (1-2 Gy) may lead to a compromised immune system through hematopoietic lymphocyte depletion within the bone marrow. In addition, moderate (2-4 Gy) exposures may cause a leaky GI tract due to gastrointestinal cell depletion within the stem cell crypts which may result in diarrhea and/or a systemic infection. Around the LD_{50} of ~3.5-4 Gy, common symptoms also include anorexia, nausea, and vomiting (13). Severe exposures (>4 Gy) may lead to side effects characteristic of acute radiation syndrome (ARS) including high fevers, infections, bleeding, disorientation, and death if not properly treated (13). Well-accepted long-term exposures, depending on dose, may also contribute to cataractogenesis, infertility, and increased incidence of primary or secondary cancers (9, 14-16).

1.3 Clinical Ionizing Radiation Exposures

Although ionizing radiation leads to cellular damage, this phenomenon is a double-edged sword. On the one hand, unwarranted IR exposures can damage normal cells and tissues through local bystander effects. On the other hand, however, IR treatments provide great benefit to decrease tumor burden, is even curative for some cancers, and is routinely used as a standard-of-care for cancer therapy in the clinic.

The use of ionizing radiation in modern medicine is unprecedented and serves as one of the pillars of cancer therapy. High energy external beam IR therapy can be meticulously targeted to a

tumor site-specifically, leading to tumor contraction or eradication while sparing surrounding tissues (17). Currently, external beam photons, protons, electrons, and heavy ion therapies have been explored in the clinic (18). Internal brachytherapy, where the IR source targets the tumor site-specifically, has also demonstrated promise in the clinic, and is currently explored for several cancers, including prostate, breast, cervical, bladder, and head and neck tumors (19). In addition, radioactive isotopes can be utilized for delivering targeted radiation to tumors site-specifically, including ^{131}I as a treatment for high-risk neuroblastoma patients (20, 21).

a. Radiotherapy and Imaging

Another potential source of IR exposure in the clinic is through imaging modalities, including x-rays, CT scans, as well as tagged radioisotopes for imaging contrast. These IR exposures are used to detect inflammation, tumors, or abnormal bone or tissue maladies. For example, radiolabeled pharmaceuticals, such as fluorodeoxyglucose 18F (^{18}F-FDG), are administered for positron emission tomography (PET) imaging to track glucose metabolism and detect tumor metastasis or inflammation (22).

Other radioisotopes are conjugated to drugs to deliver targeted radiotherapy. For example, actinium-225 (^{225}Ac), bismuth-213 (^{213}Bi), and yttrium-90 (^{90}Y) conjugates are being studied as potential glioblastoma multiforme therapies (23, 24). In addition, radiolabeled monoclonal antibodies ^{225}Ac or ^{213}Bi conjugated to cetuximab (anti-EGFR), lintuzumab (HuM195, anti-CD33), or anti-CD20 antibodies are administered for Non-Hodgkin's lymphoma, leukemia, and bladder cancer (25). ^{131}I conjugated to anti-tenascin antibodies has also been investigated in many glioblastoma multiforme trials (26). In this dissertation, I will discuss ^{131}I-metaiodobenzylguanidine (^{131}I-mIBG), a radionuclide currently in a Phase II/III clinical trial for

high-risk neuroblastoma patients (Clinicaltrials.gov identifiers: NCT02035137 and NCT03126916) (Figure 1.6).

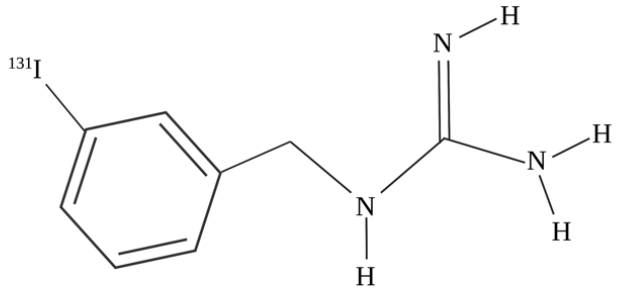

Figure 1.6: Structure of ^{131}I-metaiodobenzylguanidine (^{131}I-mIBG). ^{131}I-mIBG is a radiopharmaceutical used for imaging as well as delivering targeted radiation therapy to patients with neuroblastoma tumors. It undergoes radioactive decay through both β^- and gamma emissions with a physical half-life of about 8 days.

b. ^{131}I-mIBG as a targeted radiotherapy

^{131}I-mIBG serves as an analogue to norepinephrine, an endogenous neurotransmitter in the peripheral nervous system. The great majority of ^{131}I-mIBG is readily taken up in neuroblastoma tumors site-specifically via the norepinephrine transporter (NET) pathway, and it has been well recognized that MIBG avidity is directly proportional to NET levels (27, 28). ^{131}I-mIBG delivers targeted radiation treatment via beta minus (90%) and gamma (10%) decay, with myelosuppression being the major dose-limiting toxicity (21). It is currently administered intravenously in high-risk neuroblastoma patients, who often display with advanced stage and distant metastases (21). A recent Phase I clinical trial demonstrated that ^{131}I-mIBG treatment with irinotecan and vincristine was generally well-tolerated at a maximum dose of 18 mCi/kg (20). A Phase II pilot study also demonstrated that peripheral blood from patients treated with ^{131}I-mIBG can detect DNA damage and apoptosis up to 96 hours after exposure (29). It was also revealed that FLT3 ligand, *BCLXL*, and *DDB2* levels are associated with acute ^{131}I-mIBG toxicity (30). It

remains to be elucidated if peripheral blood biomarkers may indicate the likelihood of response to ^{131}I-mIBG or may be good indicators for tracking ^{131}I-mIBG normal tissue toxicity. Finally, ^{131}I-mIBG treatment may serve as an ideal biodosimetry tool for understanding internalized radiation exposures. This dissertation focuses on understanding the transcriptional response induced by p53 following ^{131}I-mIBG therapy in relapsed and refractory neuroblastoma patients and identifying biomarkers of early (72 hours) and late (15 days) exposure to ^{131}I following ^{131}I-mIBG treatment. This dissertation encompasses findings from a New Approaches to Neuroblastoma Therapy (NANT) clinical trial (Clinical trial identifier: NCT02035137).

1.4 Environmental Ionizing Radiation Exposures

a. Background exposures on Earth

While efficacious at treating tumors with normal tissue sparing, IR is also an inherent environmental problem. Background levels of radiation result from everyday life, including potassium-40, uranium-238, and radon-222 elements which are present in the terrestrial atmosphere or in the food we eat. Pilots, as well as individuals housed in high elevations, are also more heavily exposed to cosmic radiation emitted from the sun. Background levels of radiation exposure may also be acquired artificially, such as that from an x-ray. Interestingly, the United States Nuclear Regulatory Commission estimates that an average person receives about 620 mrem (6.2 mSv) annually from natural and artificial radiation combined (31). Typical background radiation is not known to be harmful to human health, although excessive exposure to areas of high background radiation, such as living in an area with high radon emissions, has been linked to increased risk of lung cancer (32).

b. Exposures beyond low Earth orbit (deep space)

The Earth's magnetosphere naturally shields humans from most of the cosmic radiation exposures emitted from the sun. Therefore, the biological effects of radiation exposure for astronauts traveling outside of the Earth's magnetosphere, also known as beyond low Earth orbit (LEO), present unknown risks. Space radiation beyond LEO includes exposure to additional IR contributors, including galactic cosmic radiation (GCR) and solar particle events (SPE), encompassing high energy protons, alpha particles, and heavy ion species (HZE) (33) (Figure 1.7). GCR, comprised of mostly protons and alpha particles, as well as HZE exposures are particularly harmful for astronauts beyond LEO and for long missions, such as a planned three-year exploration to Mars (34). Space exposure, like other types of IR, may lead to skin lesions, hematological and immune system dysfunction, neural behavioral changes, or secondary cancers (33). However, the overall RBE of cumulative space IR exposure on human health remains unknown. Recently, an astronaut-twin study investigating various biological endpoints comparing an astronaut aboard the International Space Station (ISS) for 1 year compared to his Earth-bound twin reported alterations in several biological endpoints, including gene transcription, body weight, microbiome components, and cognitive impairment (35). However, future studies are needed to confirm these findings as well as provide better estimates for the biological effects in humans in missions beyond LEO. A better understanding of human response to space radiation exposures, as well as the mechanisms of space radiation-induced toxicities, are needed to develop effective countermeasures for deep space flight.

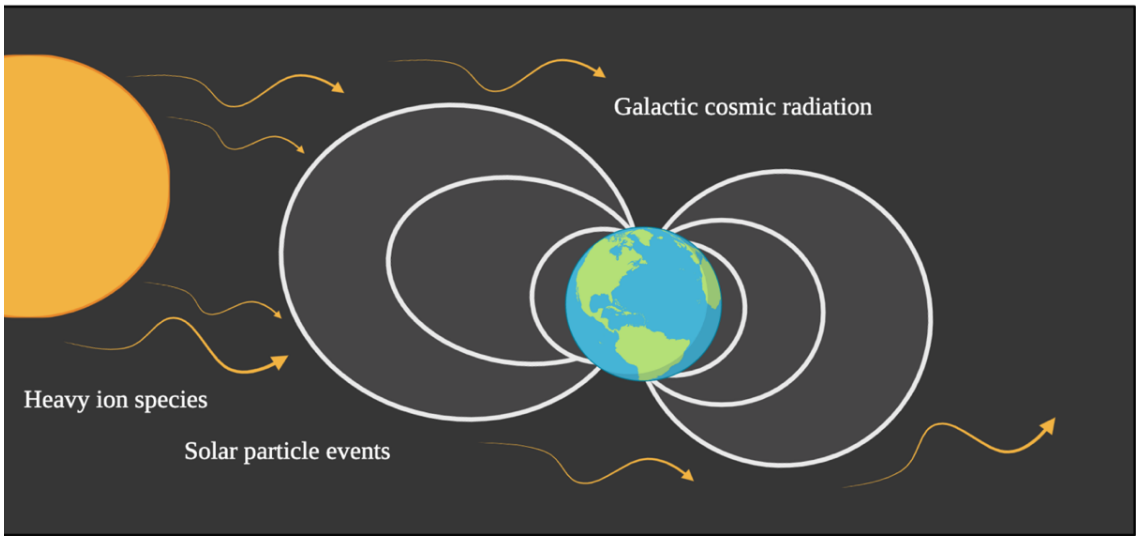

Figure 1.7: The Earth's magnetosphere protects against heavy amounts of cosmic radiation. The Earth's magnetosphere (gray/white rings) protects humans from exposure to radiation in deep space. Human exposures beyond low-earth orbit include galactic cosmic radiation (GCR), heavy ion species, and solar particle events (SPE). For astronauts traveling to Mars, exposure to heavy ions, solar flares, and GCR may contribute to hematological or neurological toxicities.

c. Simulating deep space exposures here on Earth

To simulate GCR, SPE, and HZE exposures found in deep space, specialized facilities that accelerate particles to extremely high energies are required. Brookhaven National Laboratory in Upton, NY houses one such facility known as the Nasa Space Radiation Laboratory (NSRL). The NSRL beamline can accelerate ions from lightweight protons to heavy gold particles between 50-2,500 MeV per atomic mass unit (MeV/n) (36). In 2018, NSRL opened up the first GCR simulator, housing both the option to test a 33-ion "full" GCR simulator as well as a simplified 5-ion GCR simulator that mimic the IR particle fluences characteristic of the deep space environment (36). Since only one ion species can travel through the beam at once, both the full 33-ion GCR simulator and the simplified 5-ion GCR simulator require sequential fractions of the total dose to be administered in tandem. This dissertation will describe radiation experiments performed at NSRL

using the 5-ion GCR simulator beam (SimGCRSim). Within this simplified 5-ion GCR beam, the order of the ions and corresponding energies delivered to the target cells are as follows: 1000 MeV/n protons, 600 MeV/n Si-28 ions, 250 MeV/n He-4 ions, 350 MeV/n O-16 ions, 600 MeV/n Fe-56 ions, and finally another dose of 250 MeV/n protons (36). As is characteristic of deep space, the simulated 5-ion GCR simulator delivers most of the target dose in protons (74%), followed by He-4 ions (18%), O-16 ions (6%), and a small fraction of the HZE species Si-28 (1%) and Fe-56 (1%) (36).

1.5 Developing new means to address IR exposures

Developing safe and effective radioprotectors or radiomitigators is vital for minimizing normal tissue damage either before (radioprotector) or following (radiomitigator) an ionizing radiation exposure. Mechanisms of radiation protection may include scavenging free radicals, promoting cell cycle arrest, decreasing apoptosis (p53) activation, or stabilizing the cellular DNA (37). Currently, amifostine and palifermin are the only two radiation protection agents in the United States that are FDA-approved for use in combination with radiotherapy (37). Amifostine, a prodrug, is currently administered intravenously and metabolizes to an active free-radical scavenger, preventing severe xerostomia in head and neck cancer patients (38). It has further been suggested that amifostine may also induce cellular hypoxia and protect against DNA damage in normal tissues (39). The second FDA-approved drug on the market, palifermin, is a recombinant human keratinocyte growth factor receptor that activates the MAPK pathway on buccal cell surfaces to stimulate cell growth and survival. Palifermin is administered as a radioprotector three days before IR-based therapy and effectively reduces oral mucositis in hematologic cancer patients undergoing a combined radiotherapy/chemotherapy regimen (40).

In recent years, dietary supplements and natural compounds have also been proposed as potential radioprotectors and/or radiomitigators due to their native antioxidant properties (41). One of the major antioxidants of interest is curcumin, a natural compound found within the spice turmeric (42). Throughout this dissertation, I will focus on investigating the radioprotective and radiomitigative effects of curcumin on a human fibroblast cell line exposed to both low and high-LET radiation qualities.

a. *Curcumin*

Curcumin, the main polyphenol within the spice turmeric, is a natural anti-inflammatory and antioxidant agent that has been used for centuries in Ayurvedic medicine, as a common food additive, and as a dye colorant globally (43) (Figure 1.8). Interestingly, curcumin has shown promise as both a radiation protectant in normal tissues as well as a radiation sensitizer in cancerous tissues (44). However, due to its lipophilic nature, curcumin is virtually insoluble in water and its bioavailability is therefore limited. It has been proposed that curcumin bioavailability may increase when formulated in the presence of lipids, when embedded in alternate matrices, or in conjunction with adjuvant moieties, such as piperine (45) . This dissertation focuses on solubilizing curcumin within a nanodisc environment, known as an NLP, to improve curcumin solubility and bioavailability for downstream *in vitro* or *in vivo* applications.

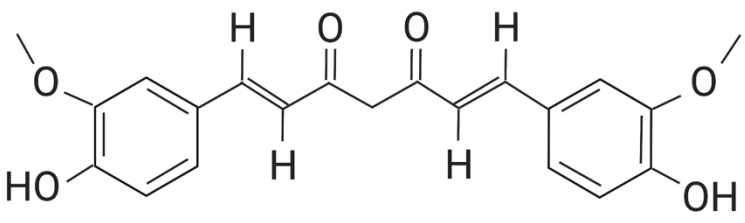

Figure 1.8: Structure of curcumin. Curcumin is the principal curcuminoid component within the spice turmeric.

b. *NLPs*

Nanolipoprotein particles (NLPs) are ~10-20 nm lipid nanodiscs consisting of a lipid bilayer mimetic surrounded by a scaffolding protein or polymeric moiety (Figure 1.9). Due to their lipid composition and resemblance to human high-density lipoprotein (HDL) molecules, NLPs provide a versatile and customizable platform that can readily transport molecules to the cell and deliver cargo both *in vitro* and *in vivo* (46). Moreover, they are non-toxic and can be readily purified and lyophilized for long-term storage purposes.

At Lawrence Livermore National Laboratory (LLNL), we have recently shown that NLPs can be customized for solubilizing membrane proteins as well as forming NLP:nucleic acid complexes which may be useful for vaccine applications (47-49). This dissertation expands upon our previously published works with NLPs and investigates their uses for increasing the solubility and bioavailability of antioxidant molecules, particularly curcumin, in cell model systems. Although the feasibility of solubilizing curcumin in an apolipoprotein-derived disc has previously been published (50, 51), we differ from these studies in that we are also testing the protective effects of curcumin nanodiscs against IR exposures within a normal human cell line model. These studies may prove useful for developing novel nutri-pharmaceutical agents to combat the negative side effects following clinical and/or environmental IR exposures.

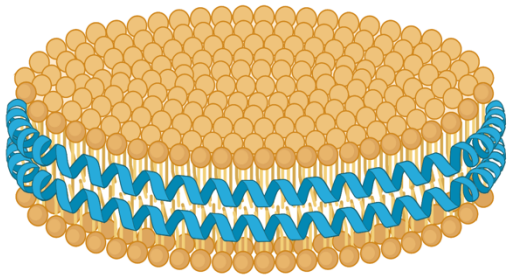

Figure 1.9: Illustration of a nanolipoprotein particle (NLP). Shown is a representative empty NLP disc surrounded by an apolipoprotein scaffold (blue). In practice, cargo molecules (such as membrane proteins

adjuvants, or lipophilic compounds) can be embedded within the lipid bilayer to improve solubility or cell delivery *in vitro* or *in vivo*. Additional surrounding moieties in lieu of the apolipoprotein scaffold may include polymers.

Aim of Dissertation:

This dissertation has two goals that focus on understanding and modulating the biological effects of ionizing radiation that directly impact humans. The first is clinically focused. I will use transcript signatures in the peripheral blood to investigate the early and late effects of the DNA damage response in children exposed to ^{131}I-mIBG as part of his or her cancer therapy regimen. The goal of this chapter is to apply this internal ^{131}I exposure data as a model for biodosimetry for a vulnerable population in the event of a radiologic disaster. This data also serves as supporting data to reveal biomarkers associated with positive patient outcomes in high-risk neuroblastoma patients as part of a Phase II NANT-2011-01 clinical trial. The second part of my dissertation work focuses on understanding the associated DNA damage, transcriptomic alterations, and hematological toxicities from environmental radiation exposures associated with space travel and developing and characterizing curcumin-nanoparticles as countermeasures to these exposures. The relative biological effectiveness of space radiation exposures will be studied using human-derived fibroblasts treated with and without curcumin-loaded NLPs. This dissertation serves to validate the transcriptome within the peripheral blood as a useful tool for biodosimetry, exposure triage, and treatment outcome in both neuroblastoma patients and astronauts exposed to ionizing radiation exposures. Furthermore, this dissertation outlines a path forward for using curcumin-loaded nanoparticles as a protectant against cellular toxicities induced by IR exposures both in the clinic or within the deep space environment.

Chapter 1 References:

1. Giaccia EJHaAJ. Radiobiology for the Radiologist. Chapter 1: Physics and Chemistry of Radiation Absorption ed: Wolters Kluwer, Lippincott Williams & Wilkins; 2012. p. 3-11.
2. Lomax ME, Folkes LK, O'Neill P. Biological consequences of radiation-induced DNA damage: relevance to radiotherapy. Clin Oncol (R Coll Radiol). 2013;25(10):578-85.
3. Giaccia EJHaAJ. Radiobiology for the Radiologist. Wolters Kluwer, Lippincott Williams & Wilkins; 2012. p. 327-55.
4. Giaccia EJHaAJ. Radiobiology for the Radiologist. Wolters Kluwer, Lippincott Williams & Wilkins; 2012. p. 104-13.
5. Giaccia EJHaAJ. Radiobiology for the Radiologist. Wolters Kluwer, Lippincott Williams & Wilkins; 2012. p. 12-34.
6. Santivasi WL, Xia F. Ionizing radiation-induced DNA damage, response, and repair. Antioxid Redox Signal. 2014;21(2):251-9.
7. Fei P, El-Deiry WS. P53 and radiation responses. Oncogene. 2003;22(37):5774-83.
8. Lakin ND, Jackson SP. Regulation of p53 in response to DNA damage. Oncogene. 1999;18(53):7644-55.
9. Bolus NE. Basic Review of Radiation Biology and Terminology. J Nucl Med Technol. 2017;45(4):259-64.
10. Zaorsky NG, Palmer JD, Hurwitz MD, Keith SW, Dicker AP, Den RB. What is the ideal radiotherapy dose to treat prostate cancer? A meta-analysis of biologically equivalent dose escalation. Radiother Oncol. 2015;115(3):295-300.
11. Giaccia EJHaAJ. Radiobiology for the Radiologist. Wolters Kluwer, Lippincott Williams & Wilkins; 2012. p. 67-85.
12. Giaccia EJHaAJ. Radiobiology for the Radiologist. Wolters Kluwer, Lippincott Williams & Wilkins; 2012. p. 86-103.
13. Giaccia EJHaAJ. Radiobiology for the Radiologist. Wolters Kluwer, Lippincott Williams & Wilkins; 2012. p. 114-28.
14. Ainsbury EA, Bouffler SD, Dorr W, Graw J, Muirhead CR, Edwards AA, et al. Radiation cataractogenesis: a review of recent studies. Radiat Res. 2009;172(1):1-9.
15. Gilbert ES. Ionising radiation and cancer risks: what have we learned from epidemiology? Int J Radiat Biol. 2009;85(6):467-82.
16. Ogilvy-Stuart AL, Shalet SM. Effect of radiation on the human reproductive system. Environ Health Perspect. 1993;101 Suppl 2:109-16.
17. Baskar R, Lee KA, Yeo R, Yeoh KW. Cancer and radiation therapy: current advances and future directions. Int J Med Sci. 2012;9(3):193-9.
18. Minniti G, Goldsmith C, Brada M. Radiotherapy. Handb Clin Neurol. 2012;104:215-28.
19. Balgobind BV, Koedooder K, Ordonez Zuniga D, Davila Fajardo R, Rasch CR, Pieters BR. A review of the clinical experience in pulsed dose rate brachytherapy. Br J Radiol. 2015;88(1055):20150310.
20. DuBois SG, Chesler L, Groshen S, Hawkins R, Goodarzian F, Shimada H, et al. Phase I study of vincristine, irinotecan, and (1)(3)(1)I-metaiodobenzylguanidine for patients with relapsed or refractory neuroblastoma: a new approaches to neuroblastoma therapy trial. Clin Cancer Res. 2012;18(9):2679-86.
21. DuBois SG, Matthay KK. Radiolabeled metaiodobenzylguanidine for the treatment of neuroblastoma. Nucl Med Biol. 2008;35 Suppl 1:S35-48.

22. Cacicedo J, Navarro A, Del Hoyo O, Gomez-Iturriaga A, Alongi F, Medina JA, et al. Role of fluorine-18 fluorodeoxyglucose PET/CT in head and neck oncology: the point of view of the radiation oncologist. Br J Radiol. 2016;89(1067):20160217.
23. Cordier D, Forrer F, Kneifel S, Sailer M, Mariani L, Macke H, et al. Neoadjuvant targeting of glioblastoma multiforme with radiolabeled DOTAGA-substance P--results from a phase I study. J Neurooncol. 2010;100(1):129-36.
24. Krolicki L, Kunikowska J, Bruchertseifer F, Koziara H, Krolicki B, Jakucinski M, et al. (225)Ac- and (213)Bi-Substance P Analogues for Glioma Therapy. Semin Nucl Med. 2020;50(2):141-51.
25. Morgenstern A, Apostolidis C, Kratochwil C, Sathekge M, Krolicki L, Bruchertseifer F. An Overview of Targeted Alpha Therapy with (225)Actinium and (213)Bismuth. Curr Radiopharm. 2018;11(3):200-8.
26. Reulen HJ, Suero Molina E, Zeidler R, Gildehaus FJ, Boning G, Gosewisch A, et al. Intracavitary radioimmunotherapy of high-grade gliomas: present status and future developments. Acta Neurochir (Wien). 2019;161(6):1109-24.
27. Dubois SG, Geier E, Batra V, Yee SW, Neuhaus J, Segal M, et al. Evaluation of Norepinephrine Transporter Expression and Metaiodobenzylguanidine Avidity in Neuroblastoma: A Report from the Children's Oncology Group. Int J Mol Imaging. 2012;2012:250834.
28. Kayano D, Kinuya S. Current Consensus on I-131 MIBG Therapy. Nucl Med Mol Imaging. 2018;52(4):254-65.
29. Edmondson DA, Karski EE, Kohlgruber A, Koneru H, Matthay KK, Allen S, et al. Transcript Analysis for Internal Biodosimetry Using Peripheral Blood from Neuroblastoma Patients Treated with (131)I-mIBG, a Targeted Radionuclide. Radiat Res. 2016;186(3):235-44.
30. Campbell K, Karski EE, Olow A, Edmondson DA, Kohlgruber AC, Coleman M, et al. Peripheral Blood Biomarkers Associated With Toxicity and Treatment Characteristics After (131)I- Metaiodobenzylguanidine Therapy in Patients With Neuroblastoma. Int J Radiat Oncol Biol Phys. 2017;99(2):468-75.
31. EPA. Radiation Sources and Doses 2020 [Available from: https://www.epa.gov/radiation/radiation-sources-and-doses.
32. Lorenzo-Gonzalez M, Torres-Duran M, Barbosa-Lorenzo R, Provencio-Pulla M, Barros-Dios JM, Ruano-Ravina A. Radon exposure: a major cause of lung cancer. Expert Rev Respir Med. 2019;13(9):839-50.
33. Chancellor JC, Scott GB, Sutton JP. Space Radiation: The Number One Risk to Astronaut Health beyond Low Earth Orbit. Life (Basel). 2014;4(3):491-510.
34. Nelson GA. Space Radiation and Human Exposures, A Primer. Radiat Res. 2016;185(4):349-58.
35. Garrett-Bakelman FE, Darshi M, Green SJ, Gur RC, Lin L, Macias BR, et al. The NASA Twins Study: A multidimensional analysis of a year-long human spaceflight. Science. 2019;364(6436).
36. Simonsen LC, Slaba TC, Guida P, Rusek A. NASA's first ground-based Galactic Cosmic Ray Simulator: Enabling a new era in space radiobiology research. PLoS Biol. 2020;18(5):e3000669.
37. Aliper AM, Bozdaganyan ME, Sarkisova VA, Veviorsky AP, Ozerov IV, Orekhov PS, et al. Radioprotectors.org: an open database of known and predicted radioprotectors. Aging (Albany NY). 2020;12(15):15741-55.

38. Giaccia EJHaAJ. Radiobiology for the Radiologist. 2012. p. 129-34.
39. Kouvaris JR, Kouloulias VE, Vlahos LJ. Amifostine: the first selective-target and broad-spectrum radioprotector. Oncologist. 2007;12(6):738-47.
40. Spielberger R, Stiff P, Bensinger W, Gentile T, Weisdorf D, Kewalramani T, et al. Palifermin for oral mucositis after intensive therapy for hematologic cancers. N Engl J Med. 2004;351(25):2590-8.
41. Weiss JF, Landauer MR. Protection against ionizing radiation by antioxidant nutrients and phytochemicals. Toxicology. 2003;189(1-2):1-20.
42. Hewlings SJ, Kalman DS. Curcumin: A Review of Its Effects on Human Health. Foods. 2017;6(10).
43. Xu XY, Meng X, Li S, Gan RY, Li Y, Li HB. Bioactivity, Health Benefits, and Related Molecular Mechanisms of Curcumin: Current Progress, Challenges, and Perspectives. Nutrients. 2018;10(10).
44. Goel A, Aggarwal BB. Curcumin, the golden spice from Indian saffron, is a chemosensitizer and radiosensitizer for tumors and chemoprotector and radioprotector for normal organs. Nutr Cancer. 2010;62(7):919-30.
45. Stohs SJ, Chen O, Ray SD, Ji J, Bucci LR, Preuss HG. Highly Bioavailable Forms of Curcumin and Promising Avenues for Curcumin-Based Research and Application: A Review. Molecules. 2020;25(6).
46. Fischer NO, Weilhammer DR, Dunkle A, Thomas C, Hwang M, Corzett M, et al. Evaluation of nanolipoprotein particles (NLPs) as an in vivo delivery platform. PLoS One. 2014;9(3):e93342.
47. He W, Evans AC, Rasley A, Bourguet F, Peters S, Kamrud KI, et al. Cationic HDL mimetics enhance in vivo delivery of self-replicating mRNA. Nanomedicine. 2020;24:102154.
48. He W, Felderman M, Evans AC, Geng J, Homan D, Bourguet F, et al. Cell-free production of a functional oligomeric form of a Chlamydia major outer-membrane protein (MOMP) for vaccine development. J Biol Chem. 2017;292(36):15121-32.
49. Tifrea DF, He W, Pal S, Evans AC, Gilmore SF, Fischer NO, et al. Induction of Protection in Mice against a Chlamydia muridarum Respiratory Challenge by a Vaccine Formulated with the Major Outer Membrane Protein in Nanolipoprotein Particles. Vaccines (Basel). 2021;9(7).
50. Ghosh M, Ryan RO. ApoE enhances nanodisk-mediated curcumin delivery to glioblastoma multiforme cells. Nanomedicine (Lond). 2014;9(6):763-71.
51. Ghosh M, Singh AT, Xu W, Sulchek T, Gordon LI, Ryan RO. Curcumin nanodisks: formulation and characterization. Nanomedicine. 2011;7(2):162-7.

Acknowledgement: All the figures in this chapter were created with BioRender.com

Chapter 2: Peripheral blood transcript signatures after internal ^{131}I-mIBG therapy in relapsed and refractory neuroblastoma patients identifies early and late biomarkers of internal ^{131}I exposures

This work is published in *Radiation Research. 2022; 197:101-112197;* DOI: 10.1667/RADE-20-00173.1. and is re-printed with permission as part of this dissertation. The approval letter to re-publish as part of this dissertation is included in the Appendix. The Figure and Table numbers have been altered from the original publication to fit this dissertation format.

Authors:

Angela C. Evans[1,2,*], Tim Setzkorn[3], David A. Edmondson[4], Haley Segelke[2], Paul F. Wilson[1], Katherine K. Matthay[5], M. Meaghan Granger[6], Araz Marachelian[7], Daphne A. Haas-Kogan[8], Steven G. DuBois[9], Matthew A. Coleman[1,2]

1. Department of Radiation Oncology, University of California Davis, Sacramento, CA.

2. Lawrence Livermore National Laboratory, Livermore, CA

3. Technical University of Munich, School of Medicine, Germany.

4. Cincinnati Children's Hospital Medical Center, Cincinnati OH

5. Department of Pediatrics, University of California San Francisco School of Medicine, San Francisco CA.

6. Department of Pediatrics, Cook Children's Hospital, Fort Worth, TX.

7. Department of Pediatrics, Children's Hospital Los Angeles, Los Angeles, CA

8. Department of Radiation Oncology, Brigham and Women's Hospital and Dana-Farber Cancer Institute, Boston, MA

9. Dana-Farber/Boston Children's Cancer and Blood Disorders Center, Boston, MA

* Scholar in Training

Corresponding Author: Matthew A. Coleman, coleman16@llnl.gov

2.1 Abstract

^{131}I-metaiodobenzylguanidine (^{131}I-mIBG) is a targeted radiation therapy developed for the treatment of advanced neuroblastoma. We have previously shown that this patient cohort can be used to predict absorbed dose associated with early ^{131}I exposure, 72 hours after treatment. We now expand these studies to identify gene expression differences associated with ^{131}I-mIBG exposure 15 days after treatment. Total RNA from peripheral blood lymphocytes was isolated from 288 whole blood samples representing 59 relapsed or refractory neuroblastoma patients before and after ^{131}I-mIBG treatment. We found that several transcripts predictive of early exposure returned to baseline levels by day 15, however, selected transcripts did not return to baseline. At 72 hours, all 17 selected pathway-specific transcripts were differentially expressed. Transcripts *CDKN1A* ($p<0.000001$), *FDXR* ($p<0.000001$), *DDB2* ($p<0.000001$), and *BBC3* ($p<0.000001$) showed the highest up-regulation at 72 hours post-^{131}I-mIBG exposure, with mean $\log_2$ fold changes of 2.55, 2.93, 1.86, and 1.85, respectively. At 15 days post-^{131}I-mIBG, 11 of the 17 selected transcripts were differentially expressed, with *XPC*, *STAT5B*, *PRKDC*, *MDM2*, *POLH*, *IGF1R,* and *SGK1* displaying significant up-regulation at 72 hours and significant down-regulation at 15 days. Interestingly, transcripts *FDXR* ($p=0.01$), *DDB2* ($p=0.03$), *BCL2* ($p=0.003$), and *SESN1* ($p<0.0003$) maintained differential expression 15 days after ^{131}I-mIBG treatment. These results suggest that transcript levels for DNA repair, apoptosis, and ionizing radiation (IR)-induced cellular stress are still changing by 15 days post ^{131}I-mIBG treatment. Our studies showcase the use of biodosimetry gene expression panels as predictive biomarkers following early (72 hours) and late (15-day) internal ^{131}I exposure. Our findings also demonstrate the utility of our transcript

panel to differentiate exposed from non-exposed individuals up to 15 days post-exposure from internal ^{131}I.

2.2 Introduction

Biodosimetry assays are employed as surrogate measurements or supplements to physical ionizing radiation (IR) dosimetry that are based on assaying the outcomes of cellular DNA damage responses (DDR) following unanticipated radiation exposures (*1*). Much progress has been made to increase the sensitivity and throughput of various types of biodosimetry assays (*2*), with the intent that in the event of large-scale radiation incidents, these techniques will allow triaging of exposed individuals so that those with higher likelihood of severe radiation damage can be urgently treated (*3*). In addition, these assays can provide more refined estimates of true physical doses received by exposed individuals.

There are several physical methods to estimate IR dose including radiographic film, thermoluminescent dosimetry, optically stimulated luminescence (OSL) dosimetry, and electron paramagnetic resonance (EPR) measurements of teeth (*4-6*). While these external dosimetry methods may prove useful, they present multiple challenges including issues of sensitivity and concerns over partial-body irradiation scenarios. Furthermore, OSL exposure estimates rapidly degrade when exposed to ambient light (*4, 5*), and EPR analysis is based on a local, rather than a whole body, absorbed dose (*6*). Therefore, additional biological markers that also accurately predict absorbed dose over time after exposure are still needed (*2, 7-10*).

While the dicentric chromosome assay has traditionally been utilized as the "gold-standard" to estimate absorbed dose by measuring dicentric chromosome numbers per cell in mitogen-stimulated peripheral blood lymphocytes, and more recently as a measurement of DNA double-

strand break-associated nuclear foci (*e.g.*, g-H2AX pS139, 53BP1) levels post-irradiation, it is not readily scalable and is time-intensive (*11*). Gene expression analysis, on the other hand, is a robust and well-validated technique that can be quite feasible for screening a large cohort of affected individuals in the case of a disaster scenario, as it can be readily scaled-up and has a rapid turnaround. Thus, recent developments in gene expression profiling have shown that this technique may be a suitable alternative as well as supplement to both physical dosimetry and cytogenetic assays, as it can serve to estimate both whole and partial-body radiation doses in both human and mouse models (12-16). In addition to being less labor intensive, quantitative real-time PCR or microarray-based analyses have shown many biological pathways and genes of interest are modulated in response to IR (*2, 17*), and several highly predictive mRNA and miRNA transcripts have been identified that are predictive of dose in human derived samples (*8, 10, 14*). These studies have proven useful for establishing panels of gene transcripts with increased sensitivity that are rapidly deployable and scalable for application in a disaster scenario.

While most radiation gene expression studies have been focused only on external irradiation scenarios, several groups have recently developed internal irradiation exposure models with an emphasis on mouse-based studies (*13, 15, 16, 18*). Previous gene expression analyses for internal irradiation exposures in humans have typically focused on biomarkers of multiple organ damage (*19-21*), but these did not look for DDR-related signatures in the peripheral blood as a readily available source of biodosimetry markers. More recently, DDR-related signatures in the peripheral blood have been studied in prostate cancer patients undergoing targeted radiation therapy (*22*). In addition, DDR-related signatures in peripheral blood lymphocytes have been seen shortly after patients undergo low-dose radiation treatments for neurological procedures (*23, 24*).

Previous work on internal exposures to ^{131}I-metaiodobenzylguanidine (^{131}I-mIBG), a commonly used targeted radiotherapeutic for advanced neuroblastoma (*25, 26*), has demonstrated the utility of using well known transcripts for biodosimetry amongst DNA repair and apoptosis pathways. We have previously shown that these same transcripts can be applied in chemo-radiotherapy patients as a model system for characterizing internal irradiation exposures to ^{131}I (*27, 28*). In brief, Edmondson et al. characterized the dosimetry of ^{131}I using a three-compartment model in a pilot study of high-risk neuroblastoma patients treated with ^{131}I-mIBG. In that study, an exponential decay curve of ^{131}I activity was measured through a radiation detector that was situated above the patient. We utilized our experimentally derived decay constants from our time-activity curve to estimate total cumulative activity and ultimately mean absorbed dose in these patients. We then performed multiple regression analysis and attained a mathematical equation to estimate gene-expression based dose prediction with time. In short, Edmondson et al. demonstrated that transcripts known to be affected by external irradiation are likewise good indicators of internal IR exposures at 72 and 96 hours post-^{131}I-mIBG treatment (*28*). Campbell et al. also showed that transcripts measured in the peripheral blood at 72 hours may be predictive of treatment toxicities in relapsed and refractory neuroblastoma patients (*27*). Extending these findings to later time points may enhance the utility of IR-specific gene expression panels to correlate biomarkers of patient response to total absorbed dose based on the treatment with ^{131}I-mIBG, as well as identify additional biomarkers that may be predictive of sub-acute toxicities. These transcript panels may also be used as an efficient tool to triage whole and partial-body exposed individuals following an unanticipated irradiation or nuclear incident.

The current study investigates ^{131}I-mIBG therapy-induced gene expression changes in pediatric relapsed and refractory neuroblastoma patients at both 72 hours and 15 days post-

exposure. The goal of this study was to further characterize our established IR-responsive transcripts and evaluate their differential expressions at both 72 hours and 15 days after ^{131}I-mIBG treatment, as compared to untreated baseline samples. To our knowledge, this is the first demonstration of isolating whole blood at 15 days after ^{131}I-mIBG treatment in humans for validating transcripts known to be responsive to both internal and external IR and calculating expression differences in patient peripheral blood. We also demonstrate that our selected transcript panel differentiates between exposed and non-exposed samples 15 days after ^{131}I-mIBG. These findings expand upon our previous studies investigating the biological responses to ^{131}I-mIBG in pediatric neuroblastoma patients and may potentially be extended to predict biomarkers of systemic total body exposures up to 2 weeks following a radiation incident involving internalized isotopes.

2.3 Materials and Methods

Clinical trial patient recruitment and mIBG study

The NANT11-01 trial was a randomized phase II trial comparing response rates in patients with relapsed/refractory mIBG-avid neuroblastoma treated with ^{131}I-mIBG therapy alone, ^{131}I-mIBG with vorinostat (SAHA), or ^{131}I-mIBG with both vincristine and irinotecan (clinicaltrials.gov identifier: NCT02035137). These patients were selected based on several inclusion as well as exclusion criteria as outlined on clinical trials.gov website (clinicaltrials.gov identifier: NCT02035137). All 59 patients in this study were treated with ^{131}I-mIBG 18 mCi/kg [6.66×10^8 Bq/kg] (maximum absolute dose 1200 mCi [4.44×10^{10} Bq]) intravenously over 90 to 120 minutes and received proper thyroid blockade and bladder protection using potassium iodide (6 mg/kg loading dose then 1 mg/kg/dose every 4 hours on Days 1-7 and then 1 mg/kg/dose once

daily on Days 8-43), and a Foley catheter as previously described (29). NANT11-01 included an optional correlative study to evaluate biomarkers of radiation exposure. Patients (or legal guardians for minor subjects) included in the current analysis provided consent for the parent trial and opted in for these gene expression studies. The Institutional Review Board of participating trial sites, as well as the University of California Davis and Lawrence Livermore National Laboratory, approved this study.

Blood sample processing

Peripheral blood was drawn using PAXgene RNA blood tubes (Qiagen) in two separate samples prior to ^{131}I-mIBG treatment (Baseline A and Baseline B) as well as a sample at 72 hours and 15 days after ^{131}I-mIBG exposure (treated). Baseline A was obtained prior to any protocol therapy for all patients. Baseline B for patients on the mIBG only arm was drawn 1-2 days later and reflects no intervening therapy. Baseline B for patients on the other arms of the trial that contain additional putative radiation sensitizers (vorinostat or vincristine/irinotecan) was drawn 1-2 days after Baseline A and reflects the intervening radiation sensitizer therapy but not the effect of mIBG (Figure 2.1). Once ^{131}I-mIBG is administered, this is Day 1, and the 72 hour or 15-day blood draw occurs either 3 days or 15 days after ^{131}I-mIBG treatment. Blood tubes were stored at -80°C for several weeks after IR exposure and before blood processing began, ensuring that the levels of ^{131}I had sufficiently decayed prior to analysis. Total RNA was then extracted using MagMAX™ for Stabilized Blood Tubes RNA Isolation Kit, compatible with PAXgene RNA tubes (Invitrogen) following the manufacturer's instructions. RNA was eluted in 50 µL aliquots and stored at -80°C for later use. RNA was quantified via the NanoDrop™ One^{C} spectrophotometer (Invitrogen) and Qubit 3.0 Fluorometer (Invitrogen). Total RNA was isolated and prepared for

cDNA synthesis prior to quantitative real-time PCR (qPCR) analysis. In total, 288 blood samples were processed for this study. Each patient serves as his or her own control for differential analysis.

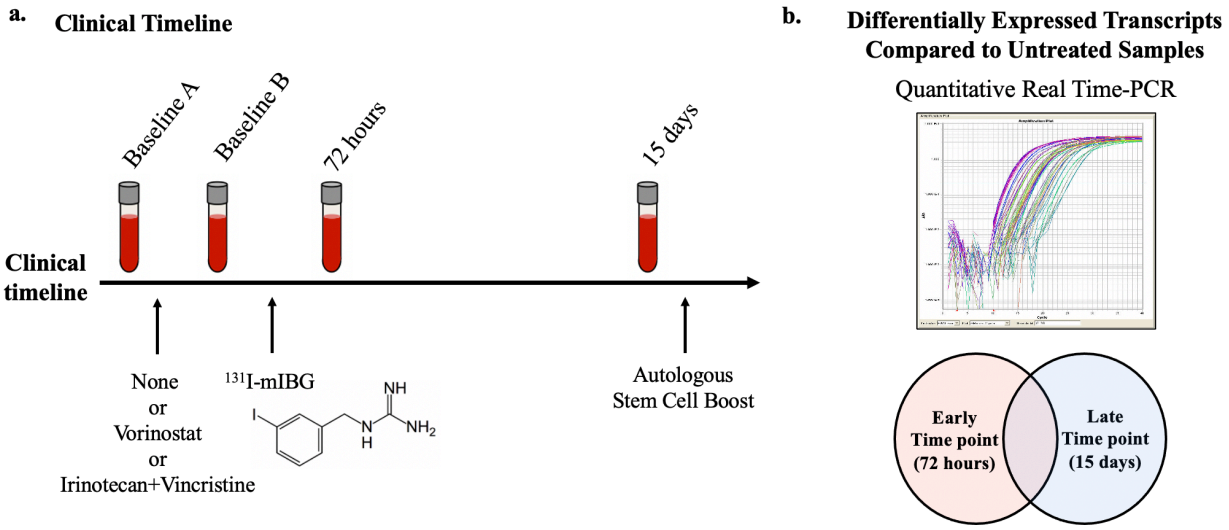

Figure 2.1: Study Design. (a). Patients with relapsed or refractory neuroblastoma were treated with ^{131}I-mIBG alone or in combination with vorinostat or irinotecan/vincristine. Blood was drawn prior to any treatment (Baseline A), as well as after introduction of radiation sensitizers (if necessary, Baseline B). All patients were treated with ^{131}I-mIBG, and ^{131}I-mIBG radiotherapy began after blood draw B. Subsequent peripheral blood was drawn at 72 hours and 15 days after the start of ^{131}I-mIBG infusion. (b). Quantitative real-time PCR was applied to calculate differential transcript expression from the lymphocytes of the peripheral blood. Differential expression of transcripts was calculated at 72 hours and 15 days post ^{131}I-mIBG treatment as compared to untreated controls (Baseline A).

Biodosimetry transcript selection

Previously published irradiation-responsive transcripts were selected for validation within our current study (*8, 30-33*) and are shown in Table 2.1. The GAPDH housekeeping gene was selected for normalization based on our previous findings using multiple housekeeping transcripts in Edmondson et al. (*28*). Most transcripts of interest were downstream effectors of the tumor

suppressor protein 53 (TP53 or p53) pathway. Additional transcripts were associated with pathways involved in cellular stress as well as TP53 DNA damage response (Table 2.1).

Gene	Name	Primer No.	Pathways	Biological Processes
GAPDH	Glyceraldehyde-3-phosphate dehydrogenase	Hs02758991		Glycolysis
CDKN1A	Cyclin dependent kinase inhibitor 1A	Hs00355782	TP53, ErbB , HIF1, FoxO, PI3K/AKT	DNA damage repair, Cell cycle arrest, Apoptosis
FDXR	Ferredoxin reductase	Hs00244586	TP53, Metabolism	Electron Transport
BCL2L1/BCLXL	BCL2 like 1	Hs00236329	Ras MAPK, NFKB, TP53, PI3K/AKT	Apoptosis (anti)
BCL2	B-Cell CLL/Lymphoma 2	Hs99999018	NFKB, HIF1, TP53, PI3K/AKT	Apoptosis (anti)
BAX	BCL2 Associated X Protein	Hs99999001	TP53	Apoptosis (pro)
DDB2	Damage Specific DNA Binding Protein 2	Hs03044953	TP53	Nucleotide Excision Repair
PRKDC	Protein Kinase, DNA-Activated, Catalytic Polypeptide	Hs04195439	TP53, PI3K.AKT	DNA repair
GADD45A	Growth Arrest And DNA Damage Inducible Alpha	Hs00169255	MAPK, FoxO, TP53, Cell Cycle, p38 JNK	Cell cycle, Cellular Stress
STAT5B	Signal Transducer And Activator Of Transcription 5B	Hs00273500	TCR Signaling	Transcription Activator
XPC	Xeroderma Pigmentosum, Complementation Group C	Hs00190295	TP53	DNA damage repair
BBC3	BCL2 Binding Component 3	Hs00248075	TP53	Apoptosis (pro)
SESN1	Sestrin 1	Hs00205427	TP53	DNA damage, Oxidative stress
POLH	DNA Polymerase Eta	Hs00982625	TP53	DNA repair
IGF1R	Insulin-Like Growth Factor 1 Receptor	Hs00181385	PI3K/AKT, Ras MAPK	Tyrosine kinase activity, Cell growth and survival, Apoptosis (anti)
SGK1	Serum/Glucocorticoid Regulated Kinase 1	Hs00985033	TP53, Ras MAPK	Cellular Stress
PCNA	Proliferating Cell Nuclear Antigen	Hs00427214	TP53	DNA repair
MDM2	Mouse Double Minute 2	Hs00234753	TP53, PI3K/AKT, FoxO	Cell cycle arrest, Apoptosis (anti)

Table 2.1: Selected transcripts of interest for quantitative real-time PCR (qPCR).

cDNA synthesis

In preparation for quantitative real-time PCR (qPCR), 200 ng of RNA was converted to cDNA via the High-Capacity RNA-to-cDNA kit (Applied Biosystems, Foster City, CA). If RNA was too dilute, it was concentrated via Speedvac 2.0 (Savant, DNA SpeedVac 120) prior to cDNA synthesis. The cDNA synthesis reactions incubated in a thermocycler at 37°C for 60 minutes, 95°C for 5 minutes, and then held at 4°C. Once complete, the cDNA was pre-amplified with Taqman™ PreAmp Master Mix (Applied Biosystems, Foster City, CA). A custom pooled assay mix of TaqMan primers, including all 18 transcripts for this study, were combined along with the cDNA template and the Taqman™ PreAmp master mix. Reactions pre-amplified at 95°C for 10 minutes,

followed by 14 cycles of (95°C for 15 seconds, 60°C for 4 minutes) in a thermocycler. After pre-amplification, reactions were diluted 20-fold in 1X TE buffer and stored at -15°C to -25°C in preparation for qPCR.

Quantitative real-time PCR (qPCR)

Quantitative real-time PCR was used to analyze the transcript expression level differences for each patient at each exposure time point. Each reaction used 5x TUFF TAQ QPCR Master Mix+Rox (Rebel Bioscience, Portland, OR), TaqMan™ primers (Table 2.1), pre-amplified cDNA, and nuclease-free water for a total volume of 25 µL per reaction. Each transcript was analyzed in triplicate. Reactions were placed in a 7900HT Fast Real-Time PCR machine (Applied Biosystems, Foster City, CA). The following parameters were used: 95°C for 10 minutes, followed by 40 cycles of (95°C for 15 seconds, 60°C for 1 minute). The cycle threshold (Ct) values from the qPCR curves were extracted at the logarithmic growth phase of the curve. The delta-delta Ct methods was used to calculate the fold changes ($2^{-\Delta\Delta Ct}$), as previously described (*28*). The $\log_2$ of the linear fold changes was calculated for comparisons.

Statistics and analysis

For qPCR, the $2^{-\Delta\Delta Ct}$ was used to calculate the fold change, as previously published (*28*). A p-value of 0.05 was used as a cutoff to determine statistical significance. P-values are labeled as <0.05 (*), <0.01 (**), <0.001 (***), and <0.0001 (****) throughout the manuscript.

At 72 hours and 15 days post-^{131}I-mIBG, patient fold changes were calculated with respect to Baseline A (untreated) expression levels across all patient sets. Each baseline sample was analyzed in the same manner as the exposed samples. Fold changes between Baseline B and Baseline A

samples account for either normal variability in the baseline data (^{131}I-mIBG only group) or the effects of the additional drug(s) (vorinostat or vincristine/irinotecan patients) prior to irradiation exposure. The "Baseline" fold changes (Baseline B versus Baseline A) were then used for comparisons with later time points. Thus, any variability under the "Baseline" fold change will account for the potential effect(s) of the radiation sensitizers when comparing to fold changes at 72 hours or 15 days after ^{131}I-mIBG treatment. The $\log_2$ of the linear fold changes were calculated and multiple t-tests were performed to determine significance between various time points. Data plotting and t-tests used GraphPad software.

Calculated kinetic model (Km) doses at 72 hours were determined based on absolute mCi of ^{131}I-mIBG received and fitted to the linear decay curve as previously described (*28*). A linear regression model was then derived using the top priority transcript fold changes to generate a gene expression-based dose (GE) as previously described (*28*). Predicted doses for 32 random samples (16 at 72 hours and 16 unexposed) were fit using our newly derived gene expression based linear regression model (Table 2.3), along with prediction intervals (PI) and confidence intervals (CI).

Partial Least Squares Discriminant Analysis

As a preliminary assessment for how strongly $\log_2$ transformed transcripts can predict whether a patient has been exposed (72 hours or 15 days after treatment) from unexposed patients (prior to treatment), we used partial-least squares discriminant analysis (PLS-DA). PLS-DA is a linear classification model generated from data that can be used to classify new samples. PLS-DA was applied using only the top 7 transcripts (*CDKN1A*, *FDXR*, *BAX*, *BCL2*, *BCL2L1*, *DDB2*, and *PRKDC*) at 72 hours, and two PLS-DA runs were applied to 15-day samples (top 7 transcripts and all transcripts). We assessed generalizability of the model by performing leave-one-out cross-

validation. We calculated sensitivity, specificity, and area under the curve (AUC) as measures of model performance. Implementation of PLS-DA was done using the R package 'mixOmics' (*34*).

2.4 Results

Patient and sample characteristics

Fifty-nine pediatric patients with relapsed or refractory neuroblastoma provided samples for the current analysis (Figure 2.1). There were 25 males and 34 females included in this analysis. The ages of the patients range from 1-26, with a mean age of 7. There were 22 of the 59 patients that received two rounds of ^{131}I-mIBG treatment (four ^{131}I-mIBG alone, nine ^{131}I-mIBG+vincristine/irinotecan patients, and nine ^{131}I-mIBG+vorinostat patients), and we received samples from only a second course of treatment from one patient (^{131}I-mIBG+vincristine/irinotecan). We confirmed with this dataset our previous findings that our gene expression transcript panel was not statistically different following the second course of treatment compared to the first course of treatment (Figure 2.2, (*28*)). Thus, individuals who had a previous course of treatment were analyzed independently of their second course of treatment. Altogether, there were 81 patient sets (courses of treatment) in this study (20 ^{131}I-mIBG only, 31 ^{131}I-mIBG +vincristine/irinotecan, and 30 ^{131}I-mIBG +vorinostat). One patient set did not have a 72-hour time point and only had baseline and 15-day blood draws. In total, there were 80 patient sets with a 72-hour timepoint (57 patient sets from Course 1 and 23 patient sets from Course 2, with one patient set only having received Course 2 samples) and 16 patient sets at the 15-day time point (12 patient sets from Course 1 and 4 patient sets from Course 2, with one patient set only having received Course 2 samples). Transcripts *GAPDH*, *CDKN1A*, *FDXR*, *BAX*, *BCL2*, *BCL2L1*, *DDB2*, and *PRKDC* were considered our top priority transcripts and were analyzed with all 58 patients (n=80

courses of treatment) at 72 hours and all 13 patients (n=16 courses of treatment) at 15 days. Second priority transcripts *GADD45A*, *XPC*, *STAT5B*, *SESN1*, *POLH*, *BBC3*, *PCNA*, *IGF1R*, and *SGK1* comprised of 12 patients (n=14 courses of treatment) at 15 days or 26 patients (n=31 courses of treatment) at 72 hours. *MDM2* was added to the transcript panel after many samples had already been analyzed and comprised of 12 patients (n=14 courses of treatment) at 15 days or 11 patients (n=13 courses of treatment) at 72 hours. The total number of patients, total courses of treatment, p-values, and FDR values for all transcripts at both 72 hours and 15 days as compared to untreated controls are summarized in Table 2.2. RNA yield varied between 4.7 and 574 ng/µl, with average A260/280 absorbance values of 2.2, and A260/230 absorbance values of 0.9 across all samples. The mean RIN value collected was 8. Our analysis focused on differentially expressed transcripts within these patient sets for comparing early (72 hours) and late (15-day) responses after ^{131}I-mIBG via quantitative real-time PCR (Table 2.1, Figure 2.1b).

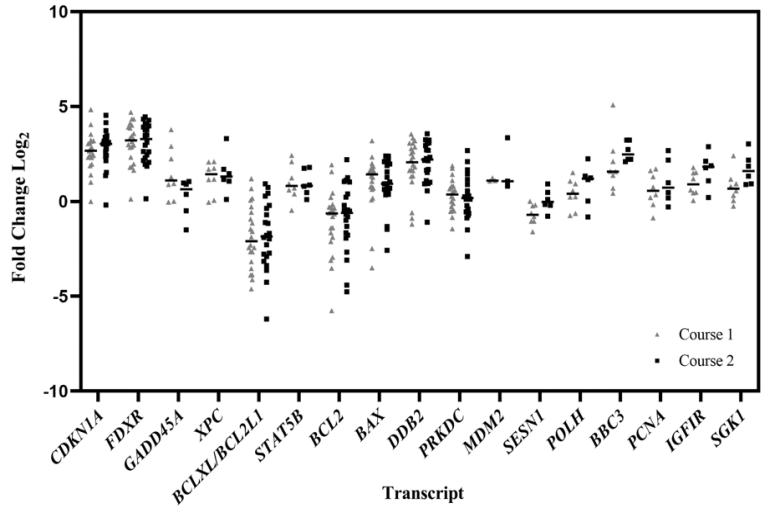

Transcript	P value	FDR (q value)
CDKN1A	0.448492	0.944136
FDXR	0.952539	>0.999999
GADD45A	0.078130	0.464874
XPC	0.667585	0.944136
BCLXL/BCL2L1	0.886644	>0.999999
STAT5B	0.949352	>0.999999
BCL2	0.647904	0.944136
BAX	0.811385	>0.999999
DDB2	0.658709	0.944136
PRKDC	0.687606	0.944136
MDM2	0.498140	0.944136
SESN1	0.028622	0.458009
POLH	0.369519	0.944136
BBC3	0.295827	0.944136
PCNA	0.467459	0.944136
IGFIR	0.110212	0.491820
SGK1	0.051318	0.458009

Fig. 2.2: Course of treatment does not dramatically alter gene expression findings. Quantitative real-time PCR was used to determine fold change differences amongst patients between his or her first and second course of treatment. No transcripts were determined to be statistically different at 72 hours between courses based on an unpaired t-test with two-stage step-up (Benjamini, Krieger, and Yekutieli). Each dot represents one patient, and the black bar represents the median $\log_2$ fold change.

Transcript	Timepoint	Total Patients	Total courses of treatment	P-value	FDR
CDKN1A	72 hrs	58	80	<0.000001	<0.000001
	15 days	13	16	0.441898	0.372254
FDXR	72 hrs	58	80	<0.000001	<0.000001
	15 days	13	16	0.011147	0.013760
GADD45A	72 hrs	26	31	0.000344	0.000232
	15 days	12	14	0.880141	0.586203
XPC	72 hrs	26	31	0.000002	0.000001
	15 days	12	14	0.028870	0.031669
BCLXL/BCL2L1	72 hrs	58	80	<0.000001	<0.000001
	15 days	13	16	0.896980	0.586203
STAT5B	72 hrs	26	31	0.000394	0.000239
	15 days	12	14	0.007300	0.011586
BCL2	72 hrs	58	80	0.020016	0.007135
	15 days	13	16	0.002583	0.004783
BAX	72 hrs	58	80	<0.000001	<0.000001
	15 days	13	16	0.812857	0.586203
DDB2	72 hrs	58	80	<0.000001	<0.000001
	15 days	13	16	0.031355	0.031669
PRKDC	72 hrs	58	80	0.014392	0.005814
	15 days	13	16	0.001428	0.003967
MDM2	72 hrs	11	13	0.011317	0.005171
	15 days	12	14	0.002145	0.004767
SESN1	72 hrs	26	31	0.015751	0.005966
	15 days	12	14	0.000287	0.002762
POLH	72 hrs	26	31	0.011946	0.005171
	15 days	12	14	0.000746	0.002762
BBC3	72 hrs	26	31	<0.000001	<0.000001
	15 days	12	14	0.232644	0.215389
PCNA	72 hrs	26	31	0.002399	0.001321
	15 days	12	14	0.469087	0.372254
IGF1R	72 hrs	26	31	<0.000001	<0.000001
	15 days	12	14	0.000500	0.002762
SGK1	72 hrs	26	31	0.011909	0.005171
	15 days	12	14	0.009254	0.012851

Table 2.2: Transcript statistics at the early (72 hour) or late (15-day) time points.

^{131}I-mIBG exposure alters early gene expression levels compared to baseline

Figure 2.3a shows the range of transcript fold changes at 72 hours as compared to Baseline A samples. Overall, 17 transcripts demonstrated significant gene expression differences at 72 hours as compared to baseline controls, with 14 transcripts displaying significant up-regulation and 3 transcripts demonstrating significant down-regulation (Figure 2.3a, Appendix Figure A.2.1). At 72 hours post ^{131}I-mIBG treatment, the average $\log_2$ transformed fold changes across the transcript

panel ranged from -1.786 (*BCL2L1*) to +2.930 (*FDXR*) across all 80 patient sets. Several transcripts demonstrated significant up-regulation, including *CDKN1A* (p<0.000001), *FDXR* (p<0.000001), *DDB2* (p<0.000001), and BBC3 (p<0.000001) (Figure 2.3a, Appendix Figure A.2.1). *FDXR* showed the highest levels of up-regulation at 72 hours, with the median linear fold change of 7.77, and peak linear fold change of 25.85. *BCLXL* was heavily down-regulated at 72 hours, with median linear fold change of 0.277 (about 1.85 fold down-regulated) over baseline samples (untreated controls).

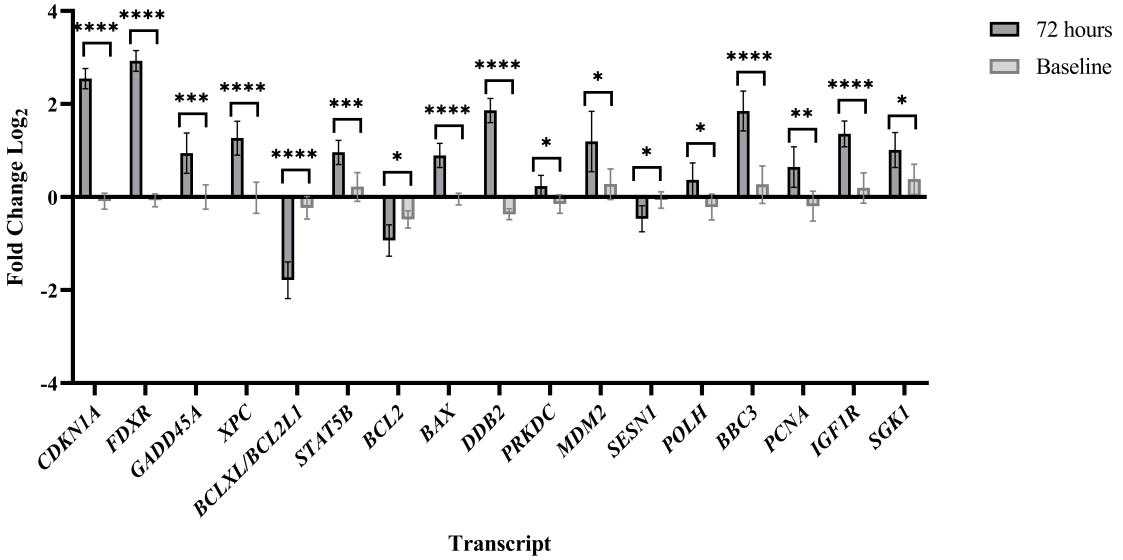

Figure 2.3a. Differential expression 72 hours after ^{131}I-mIBG radiotherapy. Quantitative real-time PCR demonstrates 17 statistically significant transcripts at 72 hours post ^{131}I-mIBG treatment. Differential expression from 58 patients and 80 courses of treatment are shown for our top priority transcripts. Shown is the mean $\log_2$ fold change with 95% Confidence Intervals. All fold changes are with respect to untreated blood draw A (Baseline A).

Multiple transcripts are differentially expressed 15 days after ^{131}I-mIBG exposure

Similar to the early exposed samples, all transcripts selected were measurable in qPCR assays 15 days after ^{131}I-mIBG treatment and a Baseline B to Baseline A (untreated control) fold change comparison was used to negate potential confounding factors from the radiosensitizer(s) (Figure

2.3b). Nine transcripts were significantly down-regulated at 15 days compared to untreated controls, including *BCL2* (p=0.002583), *XPC* (p=0.028870), *STAT5B* (p=0.007300), *MDM2* (p=0.002145), *PRKDC* (p=0.001428), *SESN1* (p=0.000287), *IGF1R* (p=0.0005), *POLH* (p=0.000746), and *SGK1* (p=0.009254) (Figure 2.3b, Appendix Figure A.2.2). *FDXR* and *DDB2* (p=0.01 and 0.03, respectively) maintained significant up-regulation at 15 days post exposure. Additionally, *BCL2* and *SESN1* expression remained down-regulated at both 72 hours and 15 days (Figure 2.4). Interestingly, *STAT5B*, *XPC*, *MDM2*, *PRKDC*, *POLH*, *SGK1*, and *IGF1R* were significantly up-regulated at 72 hours but were significantly down-regulated at 15 days (Figure 2.4, Appendix Figures A.2.1-A.2.2). Expression levels of six irradiation-responsive transcripts at early time points (*CDKN1A*, *GADD45A*, *BCL2L1*, *BAX*, *BBC3*, and *PCNA*) did not display any differential expression at 15 days as compared to untreated controls, indicating a return to baseline expression levels (Figure 2.3b, Figure 2.4).

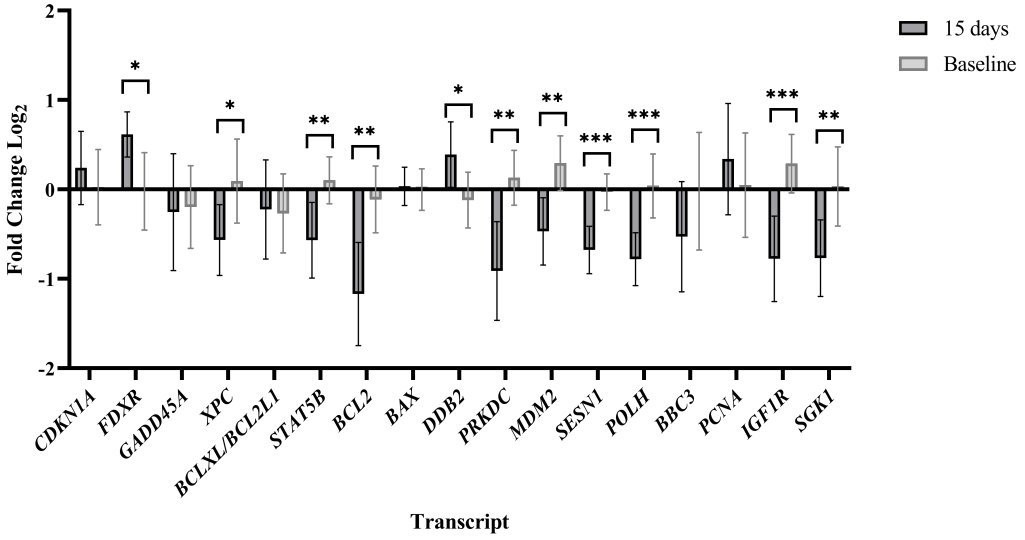

Figure 2.3b. Differential expression 15 days after ^{131}I-mIBG radiotherapy. Quantitative real-time PCR determined 11 statistically significant transcripts 15 days post ^{131}I-mIBG treatment. *SESN1*, *POLH*, and *IGF1R* displayed the most significant down-regulation from Baseline ($p<0.001$). Shown is the mean $\log_2$ fold change with 95% Confidence Intervals. All fold changes are with respect to untreated blood draw A (Baseline A).

Comparison between early and late time points show differences in gene expression

Given the differential gene expression changes between early (72 hours) and late (15-day) time points compared to untreated controls, we next sought to compare differences between 72 hours and 15 days independently. Here, the $\log_2$ fold changes at both time points were calculated with respect to untreated Baseline A. Fourteen transcripts demonstrated significant modulation between early and late time points after ^{131}I-mIBG treatment (Figure 2.3c, Appendix Figure A.2.3). Fold changes for thirteen of the fourteen transcripts were up-regulated at 72 hours after exposure, and subsequently down-regulated at day 15. The only transcript that displayed significant down-regulation at 72 hours as compared to 15 days was *BCL2L1*, an anti-apoptotic marker (Figure 2.3c, Appendix Figure A.2.3).

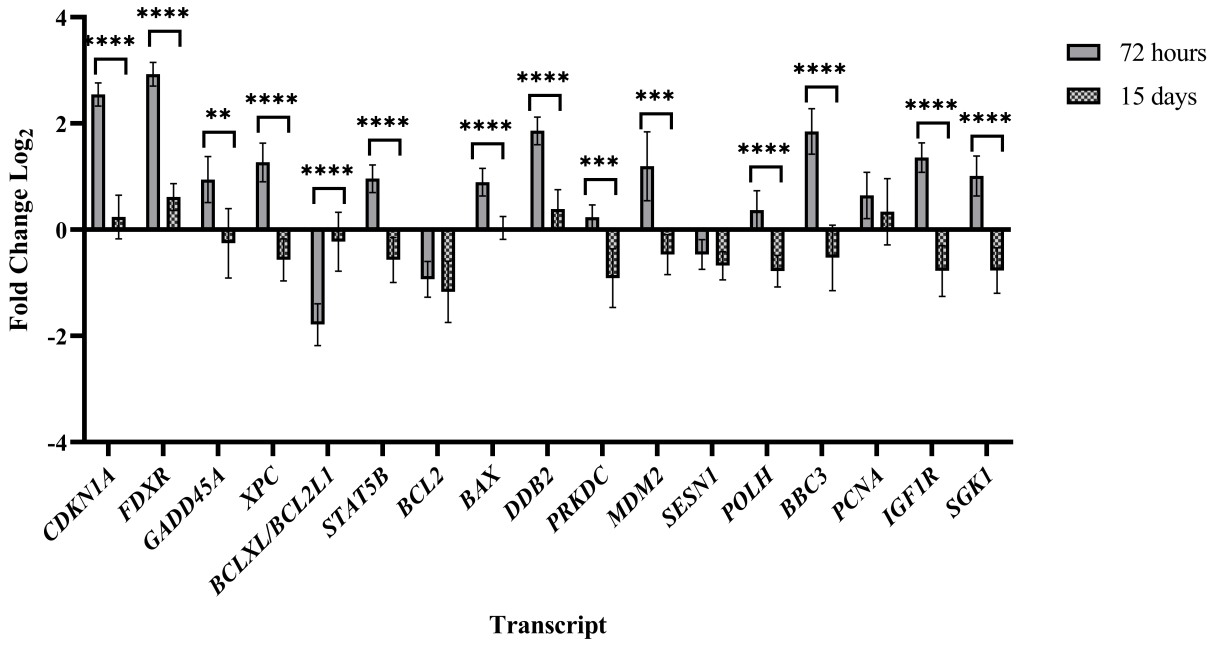

Figure 2.3c. Observational expression level differences between early and late time points. Quantitative real-time PCR determined fold change fluctuations between early and late time points after^{131}I-mIBG treatment. Shown are the mean $\log_2$ fold changes with 95% Confidence Intervals. All fold changes are with respect to untreated blood draw A (Baseline A).

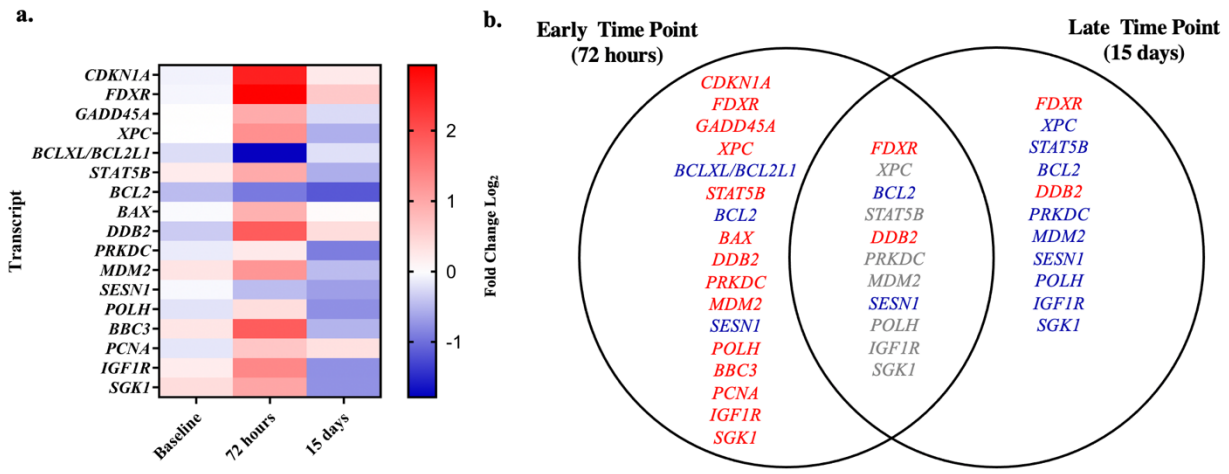

Figure 2.4: Transcripts levels fluctuate between early and late time points. (a). Heatmap of average $\log_2$ fold changes across time points. Baseline fold change refers to the Baseline B vs Baseline A comparison. All fold changes are with respect to Baseline A. (b). Venn diagram illustrates the differentially expressed transcripts at 72 hours, 15 days, or the overlap between both time points. Transcript coloring is as follows: up-regulated transcripts (red), down-regulated transcripts (blue), differential expression at both timepoints, but in reverse directions when compared to baseline (gray). All fold changes are $\log_2$ transformed and were compared to Baseline A. Differential gene expression cutoff was $p<0.05$.

Gene expression-based dose prediction is consistent at 72 hours but inconclusive at 15 days

We calculated absorbed doses for all 80 patient sets at 72 hours using the three-compartment biokinetic model based on the ^{131}I decay curve, amount of injected ^{131}I-mIBG activity, and patient body weight as previously described (*28*). These doses were termed kinetic model (Km) doses. We then applied a linear regression model on a random pool of 32 patient sets (16 treated at 72 hours and 16 untreated) to predict dose based on gene expression values. We focused only on the top 7 priority transcripts (*CDKN1A*, *FDXR*, *BAX*, *BCL2*, *BCL2L1*, *DDB2*, and *PRKDC*) for our gene expression dose estimation to ensure that all patients contained full datasets. Predicted doses based on the gene expression (GE) model fall between 1.55–2.97 Gy, and

calculated Km doses for these 16 treated samples fall within 2.3–2.88 Gy with an R^2 value of ~0.89, suggesting that a linear regression model remains robust for predicting dose values in subjects exposed to ^{131}I-mIBG (Table 2.3). We then performed PLS-DA with Leave-One-Out Cross Validation (LOO-CV) using the same top 7 transcripts on all 160 samples at 72 hours (80 treated and 80 untreated) to predict exposed from unexposed individuals. LOO-CV predicted exposed from unexposed samples with 98% specificity and 92.5% sensitivity (Table 2.4).

Because our previously published three-compartment model only encompassed data up to 120 hours, we could not use this model to predict doses at 15 days. Therefore, we used the amount of injected ^{131}I-mIBG activity (mCi) to calculate the absorbed dose at 15 days using the Equations 1-3 from our previous pilot study (*28*) in an attempt to calculate dose based on gene expression at the 15-day time point. The resulting doses from the biokinetic model were termed "observed" doses. We then performed linear regression and LOO-CV to create a gene expression model that would be relevant at 15 days. Using our newly derived 15-day gene expression-based model, we predicted total dose absorbed at 15 days as compared to the observed dose from the biokinetic model (data not shown). Predicted doses from the 15-day gene expression results ($\log_2$ fold change compared to Baseline A) were indistinguishable from the predicted dose using untreated baseline samples (Time 0; $\log_2$ fold change comparing Baseline B to Baseline A). This suggests that 15 days may be too late to retrieve an accurate gene-expression based dose estimation reading within the peripheral blood from internal ^{131}I.

Patient Set	Km Dose	GE Dose (Fit)	Lower PI	Upper PI	Lower CI	Upper CI
1	246.25	215.50	113.88	317.13	184.44	246.56
2	283.88	269.84	170.63	369.05	247.95	291.73
3	256.56	261.98	163.21	360.75	242.16	281.80
4	233.92	225.61	126.12	325.11	202.45	248.78
5	251.26	245.56	143.52	347.60	213.18	277.94
6	250.75	155.45	57.19	253.72	138.36	172.55
7	275.89	242.50	144.78	340.21	228.88	256.12
8	254.95	252.93	154.00	351.86	232.36	273.51
9	272.85	237.56	139.65	335.47	222.63	252.49
10	271.75	215.67	117.81	313.52	201.10	230.24
11	259.26	281.64	178.13	385.15	244.89	318.39
12	267.24	254.53	155.60	353.47	233.92	275.14
13	256.56	181.26	83.54	278.98	167.63	194.90
14	275.89	221.45	118.75	324.16	187.04	255.87
15	275.02	257.70	157.67	357.74	232.34	283.07
16	288.13	297.31	197.49	397.13	272.78	321.84
1	0	-32.06	-129.99	65.87	-47.10	-17.02
2	0	10.91	-88.53	110.36	-12.01	33.84
3	0	-24.50	-122.17	73.17	-37.78	-11.21
4	0	-7.15	-110.04	95.73	-42.10	27.80
5	0	6.67	-91.06	104.41	-7.10	20.45
6	0	-66.40	-163.97	31.16	-78.88	-53.92
7	0	-29.87	-127.21	67.47	-40.41	-19.32
8	0	-7.96	-105.11	89.18	-16.51	0.58
9	0	1.77	-95.04	98.57	-1.15	4.68
10	0	-5.00	-102.81	92.81	-19.28	9.28
11	0	28.87	-74.45	132.18	-7.34	65.07
12	0	8.23	-88.83	105.29	0.63	15.84
13	0	-19.41	-116.86	78.03	-30.89	-7.93
14	0	20.43	-77.70	118.55	4.15	36.71
15	0	-7.02	-105.10	91.06	-23.02	8.98
16	0	-11.73	-109.07	85.61	-22.31	-1.16

Table 2.3: Gene expression dose prediction at 72 hours using a linear regression model

	N unexposed	N exposed	AUC	Specificity	Sensitivity
LOO-CV Results	80	80	0.9892	0.9875	0.925

Table 2.4: Leave One Out Cross Validation (LOO-CV) at 72 hours on 160 blood samples predicted exposed vs. unexposed with over 98% specificity.

Transcripts are strongly predictive of exposure status out to 15 days

Although accurate or absolute dose prediction was inconclusive at 15 days, we next sought to investigate if our gene expression panel could distinguish IR-exposed from unexposed

individuals at 15 days. Thus, we generated a predictive two-component PLS-DA model using gene expression results from 16 patients sets (Figure 2.5). We ran PLS-DA with LOO-CV on our top 7 priority transcripts and predicted exposed vs. unexposed samples with 87.5% specificity, 87.5% sensitivity and an R^2 value of ~0.9 (Figure 2.5, Table 2.5). All 16 exposed samples were correctly identified as exposed, and only 1 false positive sample was incorrectly predicted as exposed (Figure 2.5). We also performed PLS-DA and LOO-CV on our complete 17 transcript panel and found it to be slightly more specific than our top 7 transcripts alone, with 94% specificity and 87.5% sensitivity (Figure 2.6, Table 2.5).

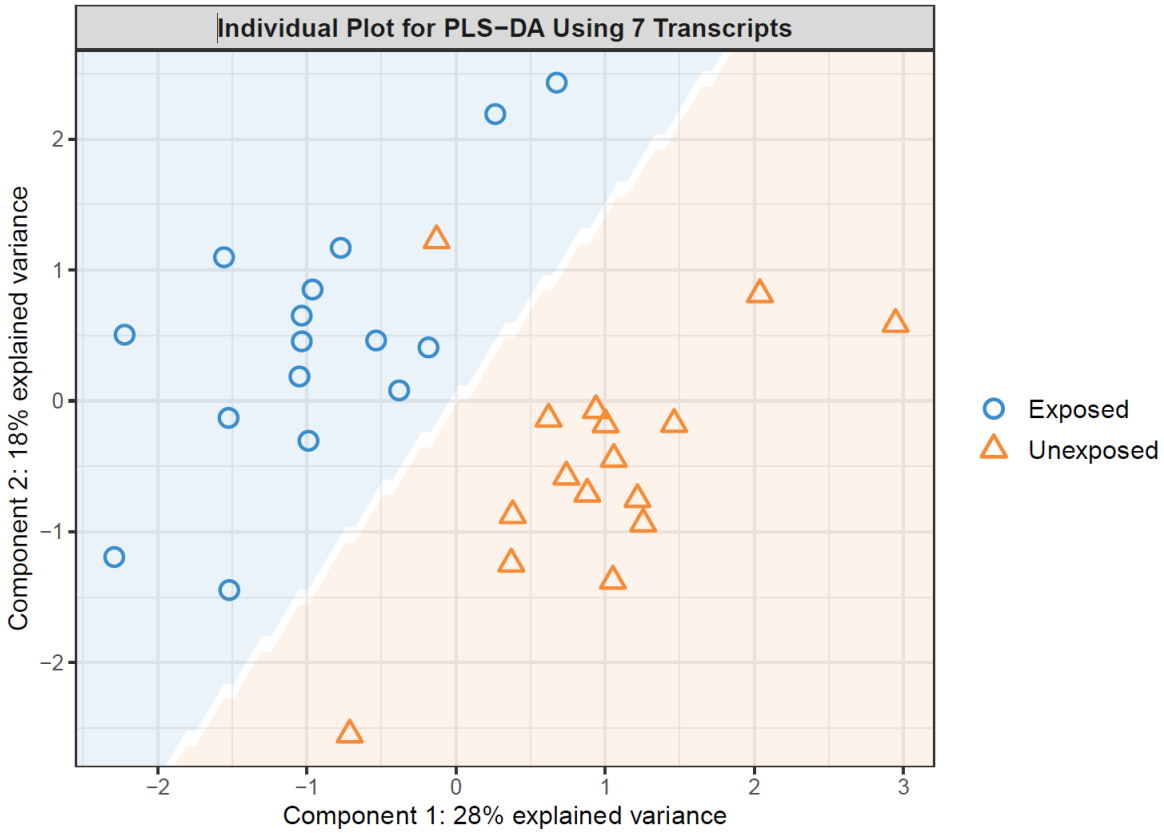

Figure 2.5: Top 7 transcript panel differentiates exposed from non-exposed out to 15 days. A predictive two-component PLS-DA model comprised of *CDKN1A*, *FDXR*, *DDB2*, *BCL2*, *BCL2L1*, *DDB2*, and *PRKDC* identified exposed versus unexposed samples with 87.5% specificity. The color of the background represents the predicted label, and the icons are representative of the actual label.

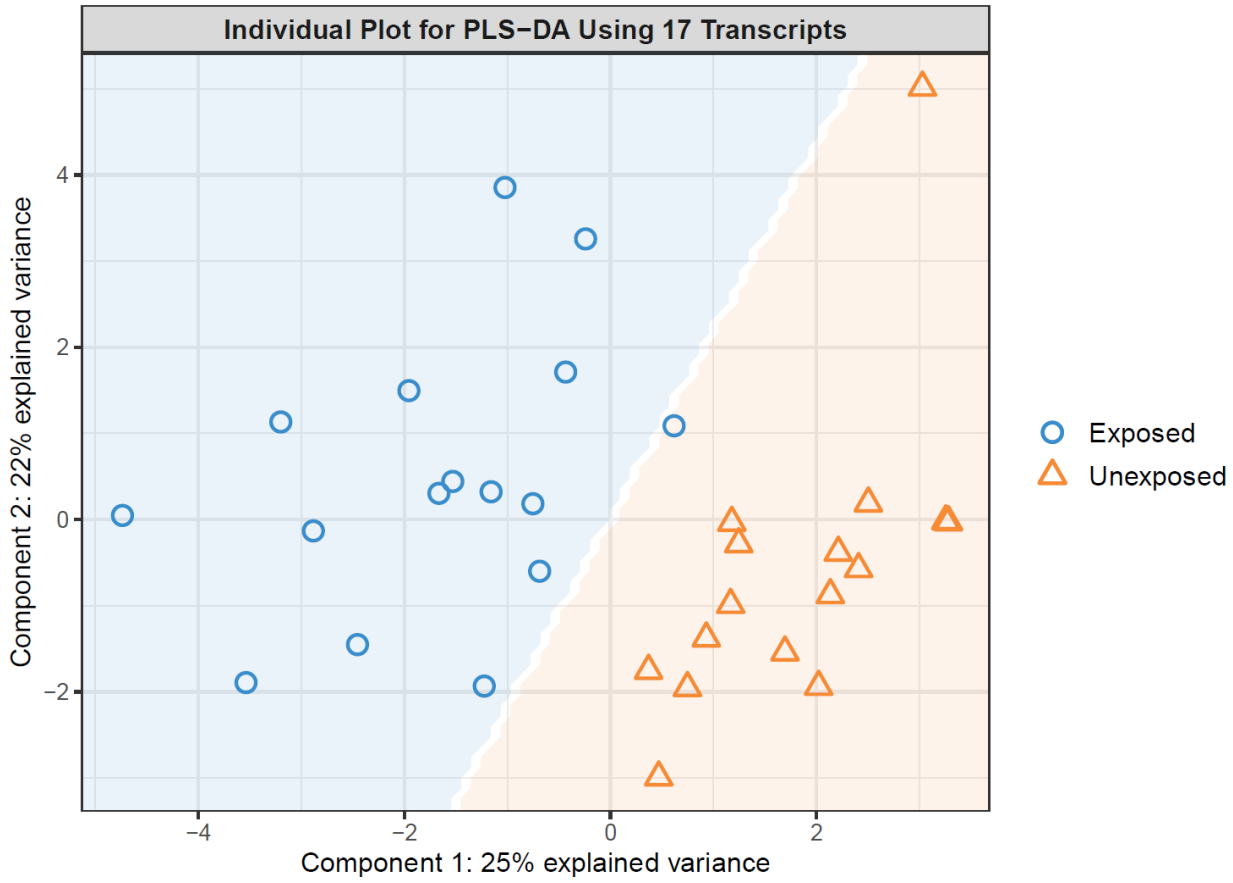

Figure 2.6: PLS-DA on entire transcript panel mimics Top 7 findings to differentiate exposed from non-exposed out to 15 days. A predictive two-component PLS-DA model using all transcript data collected identified exposed versus unexposed samples with ~94% specificity and ~88% sensitivity. The color of the background represents the predicted label, and the icons are representative of the actual label.

	N unexposed	N exposed	AUC	Specificity	Sensitivity	
LOO-CV Results	16	16	0.8594	0.875	0.875	***Top Priority Transcripts***
LOO-CV Results	16	16	0.9648	0.9375	0.875	***All Transcripts***

Table 2.5: Leave One Out Cross-Validation (LOO-CV) on Top Priority Transcripts Predicts Exposed from Unexposed at 15 days

2.5 Discussion

This study demonstrates the utility of using biodosimetry gene expression panels established for external irradiation scenarios for internalized ^{131}I exposures (and may be generally applicable to other internal radioisotopes) over later time points. Importantly, the data are derived directly from pediatric patients, an under-represented population rarely included in radiation exposure studies. These data were also useful for detecting transcriptional differences between early (3 day) and late (15-day) time points after ^{131}I-mIBG treatment in human chemo-radiotherapeutic patients using known IR-responsive gene transcripts. Furthermore, our findings demonstrate that this gene expression panel is useful for predicting exposed from unexposed individuals out to 15 days and could accurately triage the exposed population with as little as 7 selected transcripts. These data may be useful in the event of a large-scale disaster between 3 days and up to 2 weeks after an initial exposure, allowing clinical assistance and resources to funnel to those in need while reassuring the worried well.

Previous external and internal biodosimetry studies provided transcript analysis usually within 3 days of exposure (10, 12, 14, 27, 28). To our knowledge, our study is unique in that it demonstrates the strength of using peripheral blood as a biomarker of DNA damage-related responses to internal 131I in humans up to 15 days after exposure, demonstrating further utility for expression panels with common transcripts of interest. We chose our two time points of interest, 72 hours and 15 days, because they align nicely with the treatment plan for these relapsed/refractory neuroblastoma patients. There are radiation safety concerns with obtaining blood samples prior to 72 hours after 131I-mIBG treatment. Thus, 72 hours (3 days) serves as our early time point. The 15-day time point was chosen as patients are clinically treated with an autologous stem cell boost at that time.

We utilized an expanded panel of TP53, PI3K/AKT, and MAPK-regulated transcripts and found that certain predictors of early exposure did not overlap with the later time point of 15 days. These data demonstrate that at 72 hours of exposure, *CDKN1A*, *GADD45A*, *BAX*, *BBC3*, *PCNA*, and *BCL2L1* were key indicators of internal ^{131}I exposure, however, transcript fluctuations were time-dependent and were not significant at the later time point as compared to untreated controls. This demonstrates that these transcripts may be useful as early biomarkers of more recent ^{131}I exposures that could likewise be relevant to other beta-emitting radioisotopes of concern such as ^{90}Sr and ^{137}Cs. We also identified four transcripts that continued to maintain consistent gene expression differences at both early (72-hour) and late (15-day) points: *FDXR*, *DDB2*, *BCL2*, and *SESN1*. These transcripts may serve as novel biomarkers useful for triaging those exposed at both early and late time points, especially in the event of a nuclear disaster, where it may not be feasible to triage the entire exposed population from the worried well within three days. We also found that *STAT5B*, *XPC*, *MDM2*, *PRKDC*, *POLH*, *SGK1*, and *IGF1R* were the only transcripts in this study to be significantly up-regulated at the early time point and significantly down-regulated at the late time point. This indicates that these transcripts may be more sensitive to small changes in relevant IR-responsive cell cycle and DNA damage response pathways, such as those mediated by TP53. This may also indicate transcripts that are susceptible to long-term toxicities associated with treatment, such as immune modulation and hematopoietic stem cell depletion/dysfunction associated with ^{131}I-mIBG treatment at later time points. It should also be noted that gene expression levels continued to change at 15 days post-treatment, as most transcripts had not returned to baseline levels.

Our biodosimetry panel focused on several TP53-regulated transcripts of interest that have been previously identified as responsive to early irradiation exposures of ≤3 days (*35*). These

results coincide with previous reports of *ex-vivo* irradiated samples from human peripheral blood, validating *FDXR* and *CDKN1A* as important biomarkers of early exposure for both internal and external sources of irradiation (*14, 36*). Other external irradiation studies of TP53-responsive genes included *DDB2* and *MDM2*, which were also significantly up-regulated upon early exposures (*35, 37*). Although previous studies have investigated *CDKN1A*, *FDXR*, *MDM2*, and *DDB2* as candidate up-regulated biomarkers of IR exposure (*30, 35, 36*), our study expands upon these findings to validate these transcripts as biomarkers of internal ^{131}I exposure at early time points. Similar to what we have seen previously in neuroblastoma patients, *CDKN1A* and *MDM2* also displayed a time-dependent up-regulation at 72 hours and decreased with later time points (*28*). Interestingly, our study identified *FDXR* and *DDB2* as biomarkers of both early and late exposures, maintaining consistent up-regulation at 72 hours and 15 days as compared to untreated controls.

We found that at 15 days the fold changes of our transcript panel differed from those at 72 hours. We identified nine transcripts significantly down-regulated at day 15 as compared to untreated controls, which may indicate a delayed recovery response of these genes to return to normal levels from the effects of internal ^{131}I-mIBG exposure. It is also possible that the biological effects of ^{131}I may still be contributing to these transcript fluctuations at day 15, as the physical half-life of ^{131}I is ~8 days and there is still ongoing exposure 15 days after treatment initiation. This finding that transcripts are still fluctuating after two weeks of exposure will need to be considered when triaging and treating individuals long after an irradiation incident.

Here, we suggest that many transcripts initially designated as early biomarkers of ionizing radiation exposure are no longer predictive biomarkers of exposure out to 15 days. In contrast to transcripts that we identified that are indicative of early exposures, we found that *BCL2* and *SESN1* remained significantly down-regulated at 15 days, indicating that DDR and apoptotic pathways

may still be dysregulated at later time points. These transcripts differ from the standard transcripts studied with early exposures and may be relevant and impactful biomarkers at late exposures out to 15 days, where gene expression levels are still changing.

Among the essential features of this model system is the well-defined patient exposure history, where samples were collected at both early and late time points post-^{131}I-mIBG treatment. Moreover, each subject provided blood before and after exposure, so that each individual acts as his or her own control. Furthermore, we utilized robust qPCR assays that are used in exposure scenarios over an extensive amount of irradiation studies (*35*) and that have been previously validated as an accurate and reproducible method for analyzing ^{131}I-mIBG patient samples (*38*). This model system is also ideal for detecting biomarkers of acute toxicity (*27*) and extrapolating absorbed dose estimates from ^{131}I-mIBG exposures (*28*).

Despite the quick and reliable detection methods of qPCR, there is still a need for larger gene expression studies to better understand the overall association between transcripts and physiological effects associated with exposure outcomes. Another limitation of qPCR is that it is directed towards a specific transcript panel of interest, and it is not feasible for analyzing thousands of genes at once. Thus, analyzing gene expression levels via qPCR in combination with additional studies, like microarray and sequencing, may complement these findings and validate new genes and pathways responding to both early and late ^{131}I-mIBG exposures.

Although human data are the most relevant in the case of an irradiation exposure, there are confounding factors within this study that may alter the gene expression results as compared to the normal population. First, all the individuals within this study have been diagnosed with relapsed or refractory neuroblastoma and may have been previously exposed to chemotherapeutic agents and/or surgery. In addition, these data encompass exposure conditions from children treated with

potassium iodide to block and protect the thyroid, as well as concomitant chemotherapy or radiation sensitizers, which may or may not contribute at some level to the differential expression observed in the peripheral blood. Furthermore, similar studies in adults are limited due to the nature of this disease. It is also worth noting that this study encompasses 81 different patient sets amongst 59 different people, since many patients had two courses of treatment. The impact of the autologous stem cell boost may have been the reason for seeing transcriptional responses resetting prior to the next round of treatment.

In the case of a large-scale irradiation incident, estimating the dose for exposed individuals will help triage those that need immediate attention to relay the proper medical treatment. It is known that the timing since exposure can have drastic influence on dose estimate and clinical patient care (*5, 39*). Therefore, expanding the gene panel of interest out to different time points remains a key variable in providing accurate and reliable dose-estimation and clinical assistance in the event of an exposure disaster. In summary, we have shown in a human peripheral blood model system that there are unique transcripts that are differentially expressed at both early and late time points after ^{131}I-mIBG treatment. We have also identified key biomarkers responding to internal ^{131}I-mIBG at both early (72 hour) and late (15-day) time points. In addition, *FDXR*, *DDB2*, *BCL2*, and *SESN1* maintained consistent differential expression at both 72 hours and 15 days, indicating biomarkers that may remain useful in a triage incident 15 days post exposure.

Furthermore, the modulation in gene expression at the 15-day time point can still discriminate between exposed and non-exposed individuals using a selected gene transcript panel associated with DNA damage signaling, apoptosis, cell cycle progression, and cellular stress response pathways. We can also predict exposed from the non-exposed at 15 days post treatment with 87.5% or 94% specificity using the weightings from our top priority transcripts or our full transcript panel,

respectively. It is worth noting that these data not only serve to model ^{131}I dosimetry or internal exposure, but may ultimately be shown to provide a measure of patient toxicity or tolerance in the treatment of high-risk neuroblastoma patients (*27*). In the future, it will be of interest to investigate additional genome scale data such as arrays and next generation sequencing to expand our biodosimetry panel of interest and identify both patient-specific and treatment-specific responses to ^{131}I-mIBG exposure, including its relevance as a measure of overall patient outcome.

2.6 Acknowledgements

Support for this research was provided by the NIH/NCI (R01CA172067) and Columbia University NIH/NIAID Pilot Grant U19 AI067773. The UC Davis Comprehensive Cancer Center Genomics Shared Resource is supported by Cancer Center Support Grant P30CA093373 from the NCI. Work was also performed under the auspices of the U.S. Department of Energy by Lawrence Livermore National Laboratory under contract DE-AC52-07NA27344. Funding was also supported by LLNL LDRD 18-ERD-045. This work was also supported by the Translational Research Institute for Space Health through Cooperative Agreement NNX16AO69A.

Chapter 2 References:

1. Levinson HS, Garber EB. Release of inorganic phosphate from irradiated yeast: radiation biodosimetry and evaluation of radioprotective compounds. Appl Microbiol. 1967;15(2):431-40.
2. Sproull M, Camphausen K. State-of-the-Art Advances in Radiation Biodosimetry for Mass Casualty Events Involving Radiation Exposure. Radiat Res. 2016;186(5):423-35.
3. Dainiak N, Waselenko JK, Armitage JO, MacVittie TJ, Farese AM. The hematologist and radiation casualties. Hematology Am Soc Hematol Educ Program. 2003:473-96.
4. Sholom S, Dewitt R, Simon SL, Bouville A, McKeever SW. Emergency Dose Estimation Using Optically Stimulated Luminescence from Human Tooth Enamel. Radiat Meas. 2011;46(9):778-82.
5. Swartz HM, Williams BB, Flood AB. Overview of the principles and practice of biodosimetry. Radiat Environ Biophys. 2014;53(2):221-32.
6. Trompier F, Burbidge C, Bassinet C, Baumann M, Bortolin E, De Angelis C, et al. Overview of physical dosimetry methods for triage application integrated in the new European network RENEB. Int J Radiat Biol. 2017;93(1):65-74.

7. Amundson SA, Bittner M, Chen Y, Trent J, Meltzer P, Fornace AJ, Jr. Fluorescent cDNA microarray hybridization reveals complexity and heterogeneity of cellular genotoxic stress responses. Oncogene. 1999;18(24):3666-72.
8. Budworth H, Snijders AM, Marchetti F, Mannion B, Bhatnagar S, Kwoh E, et al. DNA repair and cell cycle biomarkers of radiation exposure and inflammation stress in human blood. PLoS One. 2012;7(11):e48619.
9. Kim D, Marchetti F, Chen Z, Zaric S, Wilson RJ, Hall DA, et al. Nanosensor dosimetry of mouse blood proteins after exposure to ionizing radiation. Sci Rep. 2013;3:2234.
10. Tucker JD, Joiner MC, Thomas RA, Grever WE, Bakhmutsky MV, Chinkhota CN, et al. Accurate gene expression-based biodosimetry using a minimal set of human gene transcripts. Int J Radiat Oncol Biol Phys. 2014;88(4):933-9.
11. Sproull MT, Camphausen KA, Koblentz GD. Biodosimetry: A Future Tool for Medical Management of Radiological Emergencies. Health Secur. 2017;15(6):599-610.
12. Ghandhi SA, Smilenov LB, Elliston CD, Chowdhury M, Amundson SA. Radiation dose-rate effects on gene expression for human biodosimetry. BMC Med Genomics. 2015;8:22.
13. Langen B, Rudqvist N, Parris TZ, Schuler E, Helou K, Forssell-Aronsson E. Comparative analysis of transcriptional gene regulation indicates similar physiologic response in mouse tissues at low absorbed doses from intravenously administered 211At. J Nucl Med. 2013;54(6):990-8.
14. Paul S, Amundson SA. Development of gene expression signatures for practical radiation biodosimetry. Int J Radiat Oncol Biol Phys. 2008;71(4):1236-44.
15. Schuler E, Parris TZ, Rudqvist N, Helou K, Forssell-Aronsson E. Effects of internal low-dose irradiation from 131I on gene expression in normal tissues in Balb/c mice. EJNMMI Res. 2011;1(1):29.
16. Schuler E, Rudqvist N, Parris TZ, Langen B, Spetz J, Helou K, et al. Time- and dose rate-related effects of internal (177)Lu exposure on gene expression in mouse kidney tissue. Nucl Med Biol. 2014;41(10):825-32.
17. Park WY, Hwang CI, Im CN, Kang MJ, Woo JH, Kim JH, et al. Identification of radiation-specific responses from gene expression profile. Oncogene. 2002;21(55):8521-8.
18. Paul S, Ghandhi SA, Weber W, Doyle-Eisele M, Melo D, Guilmette R, et al. Gene expression response of mice after a single dose of 137CS as an internal emitter. Radiat Res. 2014;182(4):380-9.
19. Abend M, Pfeiffer RM, Ruf C, Hatch M, Bogdanova TI, Tronko MD, et al. Iodine-131 dose dependent gene expression in thyroid cancers and corresponding normal tissues following the Chernobyl accident. PLoS One. 2012;7(7):e39103.
20. Maenhaut C, Detours V, Dom G, Handkiewicz-Junak D, Oczko-Wojciechowska M, Jarzab B. Gene expression profiles for radiation-induced thyroid cancer. Clin Oncol (R Coll Radiol). 2011;23(4):282-8.
21. Ory C, Ugolin N, Schlumberger M, Hofman P, Chevillard S. Discriminating gene expression signature of radiation-induced thyroid tumors after either external exposure or internal contamination. Genes (Basel). 2011;3(1):19-34.
22. Abend M, Badie C, Quintens R, Kriehuber R, Manning G, Macaeva E, et al. Examining Radiation-Induced In Vivo and In Vitro Gene Expression Changes of the Peripheral Blood in Different Laboratories for Biodosimetry Purposes: First RENEB Gene Expression Study. Radiat Res. 2016;185(2):109-23.

23. Visweswaran S, Joseph S, Dhanasekaran J, Paneerselvam S, Annalakshmi O, Jose MT, et al. Exposure of patients to low doses of X-radiation during neuro-interventional imaging and procedures: Dose estimation and analysis of gamma-H2AX foci and gene expression in blood lymphocytes. Mutat Res. 2020;856-857:503237.
24. Visweswaran S, Joseph S, S VH, O A, Jose MT, Perumal V. DNA damage and gene expression changes in patients exposed to low-dose X-radiation during neuro-interventional radiology procedures. Mutat Res. 2019;844:54-61.
25. DuBois SG, Matthay KK. 131I-Metaiodobenzylguanidine therapy in children with advanced neuroblastoma. Q J Nucl Med Mol Imaging. 2013;57(1):53-65.
26. Sharp SE, Trout AT, Weiss BD, Gelfand MJ. MIBG in Neuroblastoma Diagnostic Imaging and Therapy. Radiographics. 2016;36(1):258-78.
27. Campbell K, Karski EE, Olow A, Edmondson DA, Kohlgruber AC, Coleman M, et al. Peripheral Blood Biomarkers Associated With Toxicity and Treatment Characteristics After (131)I- Metaiodobenzylguanidine Therapy in Patients With Neuroblastoma. Int J Radiat Oncol Biol Phys. 2017;99(2):468-75.
28. Edmondson DA, Karski EE, Kohlgruber A, Koneru H, Matthay KK, Allen S, et al. Transcript Analysis for Internal Biodosimetry Using Peripheral Blood from Neuroblastoma Patients Treated with (131)I-mIBG, a Targeted Radionuclide. Radiat Res. 2016;186(3):235-44.
29. DuBois SG, Chesler L, Groshen S, Hawkins R, Goodarzian F, Shimada H, et al. Phase I study of vincristine, irinotecan, and (1)(3)(1)I-metaiodobenzylguanidine for patients with relapsed or refractory neuroblastoma: a new approaches to neuroblastoma therapy trial. Clin Cancer Res. 2012;18(9):2679-86.
30. Amundson SA, Grace MB, McLeland CB, Epperly MW, Yeager A, Zhan Q, et al. Human in vivo radiation-induced biomarkers: gene expression changes in radiotherapy patients. Cancer Res. 2004;64(18):6368-71.
31. Amundson SA, Myers TG, Fornace AJ, Jr. Roles for p53 in growth arrest and apoptosis: putting on the brakes after genotoxic stress. Oncogene. 1998;17(25):3287-99.
32. Paul S, Smilenov LB, Amundson SA. Widespread decreased expression of immune function genes in human peripheral blood following radiation exposure. Radiat Res. 2013;180(6):575-83.
33. Wyrobek AJ, Manohar CF, Krishnan VV, Nelson DO, Furtado MR, Bhattacharya MS, et al. Low dose radiation response curves, networks and pathways in human lymphoblastoid cells exposed from 1 to 10cGy of acute gamma radiation. Mutat Res. 2011;722(2):119-30.
34. Rohart F, Gautier B, Singh A, Le Cao KA. mixOmics: An R package for 'omics feature selection and multiple data integration. PLoS Comput Biol. 2017;13(11):e1005752.
35. Lacombe J, Sima C, Amundson SA, Zenhausern F. Candidate gene biodosimetry markers of exposure to external ionizing radiation in human blood: A systematic review. PLoS One. 2018;13(6):e0198851.
36. O'Brien G, Cruz-Garcia L, Majewski M, Grepl J, Abend M, Port M, et al. FDXR is a biomarker of radiation exposure in vivo. Sci Rep-Uk. 2018;8.
37. Brzoska K, Kruszewski M. Toward the development of transcriptional biodosimetry for the identification of irradiated individuals and assessment of absorbed radiation dose. Radiat Environ Bioph. 2015;54(3):353-63.
38. Carlin S, Mairs RJ, McCluskey AG, Tweddle DA, Sprigg A, Estlin C, et al. Development of a real-time polymerase chain reaction assay for prediction of the uptake of meta-[(131)I]iodobenzylguanidine by neuroblastoma tumors. Clin Cancer Res. 2003;9(9):3338-44.

39. Ainsbury EA, Bakhanova E, Barquinero JF, Brai M, Chumak V, Correcher V, et al. Review of Retrospective Dosimetry Techniques for External Ionising Radiation Exposures. Radiat Prot Dosim. 2011;147(4):573-92.

Chapter 2 Appendix

Subject: Re: [External] Attention: Permissions Coordinator
Date: Monday, February 14, 2022 at 1:40:42 PM Pacific Standard Time
From: Fye, Judy
To: Angela Clare Evans
CC: coleman16@llnl.gov
Attachments: image001.png, image002.png

Dear Angela,

Congratulations on the completion of your Ph.D., we send our good wishes for your future.

Radiation Research grants to Requester the permission to re-publish article: "Peripheral Blood Transcript Signatures after Internal 131I-mIBG Therapy in Relapsed and Refractory Neuroblastoma Patients Identifies Early and Late Biomarkers of Internal 131I Exposures." Radiat Res 2022; 197:101-112, as a part of your dissertation.

The above-mentioned article is not an Open Access article, therefore, *Radiation Rese*arch retains copyright and does not grant irrevocable, nonexclusive license to University of California, Davis, we also do not agree to allow the independent article to be place any open access repository or depository.

If you would like to purchase Open Access for the above-mentioned article, please let us know.

All the best,
Judy

Judy E. Fye
Managing Editor, *Radiation Research*

E-mail address: jfye@iu.edu
Editorial office phone: 317·944·1308

	P value (72 hrs vs Baseline)	FDR value
CDKN1A	<0.000001	<0.000001
FDXR	<0.000001	<0.000001
GADD45A	0.000344	0.000232
XPC	0.000002	0.000001
BCLXL/BCL2L1	<0.000001	<0.000001
STAT5B	0.000394	0.000239
BCL2	0.020016	0.007135
BAX	<0.000001	<0.000001
DDB2	<0.000001	<0.000001
PRKDC	0.014392	0.005814
MDM2	0.011317	0.005171
SESN1	0.015751	0.005966
POLH	0.011946	0.005171
BBC3	<0.000001	<0.000001
PCNA	0.002399	0.001321
IGF1R	<0.000001	<0.000001
SGK1	0.011909	0.005171

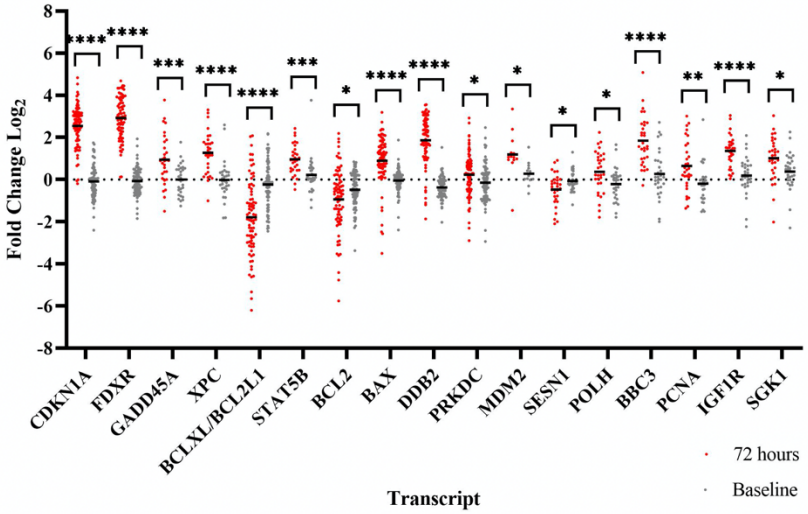

Figure A.2.1: Individual fold change plots and statistical significance across 72-hour time point. Unpaired multiple t-tests determined statistical significance amongst time points. Left panel: The p-values for 72 hours vs. Baseline were analyzed. All fold changes were log_2 transformed and compared to untreated controls. Right panel: Quantitative real-time PCR determined fold change fluctuations between 72 hours vs. Baseline. Each dot represents one blood sample. All fold changes are with respect to untreated blood draw A (Baseline A). The black line represents the mean fold change.

	P value (15 days vs Baseline)	FDR value
CDKN1A	0.441898	0.372254
FDXR	0.011147	0.013760
GADD45A	0.880141	0.586203
XPC	0.028870	0.031669
BCLXL/BCL2L1	0.896980	0.586203
STAT5B	0.007300	0.011586
BCL2	0.002583	0.004783
BAX	0.812857	0.586203
DDB2	0.031355	0.031669
PRKDC	0.001428	0.003967
MDM2	0.002145	0.004767
SESN1	0.000287	0.002762
POLH	0.000746	0.002762
BBC3	0.232644	0.215389
PCNA	0.469087	0.372254
IGF1R	0.000500	0.002762
SGK1	0.009254	0.012851

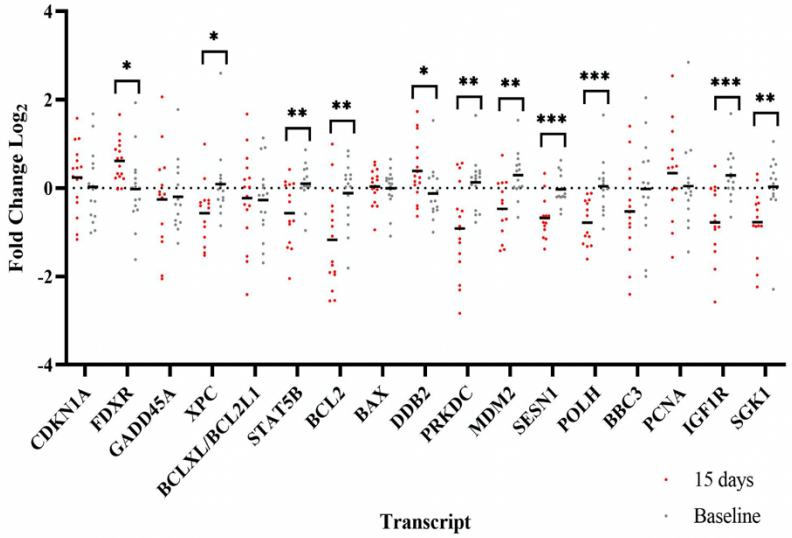

Figure A.2.2: Individual fold change plots and statistical significance across 15-day time point. Unpaired multiple t-tests determined statistical significance amongst time points. Left panel: The p-values for 15 days vs.

Baseline. All fold changes were log_2 transformed and compared to untreated controls. Right panel: Quantitative real-time PCR determined fold change fluctuations between 15 days vs. Baseline. Each dot represents one blood sample. All fold changes are with respect to untreated blood draw A (Baseline A). The black line represents the mean fold change.

	P value (72 hrs vs 15 days)	FDR value
CDKN1A	<0.000001	<0.000001
FDXR	<0.000001	<0.000001
GADD45A	0.003265	0.000707
XPC	<0.000001	<0.000001
BCLXL/BCL2L1	0.000031	0.000009
STAT5B	<0.000001	<0.000001
BCL2	0.462943	0.082513
BAX	0.000002	<0.000001
DDB2	<0.000001	<0.000001
PRKDC	0.000572	0.000133
MDM2	0.000111	0.000028
SESN1	0.260418	0.052604
POLH	0.000007	0.000002
BBC3	<0.000001	<0.000001
PCNA	0.400666	0.075876
IGF1R	<0.000001	<0.000001
SGK1	<0.000001	<0.000001

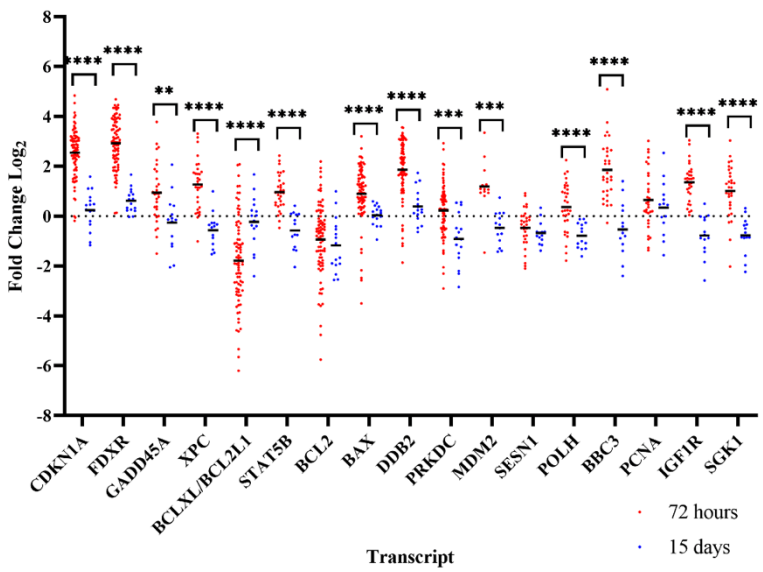

Figure A.2.3: Individual fold change plots and statistical significance across 72-hours and 15-day time points. Unpaired multiple t-tests determined statistical significance amongst time points. Left panel: The p-values for 72 hours vs. 15 days were analyzed. All fold changes were log_2 transformed and compared to untreated controls. For the 72 hours vs 15-day comparison, a multiple t-test with Welch's correction (assumed variance between each group) was applied since there were drastically different numbers of patients tested at 72 hours versus 15 days. Right panel: Quantitative real-time PCR determined fold change fluctuations between 72 hours vs. 15 days. Each dot represents one blood sample. All fold changes are with respect to untreated blood draw A (Baseline A). The black line represents the mean fold change.

Chapter 3: Curcumin nanodiscs improve solubility and protect against ionizing radiation exposures

Authors:

Angela C. Evans[1,2], Kelly A. Martin[2], Manoj Saxena[1], Sandra Bicher[3,4], Elizabeth Wheeler[5], Christopher D. Porada[6], Graça Almeida-Porada[6], Takamitsu Kato[7], Paul F. Wilson[1], and Matthew A. Coleman[1,2]

1. Department of Radiation Oncology, University of California Davis, Sacramento, CA, USA
2. Physical and Life Sciences Directorate, Lawrence Livermore National Laboratory, Livermore, CA, USA
3. Institute of Radiation Medicine, Helmholtz Zentrum München, Munich, Germany
4. Department of Radiation Oncology, Klinikum rechts der Isar, Technical University Munich (TUM), Munich, Germany
5. Engineering Directorate, Lawrence Livermore National Laboratory, Livermore, CA., USA
6. Wake Forest Institute for Regenerative Medicine, Wake Forest University School of Medicine, Winston-Salem, NC, USA
7. Department of Environmental & Radiological Health Sciences, Colorado State University, Fort Collins, CO, USA

3.1 Abstract

Curcumin, a natural polyphenol present within the spice turmeric (*Curcuma longa*), contains antioxidant, anti-inflammatory, and anti-cancer properties and has also presented as a promising radiation medical countermeasure (MCM). However, curcumin bioavailability is inherently low due to poor water solubility and rapid metabolism. Here, we have successfully incorporated

curcumin into “biomimetic” nanolipoprotein particles (cNLPs) surrounded by apolipoprotein A1 and amphipathic polymer scaffolding moieties. Our cNLP formulation improves the water solubility of curcumin and produces nanoparticles with ~350 μg/ml total soluble curcumin for downstream *in vitro* applications. We found that cNLPs were well-tolerated in human primary lung fibroblasts (AG05965/MRC-5 cells) in G0/G1-phase compared to those treated with curcumin solubilized in DMSO (curDMSO). Pre-treatment with cNLPs on MRC-5 cultures also improved cell survival when exposed to ^{137}Cs rays. These findings may be useful for establishing curcumin nanodiscs as a method to improve the bioavailability of curcumin for administration as radioprotective agents against ionizing radiation (IR) exposures.

3.2 Introduction

Curcumin, a major component of turmeric (*Curcuma longa*), is a naturally occurring phytochemical known for its pleotropic health benefits including antioxidant and anti-inflammatory properties (1). Turmeric, a common household spice and the main source of curcumin, has been used in South-East Asia and the Middle East for centuries as a curative for minor ailments, as well as a food additive, dye colorant, and cosmetic additive globally (2). Recently, curcumin has been studied as a health supplement for a variety of diseases and disorders, including liver fibrosis, diabetes, cardiovascular disease, and cancer (3). To date, there have been over 100 clinical trials involving more than 6,000 participants examining the safety, efficacy, and health benefits of curcumin against numerous disease states (4). It has been established that curcumin is safe and well-tolerated in humans, with acceptable intake up to 12 grams/day demonstrating little to no toxicity (5).

Currently, the mechanisms of action following curcumin treatment are being investigated with increasing popularity in humans (1, 3, 4). It is well-accepted that curcumin modulates a wide variety of cellular pathways that can affect a multitude of downstream functions, including cancer cell proliferation, apoptosis, cell cycle arrest, and inflammatory processes (3, 4). For example, curcumin has been shown to increase cell cycle arrest and disrupt VEGF, EGFR, and COX-2 pathways in numerous cancer cell lines (3). Curcumin is also a potent anti-inflammatory and free-radical scavenger, and it has been proposed that curcumin alters arachidonic acid metabolism, potentially as an upstream regulator of inflammatory processes via cyclooxygenase (COX), lipoxygenase (LOX), and tumor necrosis factor (TNF) inhibition (6). Curcumin has also been shown to decrease reactive oxygen species (ROS) production via decreasing inducible nitric oxide synthase (iNOS), increasing glutathione peroxidase, as well as increasing the transcription of antioxidant gene response elements through the Nrf-2-Keap1 complex (6).

Ionizing radiation exposures increase ROS production which can lead to increased DNA damage in cells as well as dysregulated downstream biological pathways. Previous studies have demonstrated that natural antioxidants, such as curcumin, may offer potential as radiation protectants or radiation countermeasures (7). Recently, curcumin has shown to protect human lymphocytes from lipid peroxidation and improved antioxidant potential following up to 4 Gy gamma exposures (8). Curcumin treatments have also improved wound healing response times following mice exposed to whole body doses up to 20 Gy (9), and oral administration of curcumin in mice shows decreased micronucleated polychromatic erythrocytes following 1.15 Gy of total body gamma irradiation (10). However, unlike this study, these findings were not focused on the effects on DNA double strand break (DSB) repair or cell survival following curcumin treatment.

Although curcumin acts as a promising phytochemical for radiological protection or as a radiation MCM, it has an inherently low water-solubility and poor bioavailability due to its limited absorption, rapid metabolism, and fast excretion (11). Several formulations have been proposed to circumvent the problem of low curcumin bioavailability, including curcumin-adjuvant formulations, nanoparticles, or liposomes (11). Co-administration of piperine with curcumin in mice shows an enhanced protective effect against stress-induced neural impairment over curcumin treatment alone (12). Furthermore, concomitant administration of piperine with curcumin demonstrates increased absorption of curcumin in both rats and humans, with a 2000% increase in bioavailability in human subjects (13). In addition, curcumin liposomal formulations have also recently shown promise to enhance curcumin bioavailability *in vitro* and *in vivo*, as shown via increased apoptosis and toxicity to colon, lung, prostate, and cervical cancer cell lines as well as decreased tumor growth in mouse xenograft models (14, 15). Previous nanocurcumin formulations also improved curcumin water solubility and were well-tolerated *in vivo* (16). In this study, we describe the formulation and characterization of curcumin nanolipoprotein particles (NLPs) as a vehicle to increase curcumin bioavailability.

NLPs are nanodiscs composed of lipids and scaffolding proteins that mimic high-density lipoprotein (HDL) particles within the human body. They can be readily customizable to a variety of lipids, scaffolding proteins, as well as polymeric or adjuvant formulations and are virtually non-toxic *in vitro* and *in vivo* (17). In addition, NLPs also act as biomimetic transporters of cargo into the cell (17), and serve as biodelivery platforms for otherwise unstable or insoluble moieties, including self-amplifying mRNA replicon (18) or membrane proteins (19, 20). It has previously been shown that curcumin incorporation into stable nanodiscs surrounded by either apolipoprotein ApoA1 or ApoE increases the efficiency of curcumin delivery and subsequent apoptosis in

hepatoma, lymphoma, and glioblastoma cell lines (21-23). However, these studies did not examine the effects of curcumin nanodiscs on normal human cells or its impact on cells pre- or post-IR exposure. Here, we introduce the production of our curcumin-loaded ApoA1 NLPs (cNLPs) by mixing curcumin with DMPC lipid and amphipathic telodendrimer polymers, followed by the addition of ApoA1 scaffolding proteins, and then characterize curcumin bioavailability *in vitro* as a potentially less toxic alternative to DMSO solubilized curcumin. We also examine the protection that our cNLP formulations may provide against IR-induced DNA damage and subsequent cell survival following ionizing radiation exposures *in vitro*.

The current study examines the compatibility of cNLPs compared to DMSO solubilized curcumin in a cell line derived from normal human fetal lung tissue (AG05965/MRC-5) primary lung fibroblasts and tests the ability of cNLPs to alter DNA DSB kinetics and cell survival following exposure to ^{137}Cs gamma rays. The goal of this study was to demonstrate the production, characterization, and toxicity of our cNLPs and to test whether these cNLPs may serve as radiological protectants in normal human fibroblasts. To our knowledge, this is the first study examining the effects of solubilized curcumin nanodiscs on overall toxicity and radiation protection in normal human fibroblasts. We demonstrate that our cNLPs solubilize curcumin in the lipidic nano-environment as evidenced via an absorbance shift, size exclusion chromatography (SEC), and dynamic light scattering (DLS). In addition, we show that our cNLPs protect against IR-induced cellular death *in vitro* and demonstrate the utility of cNLP formulations as potential radiation protectants or radiation medical countermeasures (MCM). These data suggest that cNLPs may be useful MCM in the clinic for patients undergoing radiotherapy or following ubiquitous environmental exposures to radiation throughout deep space missions.

3.3 Materials and Methods

Formulating curcumin-telodiscs (cur-telodiscs)

The first step to cNLP formation was forming the curcumin telodendrimer-lipid discs (cur-telodiscs). To formulate the cur-telodiscs, 60 mg/ml curcumin (in DMSO), 20 mg/ml of 1,2-dimyristoyl-sn-glycero-3-phosphocholine (DMPC) lipid (Avanti Polar Lipids) (in water), and 20 mg/ml telodendrimer PEG5k-CA8 polymer (in water) are prepped as stock solutions. First, re-constituted DMPC lipid [20 mg/ml] was sonicated in a horn sonicator for about 25-45 minutes or until optical translucence is achieved. The lipid was then mixed with the telodendrimer [20 mg/ml] in a 10:1 vol/vol (DMPC: telodendrimer) ratio. Solubilized curcumin [60 mg/ml in DMSO] was then added to the lipid-telodendrimer mixture at a 9:10:1 vol/vol/vol ratio (curcumin: DMPC: telodendrimer). The final concentration of the curcumin telodendrimer-lipid mixture (cur-telodisc) is 27 mg/ml curcumin, 10 mg/ml DMPC, and 1 mg/ml telodendrimer. The resulting cur-telodiscs were then sonicated for 30-45 minutes until homogenized in a horn sonicator and spun down in a microcentrifuge at 10,000 rpm for 1 minute to remove any unincorporated curcumin.

Formulating curcumin nanolipoprotein particles (cNLPs)

To formulate the cNLPs, 500 µl of soluble cur-telodisc was combined with purified Δ49ApolipoproteinA1 (ApoA1) (final ApoA1 concentration of 2 mg/ml) and 1X PBS to a final volume of 1 ml. The resulting curcumin nanoparticles were then sonicated for 30 minutes in a bath sonicator and then dialyzed overnight against 1X PBS pH 7.4 at room temperature. After dialysis, 250 µl of freshly sonicated [20 mg/ml] DMPC lipid is added per ml of dialyzed curcumin mixture, re-sonicated for 45 more minutes in a bath sonicator, and then centrifuged at 10,000 rpm for 1

minute to remove any potential unincorporated curcumin. The resulting supernatant contains soluble curcumin nanolipoprotein particles, or cNLPs.

UV-Vis Spectroscopy

UV-Vis spectroscopy was utilized to determine total curcumin incorporated into the cNLPs based on previous studies with ApoA1 and E4 nanodiscs as well as curcumin-amyloid aggregates (21-23). Curcumin absorbance at 430 nm was read using the NanoDropTM One^{C} spectrophotometer (Thermo Fisher Scientific). To establish a standard curve, absorbance readings at 430 nm were read for two-fold serial dilutions of curcumin solubilized in DMSO at [0.25 mg/ml], [0.125 mg/ml], [0.06 mg/ml], [0.03 mg/ml], and [0.015 mg/ml]. The resulting standard curve equation was calculated using Microsoft Excel along with the resulting R^2 value. For our experiments, our R^2 value was consistently $\geq$0.99. A new standard curve was created with fresh curcumin solubilized in DMSO for comparison to each new cNLP prep. Absorbance readings of cNLP at 430 nm were then compared to the standard curve to give a final concentration of curcumin in our cNLP sample.

Size Exclusion Chromatography (SEC)

Size exclusion chromatography was used to demonstrate proper incorporation of curcumin within our cNLP particles. cNLPs were diluted ~1:50 in PBS and loaded into a SEC column (Superose 6 Increase, GE Healthcare) to verify curcumin incorporation. SEC was run at a flow rate of 0.6 ml/min in PBS buffer. Curcumin absorbance (430 nm) along with protein absorbance (280 nm) was used to demonstrate curcumin incorporation into the cNLPs. Total run time per sample did not exceed 6 minutes.

Dynamic Light Scattering (DLS)

Dynamic light scattering was applied to determine the solution size of the nanoparticles with and without loaded curcumin. Here, 1 µL of sample was diluted in 99 µL 1X PBS in a cuvette. The cuvette was then placed into the DLS (Zetasizer Nano ZSP, Malvern Panalytical, Westborough, MA, USA) and the average size or aggregation state of the particles was determined. Zetasizer Nano ZSP software was used for analysis of the particle size distribution.

UV Transluminescence

Fluorescence of free curcumin dissolved in water or DMSO was compared alongside curcumin in telodisc form (Lipids). Curcumin concentrations in water, DMSO, or lipids ranged from 0.015-0.5 mg/ml total curcumin incorporation. 100 µl of each solution was aliquoted and imaged for general fluorescence under a UV lamp (365 nm).

Cell culture

AG05965/MRC-5 normal primary human lung fibroblasts were maintained in MEMα with 1X GlutaMAX media (GIBCO/Invitrogen). Media was supplemented with 15% FBS, 0.8% PenStrep (GIBCO/Invitrogen), 0.8% MEM Vitamins (GIBCO/Invitrogen), 0.8% MEM (Essential) Amino Acids Solution (GIBCO/Invitrogen), 0.8% MEM Non-Essential Amino Acids Solution (GIBCO/Invitrogen), and 4 mM NaOH. Cell culture media was filtered through a 0.2-micron PES filter before use. Cells were cultured in a 37°C incubator with 5% CO_2. Experiments were conducted with cells below 20 passages.

Cell Proliferation (MTS) Assay

AG05965/MRC-5 normal primary human lung fibroblasts were seeded at 10,000 cells/well in a 96 well plate. After ~24-48 hours of growth, the cells were washed 1X with PBS then treated with cNLPs [0, 20, 40, 60, 80, or 100 μM curcumin], curDMSO [0, 20, 40, 60, 80, or 100 μM curcumin], or empty NLPs [added the same volumes as cNLP group] for 18 hours. The maximum amount of DMSO used in the 100 μM curDMSO group was 0.4%. Following 18-hour curDMSO/cNLP/empty NLP treatment, 20 ul CellTiter 96® AQueous One Solution Reagent (Promega) was added to each well containing the samples in 100 μl culture medium. Cells were then incubated in a 37°C incubator with 5% CO_2 for 4 hours. After 4 hours, absorbance was read at 490 nm using a 96-well plate reader and 650 nm (background) was subtracted from all wells prior to normalization. Normalized values were calculated by dividing the average 490 nm absorbances of empty NLP, cNLP, or curDMSO treated wells by the average 490 nm absorbances from cells treated only with cell culture media ($Absorbance_{490}$ treated cells/$Absorbance_{490}$ media alone cells). Two independent biological replicates were combined to determine statistical significance using Two-Way ANOVA.

DNA Damage Immunohistochemistry

G0/G1 AG05965/MRC-5 normal primary lung fibroblasts were grown to confluency in standard MRC-5 culture media on Nunc-flaskettes (Thermo Fisher). Once confluent, cells were treated for 18 hours with 10 μg/ml [27μM] cNLPs, 10 μg/ml [27μM] curDMSO, or 0.1% DMSO alone prior to 50 cGy or 0 cGy (SHAM) irradiation. Cells were then irradiated with 50 cGy of ^{137}Cs gamma rays or 0 cGy (SHAM) at Lawrence Livermore National Laboratory (LLNL). Flaskettes were returned to the cell incubator for deactivation and samples were fixed at 15, 120,

360 and 1440 min following IR by aspirating medium, rinsing gently 2X with DPBS (with $Ca^{2+/}Mg^{2+}$), and fixed for 15 min with 4% Paraformaldehyde (PFA) in 1X PBS. Following fixation, PFA was aspirated and flaskettes were rinsed (3x5 min) with DPBS on rocker and then filled with DPBS, capped, and resealed with Parafilm and stored in 4°C refrigerator until immunostaining.

Within a few weeks post fixation, cells were immunostained as previously described (24). In detail, chambers were rinsed 2X with room temperature (RT) DPBS for 5 minutes each on rocker. Cells were then permeabilized with ice-cold PBS with 0.5% Triton X-100 per chamber and placed on rocker on ice tray for 10 minutes. Permeabilization solution was then aspirated and flaskettes were rinsed 2X with RT DPBS for 5 minutes each on rocker. Samples were then treated with Image-iT™ FX Signal Enhancer solution (Thermo Fisher) and incubated at room temperature for 30 minutes. Image-iT™ FX Signal Enhancer solution was then aspirated, and chambers were rinsed 2X with RT DPBS for 5 minutes each on rocker. Samples were then blocked with 2% goat serum, 2% FBS, 1% BSA, 0.1% Triton X-100, and 0.05% Tween-20 in PBS at RT for 30–60 minutes on the rocker. After blocking, cells were rinsed quickly RT DPBS and chambers and gasket were carefully removed from the slide with a razor blade. Primary antibody solutions of 1:250 Upstate mouse anti-phosphoH2AX JBW301 (Millipore # 05-636) and 1:250 rabbit anti-53BP1 (Novus #NB100-304) in PBS with 1% BSA were loaded on slide. Slides were overlayed with coverslip and incubated horizontally in a 37°C humid chamber (wet slide box/Tupperware in incubator/warm room) for 30–60 minutes. Slides were rinsed 3X in RT DPBS for 5 minutes each in dark Coplin jars on rocker. Secondary antibodies 1:500 Molecular Probes Alexa-488-conjugated goat anti-mouse IgG (Thermo Fisher #A-11017) and 1:500 Molecular Probes Alexa-594-conjugated goat anti-rabbit IgG (Thermo Fisher #A-11072) prepped in PBS alone (no BSA) were then mounted on slide with overlaying coverslip and incubated horizontally in a dark 37°C humid

chamber for 30–60 minutes. Slides were then rinsed 2X in RT DPBS for 5 minutes each in dark Coplin jars on rocker, followed by 1X final rinse for 10 minutes. Slides were then incubated in freshly prepared RT 3.7% paraformaldehyde in PBS for 10 minutes followed by (2x5min) rinses with RT DPBS on rocker. After the final rinse, excess PBS was removed from slides and slides were treated with RT Molecular Probes ProLong Gold with 0.2 µg/ml DAPI (Thermo Fisher) and overlayed with a 24 mm x 50 mm coverslip. Slides were cured overnight at RT in a light-tight slide box and then transferred to the refrigerator the following day and stored at 4°C until imaging. Slides were imaged at 63x with a Carl Zeiss microscope using Zen Software. Over 250 cells were counted per experimental time point.

Survival Curves

To assess the radioprotectant capabilities of cNLPs, G0/G1 AG05965/MRC-5 normal primary lung fibroblasts were treated for 18 hours with 10 µg/ml [27µM] cNLPs, 10 µg/ml [27µM] curDMSO, 10 µg/ml empty NLPs, or 0.1% DMSO alone prior to 50 cGy ^{137}Cs or 0 cGy (SHAM) irradiation. After 18 hours of treatment, cells were trypsinized and counted via Countess II FL (Invitrogen) and aliquoted into respective tubes for irradiation. Approximately 100, 111, 143, 222, 500, and 3333 cells/ml media were aliquoted into respective tubes for subsequent 0 Gy (SHAM), 0.5 Gy, 1 Gy, 2 Gy, 4 Gy, and 6 Gy irradiations, respectively. Cells were then irradiated with ^{137}Cs gamma rays at Lawrence Livermore National Laboratory (LLNL). After irradiation, cells were plated in triplicate T-25 flasks (4 ml/flask) and placed in 37°C incubator with 5% CO_2 and left undisturbed for 7 days. After 1 week, cell medium was replaced in all flasks. After 1 more week (14 days following IR), cells were fixed by aspirating medium, rinsed gently twice with 1X DPBS, and fixed/stained with 3-4 ml of staining solution (50% v/v Kopykake blue dye, 40% v/v 95%

EtOH, and 10% v/v glacial acetic acid). Flasks were stained on a shaker for 30-60 mins. Flasks were then rinsed gently twice with ultradistilled Milli-Q water, excess water was removed, and flasks were stood up neck-down on absorbent towels to drain out fully and dry overnight. Colonies with ≥25 cells were scored as survivors using a standard light microscope.

Statistical Analysis

A p-value of 0.05 was used as a cutoff to determine statistical significance. P-values are labeled as <0.05 (*), <0.01 (**), <0.001 (***), and <0.0001 (****) throughout the manuscript. Two-Way ANOVA was applied for the MTS assay to compare cNLP vs curDMSO vs empty NLP treatment viability. One-Way ANOVA was applied amongst SHAM groups at 15 minute and 24-hour time points within each treatment group. Two-Way ANOVA was also used for calculating induced foci/cell differences amongst treatment groups and time points. For foci counts, all outliers were removed prior to graphing. Induced foci counts/cell were calculated by subtracting the averaged foci counts for the SHAM values determined for curDMSO, cNLP, or DMSO alone control groups from the raw foci counts per treatment. Statistical analysis and graphs used Graphpad Prism Version 9.1.2 software.

3.4 Results

Nanolipoprotein particles support curcumin addition

Curcumin was successfully incorporated into nanodiscs using a combination of 1,2-dimyristoyl-sn-glycero-3-phosphocholine (DMPC), amphiphilic telodendrimer polymer (25), and Δ49 apolipoprotein A1 (ApoA1) (Figure 3.1). Size exclusion chromatography (SEC) illustrates the mixture of nanodiscs surrounded by either a telodendrimer polymer or apolipoprotein dominant

cNLP product (Figure 3.2a). Curcumin nanodiscs containing curcumin, DMPC, telodendrimer, and apolipoprotein ApoA1 scaffold are all components of the larger nanoparticles and elute from the SEC column at around 2 minutes. In contrast, smaller nanodiscs were also formed and eluted with a distinct peak at about 3.6 minutes. Both nano-species demonstrate overlapping 280 nm and 430 nm absorbances, indicating co-localized curcumin within the NLP nanodiscs, respectively (Figure 3.2a). The resulting mixture of curcumin nanodiscs (mixtures of curcumin-apolipoprotein A1 and curcumin-telodendrimer-apolipoprotein A1 discs) were applied to all downstream assays and were collectively termed "cNLPs". Dynamic light scattering (DLS) estimated an average size of 43 nm for our heterogeneous cNLP formulation (standard deviation of 11 nm) with a polydispersity index of 0.232 (Figure 3.2b). Our cNLP formulations show increased solubility over curcumin solubilized in water and a similar solubility to curcumin solubilized in DMSO (curDMSO) (Figure 3.2c). Contrary to the yellow fluorescence observed under UV light for curDMSO solutions, the cNLPs demonstrate a slight blue-shift in fluorescence, indicating incorporation of the curcumin into the lipid nanodisc environment (Figure 3.2c) (26). Across three biological replicates, our cNLP formulation yielded an average of 348 µg/ml incorporated curcumin.

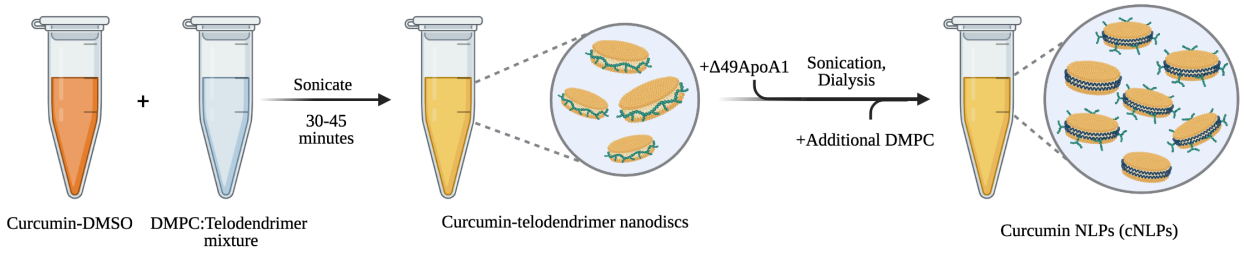

Figure 3.1: Forming curcumin nanoparticles. Curcumin-DMSO, DMPC, and an amphipathic telodendrimer (green) polymer are mixed to form curcumin-telodendrimer nanodiscs (cur-telodiscs). After cur-telodisc formation, Δ49ApoA1 protein (blue) is added to form curcumin-apolipoprotein nanodiscs. Removal of DMSO is achieved by

dialysis overnight in 1X PBS. The next morning, additional DMPC lipid is added, and the resulting mixture contains solubilized small and large nanodiscs, collectively termed cNLPs.

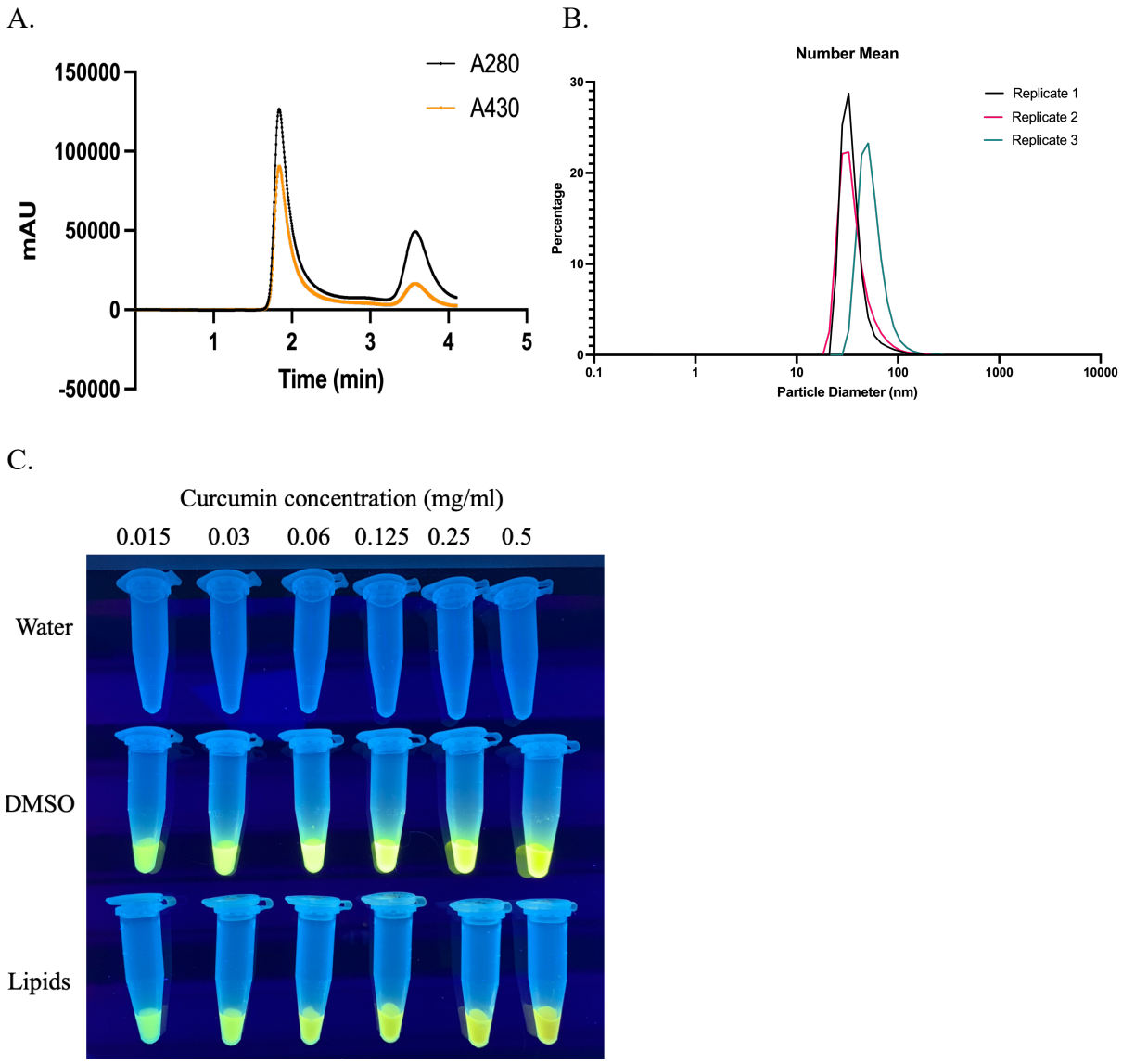

Figure 3.2: Characterization of curcumin-NLPs (cNLPs). A) Size exclusion chromatogram demonstrates that curcumin associates within larger (leftmost peak) as well as smaller (rightmost peak) ApoA1-NLPs via co-localized 280 nm protein absorbance (black) and 430 nm curcumin absorbance (orange). B) Dynamic Light Scattering of cNLPs demonstrates that these particles average about 43 nm in diameter. C) Comparison of curcumin fluorescence when solubilized in water, DMSO, or curcumin-telodendrimer nanodiscs at 0.015-0.5 mg/ml concentrations.

Normal human fibroblasts tolerate cNLPs better than DMSO solubilized curcumin

Primary human MRC-5 fibroblasts were treated with curcumin solubilized in nanodiscs (cNLPs), empty NLPs (no curcumin), or DMSO-solubilized curcumin (curDMSO). Cells treated with cNLPs trended towards increased cell viability over curDMSO treated cells at 40, 60, 80, and 100 µM concentrations. Statistical significance was achieved ($p<0.05$) between cNLP and curDMSO treated cells at 60 µM and 100 µM curcumin concentrations. At 40 µM and 80 µM curcumin concentrations, cells trended towards higher viability in cNLP groups, but these concentrations were not statistically significant from curDMSO ($p=0.1$). Cell viability was unchanged at 20 µM amongst the cNLP or curDMSO groups, but cNLPs expressed slightly higher viability over empty NLP controls (Figure 3.3).

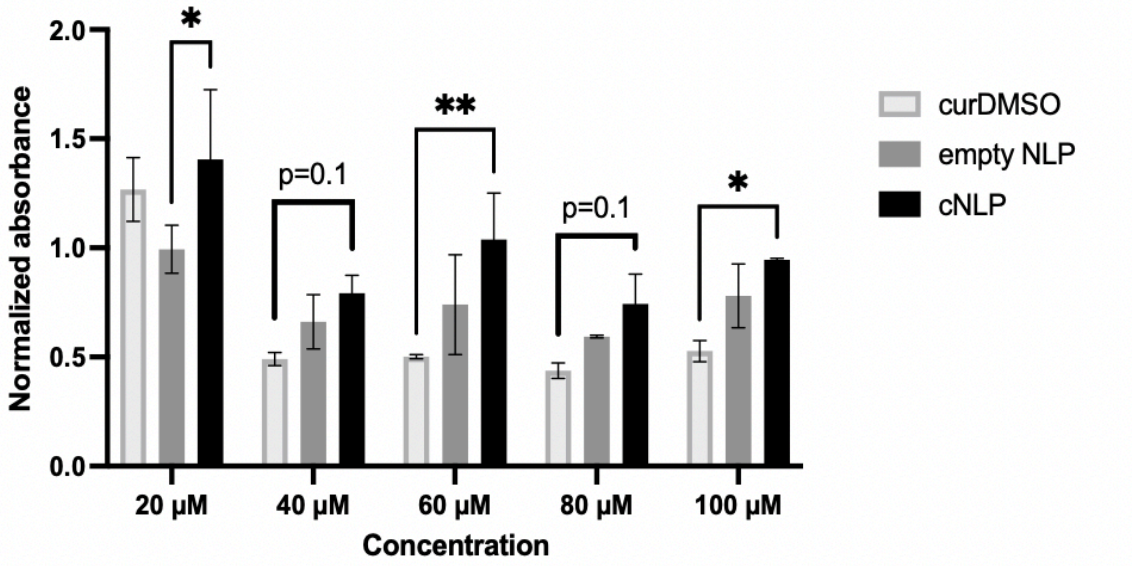

Figure 3.3: MRC-5 cells tolerate cNLP better than DMSO solubilized curcumin. MRC-5 cells were pre-treated for 18 hours with various concentrations of empty NLP (no curcumin), or with curcumin solubilized in the nanodisc (cNLP) or DMSO (curDMSO). MTS reagent was then applied to measure cell proliferative capacity. Shown is the mean normalized absorbance with standard deviation (SD). All wells were normalized to cells treated with media alone.

cNLP pre-treatment does not decrease DNA DSB foci formation but alters foci persistence following gamma irradiation

Since curcumin demonstrates natural antioxidant properties, we next sought to determine if cNLPs may alter DNA DSB foci persistence following ionizing radiation exposures. Within each treatment group, background foci/cell in SHAM samples fixed at 15 min or 24 hours were not statistically different from one another and were averaged for each treatment (cNLP, curDMSO, or DMSO alone) to determine induced foci counts (Figure 3.4).

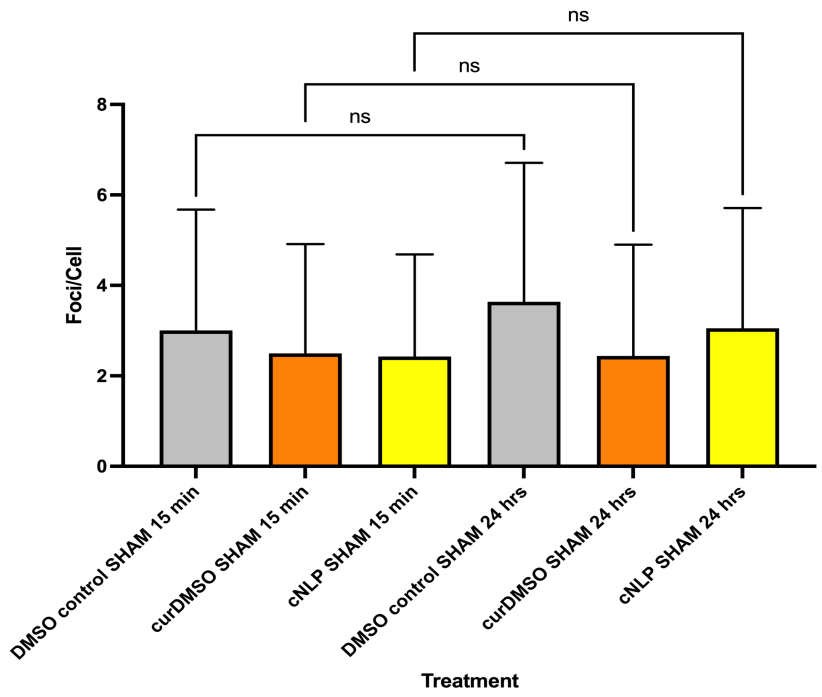

Figure 3.4: SHAM treated foci counts amongst treatment groups.

The number of induced foci/cell in cNLP, curDMSO, and DMSO treated groups exposed to 50 cGy ^{137}Cs rays were not significantly different from one another at the early time point (15 minutes) or the late time point (24 hours) post-exposure (Figure 3.5). Interestingly, cNLPs displayed slightly increased foci at the 2-hour time point when compared to DMSO controls (mean

induced foci/cell 4.84 and 3.77, respectively), however, induced cNLP foci counts were not significantly different than induced curDMSO foci counts at this time point (4.84 vs. 4.16 foci/cell, respectively). In addition, both curDMSO and cNLP groups displayed increased foci counts (mean induced foci/cell 2.2 and 2.5, respectively) compared to DMSO alone (mean induced foci/cell 0.94) at 6 hours post-exposure (Figure 3.5). Within each treatment group, the number of raw foci gradually decreased with time, overlapping with SHAM controls when fixed at the 24-hour time point (Figure 3.6). Representative immunostained images of foci following 50 cGy ^{137}Cs rays at the 15-minute fixation time point for cNLP, curDMSO, and 0.1% DMSO treatments are shown, demonstrating co-localization of gamma H2AX, 53BP1, and nuclear stain DAPI (Figure 3.7).

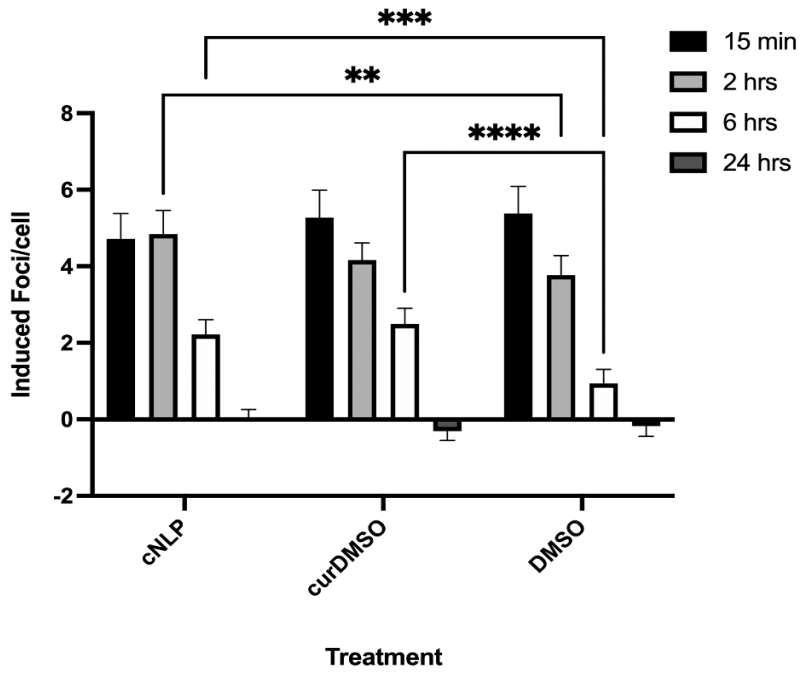

Treatment	Time post IR	15 min		2 hrs		6 hrs		24 hrs	
		Mean	SD	Mean	SD	Mean	SD	Mean	SD
	cNLP	4.72	5.77	4.84	5.32	2.22	3.38	0.003	2.39
	curDMSO	5.27	5.97	4.16	3.93	2.49	3.51	-0.309	2.06
	DMSO	5.38	6.26	3.77	4.57	0.94	3.45	-0.178	2.35

Figure 3.5: Curcumin pre-treatment alters foci persistence following ^{137}Cs exposures. MRC-5 cells were pre-treated for 18 hours with cNLP, curDMSO, or 0.1% DMSO alone prior to IR (50 cGy ^{137}Cs gamma rays). Cells were fixed at 15 minutes, 2 hours, 6 hours, or 24 hours following IR. Shown is the mean induced foci count per cell with standard deviation (SD).

cNLP

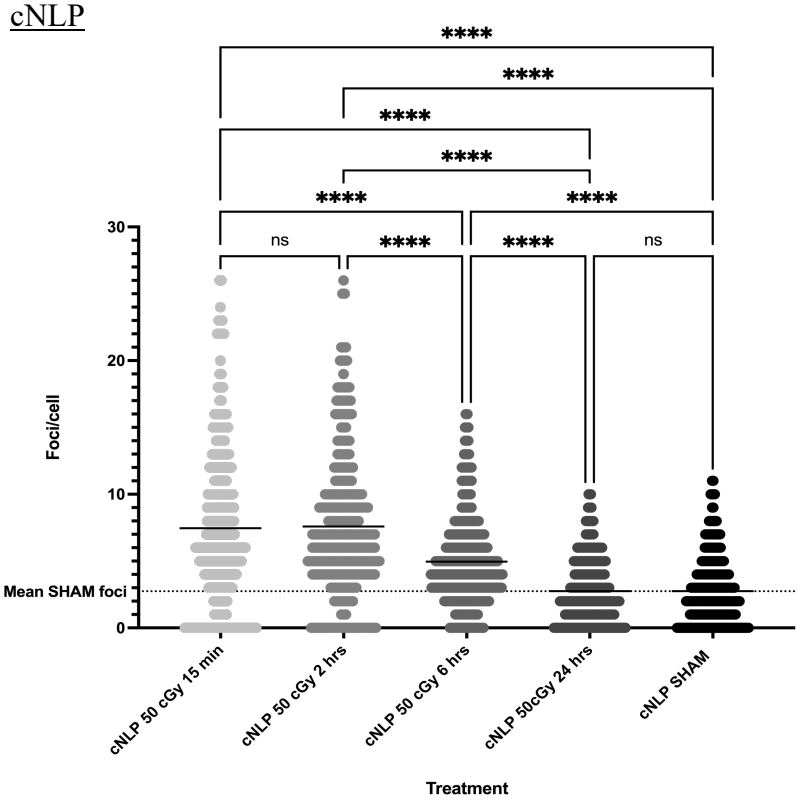

curDMSO

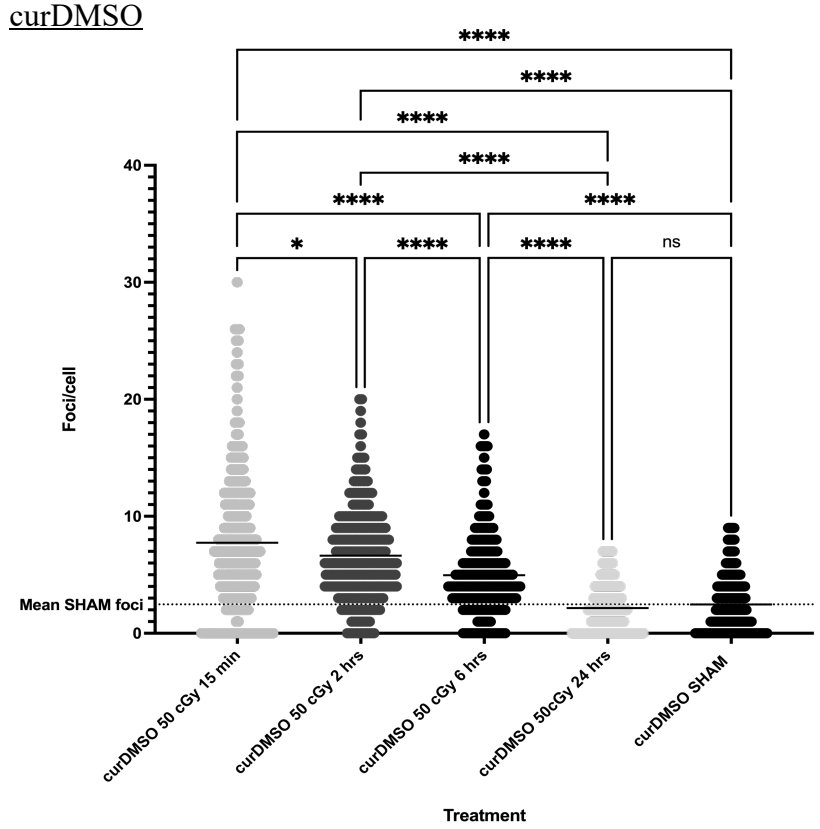

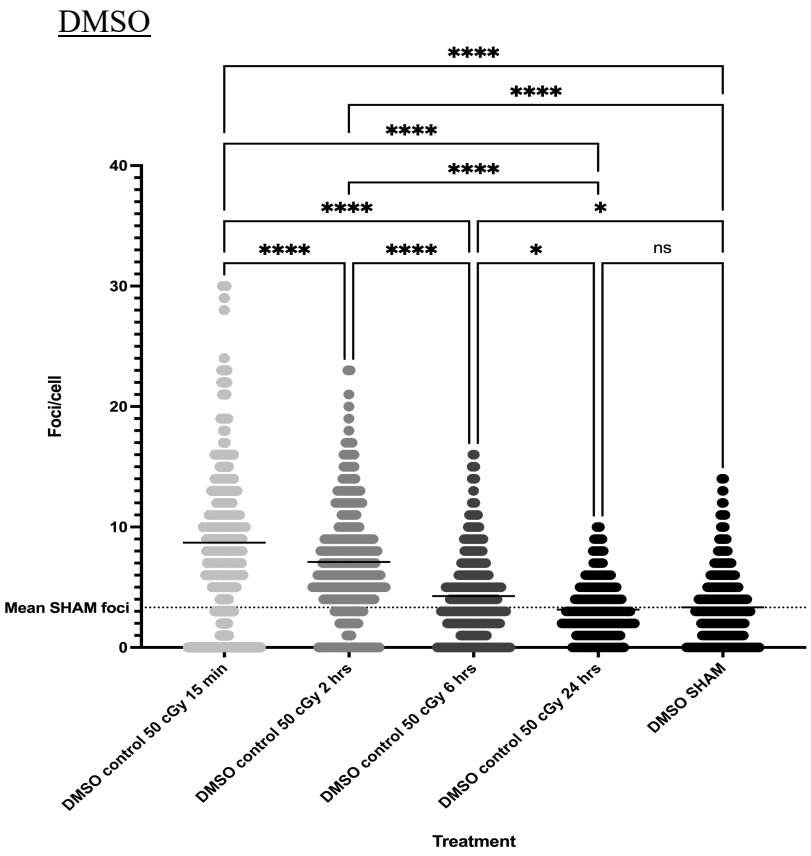

Figure 3.6: Quantification of foci from MRC-5 cells following IR exposure. Cells were pre-treated for 18 hours with cNLP, curDMSO, or 0.1% DMSO prior to IR (50 cGy or SHAM). Cells were fixed 15 minutes, 2 hours, 6 hours, or 24 hours after irradiation and immunostained with DSB markers gamma-H2AX/pSer139 and 53BP1. All outliers have been removed. The black line represents the mean foci/cell per treatment group. Statistics are One-Way ANOVA.

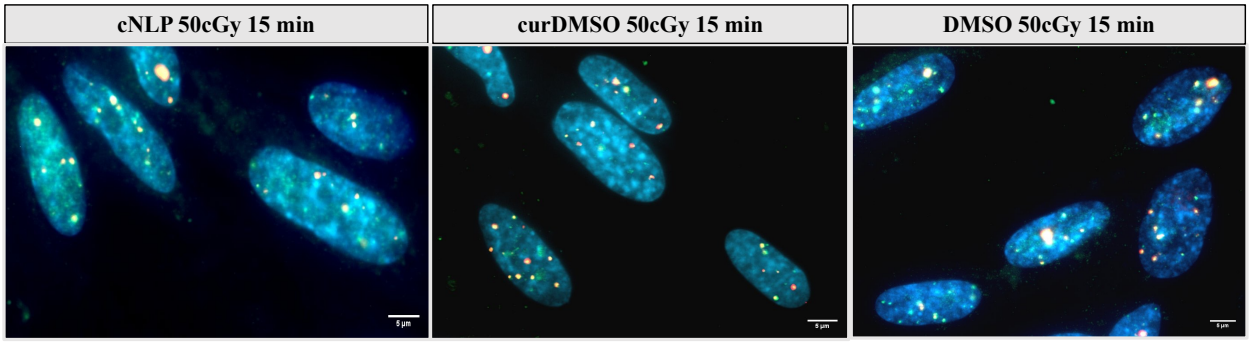

Figure 3.7: Curcumin pre-treatment does not protect against DSB foci formation. Representative images of MRC-5 cells treated with cNLP, curDMSO, and DMSO alone and irradiated with 50 cGy ^{137}Cs rays are shown at the 15-minute fixation time point. Cells were stained for gamma H2AX/pSer139 (green), 53BP1 (red), and DAPI (blue). Scale bar is 5 microns.

cNLPs offer survival benefit against ^{137}Cs irradiation

We next sought to investigate whether cNLPs could protect against cell survival. MRC-5 cells were pre-treated for 18 hours with cNLPs, empty NLPs, curDMSO, or DMSO and then exposed to 0 cGy (SHAM), 0.5 Gy, 1 Gy, 2 Gy, 4 Gy or 6 Gy of ^{137}Cs gamma rays. Both curDMSO and cNLP pre-treatment offered survival benefits to MRC-5 fibroblasts over empty NLP or DMSO alone controls. Although we saw a slight radioprotective effect seen with DMSO-containing groups (DMSO alone and curDMSO), the average relative survival fractions in cells treated with cNLP (no DMSO) were still above those seen with curDMSO treatments at 2, 4, and 6 Gy. The average relative survival fractions for cNLP vs. curDMSO were the following: 2 Gy (0.832 vs. 0.688), 4 Gy (0.387 vs. 0.232), and 6 Gy (0.143 vs 0.125) across 5 biological replicates (Figure 3.8). Our cNLP treated MRC-5 cells also trended towards higher survival at all doses relative to empty NLP controls (Figure 3.8).

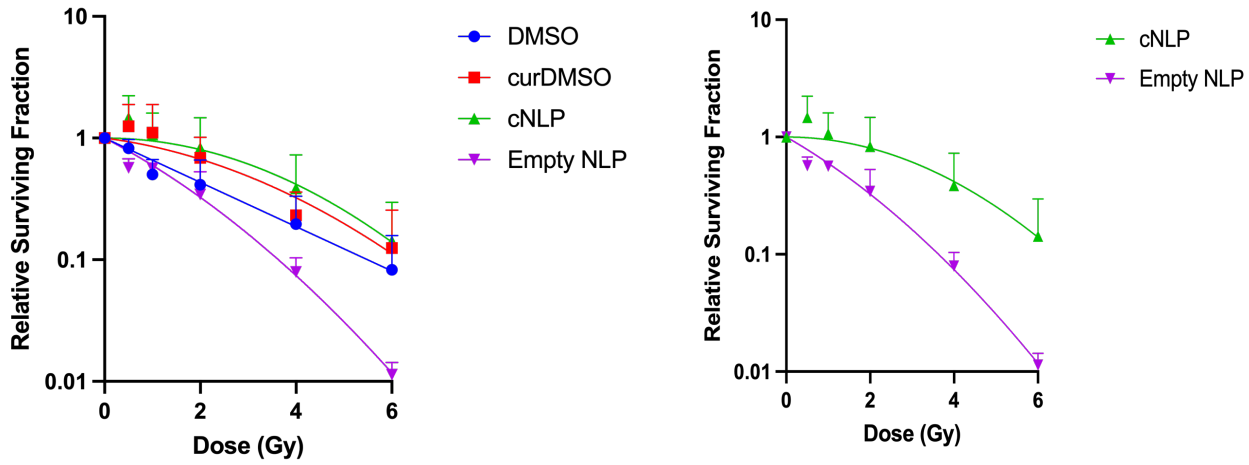

Figure 3.8: Curcumin NLP pre-treatment improves cell survival following ^{137}Cs exposures. MRC-5 cells were pre-treated for 18 hours with cNLP, curDMSO, empty NLP, or 0.1% DMSO alone prior to IR (50 cGy ^{137}Cs gamma rays). Cells are grown for 2 weeks following IR and then fixed and stained. Shown are the mean colony counts per treatment with standard deviation (SD).

3.5 Discussion

Curcumin, the main phytochemical within turmeric, exhibits numerous health benefits including antioxidant, anti-inflammatory, and free-radical scavenging properties that act on a variety of cellular mechanisms, such as inhibition of NF-kB, COX-2, and TNF (6, 27). Curcumin also decreases inflammation associated with multiple disease-states, including Type II diabetes, multiple sclerosis, and rheumatoid arthritis (6).

It is well accepted that curcumin modulates a variety of pathways and transcription factors and can act as both a chemosensitizer and radiosensitizer in a multitude of cancer cell lines and xenograft mouse models (27-30). Recent studies have highlighted potential mechanisms by which curcumin has altered cancer cell death. It has been shown that curcumin treatment activates tumor-suppressor genes p53 and PTEN while suppressing P13K and mTOR pathways, leading to increased apoptosis in cancer cell lines and decreased tumor growth in xenograft mouse models

(31-33). Curcumin has also been explored as a modulator of cancer cell apoptosis by suppressing miR-21 (34, 35) and miR-19 (36), as well as an inducer of autophagy (37) or senescence (38) in numerous cancer cell lines. It has also been shown that curcumin may synergize with other anti-cancer agents, including cisplatin or docetaxel, as well as radiation treatment (39-41).

Although curcumin increases cancer cell death through a variety of mechanisms, it has also been shown that curcumin may, in contrast, provide both chemotherapeutic and radiological protection in normal tissues (28). Srinivasan et al. demonstrated that curcumin pre-treatment on human peripheral blood lymphocytes was able to protect against micronuclei and dicentric chromosomal formation following up to 4 Gy gamma irradiation exposures (8). In addition, Abraham et al. illustrated that curcumin treatment 2 hours before gamma irradiation protected against chromosomal damage in mice (10). Additional *in vivo* studies have shown that mice injected with curcumin either 5 days before or 5 days after a single 50 Gy exposure to the hind leg improved both acute and chronic skin toxicity (42), and curcumin had also decreased associated nephrotoxicity and cardiotoxicity following cisplatin or doxorubicin treatments in rats (28). Furthermore, although curcumin is toxic to cancer stem cells, it demonstrates little to no toxicity to normal stem cells (43). Potential mechanisms at play distinguishing the toxicity of curcumin on cancer cells versus normal cells have suggested that cancer cells preferentially take up much more curcumin than normal cell counterparts (44) which may enhance cytotoxicity. Due to its widespread health benefits and potential to kill cancer cells while protecting normal tissues, curcumin is actively being explored as a therapeutic for a variety of diseases and disorders (3).

Curcumin has proven to be safe and well-tolerated in healthy human volunteers and has demonstrated efficacy against a multitude of clinical ailments (4). In one study, a standardized curcumin formulation NCB-02 (comprised of a mixture of curcumin, demothoxy curcumin, and

bis-demothoxy curcumin) decreased oxidative stress and inflammation in diabetic patients over placebo controls (45). In another study, breast cancer patients undergoing radiation therapy taking 6 mg/day of curcumin capsules orally displayed less radiation dermatitis over placebo groups (46). Furthermore, oxidative damages in thalassemia patients given 500 mg/day curcuminoid treatment were decreased at the end of a 12-month study (47).

Although curcumin acts as a pleiotropic polyphenol studied for its ability to protect against a variety of diseases and inflammatory disorders, its bioavailability is limited due to its poor water solubility. Curcumin lipid formulations therefore remain promising to enhance curcumin bioavailability and therapeutic efficacy. Lipid nanoparticles have been shown to increase curcumin bioavailability through *in vitro* cell cultures and *in vivo* animal models (17, 48, 49). Curcumin nano-formulations have also been explored in the clinic for treating inflammatory diseases. For example, curcumin nano-micelles tested in patients with multiple sclerosis (MS) demonstrated fluctuating miRNA expression levels in peripheral blood lymphocytes following 6 months of treatment, suggesting that curcumin nanodiscs may be immunomodulatory in MS patients (50). Another clinical trial showed increased survival in amyotrophic lateral sclerosis patients treated with 80 mg/day nanocurcumin for 1 year (51).

NLPs are a disc-shaped lipid nanoparticles that can be readily customizable with a variety of lipids, scaffolding proteins, as well as cargo molecules (17). We have previously shown that formulating NLPs with additional telodendrimers, amphiphilic polymers comprised of cholic acid "heads" and polyethylene glycol "tails", can decrease aggregation and may serve as additional scaffolds independent of the apolipoprotein for incorporating a cargo molecule of interest (19, 25). In the current study, formulation and characterization of heterogeneous curcumin-loaded nanodiscs (cNLPs) surrounded by a telodendrimer and/or apolipoprotein scaffold were explored

as potential radiological protectants against DNA damage or cellular survival following 50 cGy ^{137}Cs exposures. Here, we demonstrated that our cNLPs improve bioavailability of curcumin in a normal human fibroblast cell line. These cNLPs also increase curcumin water solubility and are less toxic than curDMSO. They also alter the foci persistence of DNA DSBs and provide some survival benefit to MRC-5 cells following up to 6 Gy of ^{137}Cs exposures.

Robert O. Ryan and colleagues have previously demonstrated enhanced bioavailability of curcumin nanodiscs over free curcumin (curDMSO) *in vitro* (21, 22). In these studies, curcumin nanodiscs with ApoA1 scaffold protein showed increased apoptosis in human hepatoma and lymphoma cell lines over curcumin alone controls (21, 22), and ApoE curcumin nanodiscs demonstrated increased apoptosis and bioavailability in glioblastoma cells (21). Compared to Ryan et al., we similarly incorporated curcumin into a nanodisc using a combination of sonication, centrifugation, and dialysis techniques (22). Here, our final cNLP formulation has similar overall curcumin incorporation to Ryan et al. (~350 μg/ml) and our nanodiscs are also of comparable average size (~43 nm vs 48 nm) (22). However, our methodology of making cNLPs slightly differed, as we added telodendrimer polymers to help solubilize curcumin within lipids and we did not filter out nanodiscs smaller than 0.2 microns as this may have limited our ability to include larger cNLPs. Most importantly, we tested our cNLPs on normal human MRC-5 fibroblasts in contrast to cancer cell lines, demonstrating that our cNLPs enhance the viability and offer some protection against irradiation in a normal *in vitro* cell environment.

It is well-known that the cellular DNA damage response (DDR) is activated following an ionizing radiation exposure (52). Phosphorylation of histone H2AX, forming gamma H2AX and inducing subsequent foci, is a well-accepted biomarker of DNA DSBs following numerous qualities of IR exposures (24, 53). Here, we demonstrated co-localized immunofluorescent

staining of gamma H2AX and 53BP1, a mediator protein also recruited to the site of DNA damage following genotoxic insult (54). Our co-localized immunostained MRC-5 fibroblasts do not detect differences in induced foci formation amongst curcumin treated and DMSO control cells 15 minutes after irradiation, suggesting that curcumin does not affect the induction of DNA DSB following 50 cGy of ^{137}Cs exposures. Interestingly, we detected persistent foci formation in cNLPs at 2 hours post-exposure compared to DMSO alone controls, however, this was not significantly different than the curDMSO groups. We also see slightly increased foci formation between both cNLP and curDMSO at the 6-hour time point compared to cells that did not receive curcumin treatment (Figure 3.5). This suggests that curcumin may delay the timing of DNA repair to complete following IR exposure. A previous study in HeLa cells has shown that curcumin treatment suppresses DNA damage repair processes, including non-homologous end joining (NHEJ), homologous recombination (HR), and DNA damage checkpoints (55). However, by 24 hours after irradiation, no significant differences with induced foci/cell were detected between cNLP, curDMSO, or DMSO alone treated groups and all had returned to baseline levels (Figure 3.5).

In our current study, we see that 10 μg/ml [27 μM] cNLPs protect against normal human MRC-5 fibroblast cell death following 0.5-6 Gy of ^{137}Cs exposures, with the greatest enhanced mean overall survival over empty NLP controls at 4 and 6 Gy (Figure 3.8). A previous report by Lee et al. also investigated curcumin effects on cell survival in a mouse lung carcinoma cell line and showed that 10-25 μM curcumin also affected cell survival, with curcumin enhancing radiation sensitivity following up to 6 Gy gamma exposures (56). Here, we demonstrate that in a normal human fibroblast cell line, curcumin similarly alters radiation response but in favor of cell survival, enhancing radiation protection over empty NLPs or curDMSO groups (Figure 3.8). Although we

determined that this protection was not due to decreases in DNA DSBs, potential mechanisms at play here may be the antioxidant nature of curcumin to scavenge free radicals or increase antioxidant production following radiation exposures (6, 56).

In this study, although average relative survival of cNLP groups outperformed curDMSO or empty NLP controls, we do not see significant differences in the ability of cNLPs to protect against cell survival as each dose had large variability (Figure 3.8). This may be due to the concentration of cNLP used in our experiments (10 μg/ml [27 μM]). It has been previously shown that free curcumin is toxic to cancer cells ≥1 μM (57) and we have similarly demonstrated toxicity in K562 and HL-60 human leukemia cell lines treated with 15-30 μM curcumin (58). However, since normal cells are more resistant to curcumin than cancer cells (43, 44) it is therefore possible that higher curcumin concentrations (above 30 μM) may be beneficial to cell survival following ^{137}Cs exposures. Regardless, this study illustrates the potential for cNLPs to deliver bioavailable curcumin to cells and serve as a potential radiological protectant to normal tissues or as an adjuvant therapeutic for ongoing cancer therapy. Exploring higher curcumin concentrations as well as investigating *in vivo* model systems may reveal additional radioprotective qualities of cNLPs against IR-induced normal tissue toxicities.

The essential findings of this study include successful incorporation of curcumin into a nanodisc with about 350 μg/ml total soluble curcumin in a nano-lipid environment. We also demonstrate that NLPs provide an optimal delivery vehicle for curcumin, enhancing the solubility of curcumin and its bioavailability in normal human fibroblasts. Moreover, our cNLPs are much less toxic to MRC-5 cells than curDMSO, demonstrating the feasibility of cNLPs to be used *in vitro* or *in vivo* in higher quantities. Although we do not see a decreased foci count with curcumin treatment, treating cells with 10 μg/ml curcumin was able to demonstrate mild radiological

protection and enhanced average survival in MRC-5 cells exposed to 0.5-6 Gy gamma rays. These data suggest that cNLPs may be useful as radiological protectants that can be applied in clinical radiotherapy to protect normal tissues. It also suggests the use of cNLPs as an ideal pharmaceutical formulation to protect from chronic low doses of environmental radiological exposures, such as in deep space missions. Overall, our cNLP formulation pipeline serves as a model for forming antioxidant-loaded nanodiscs to increase the water-solubility and bioavailability within *in vitro* normal human cell cultures. In the future, it will be of interest to investigate the effects of cNLPs to protect against radiological stressors *in vivo* or to protect against additional ionizing radiation species altogether.

3.6 Acknowledgements

We would like to acknowledge Wei He for assistance with nanoparticle characterization and the radiobiological experiments. We would like to also acknowledge that Manoj Saxena's current affiliation is the following: Institute of Structural and Molecular Biology, Birkbeck College, University of London, U.K. This work is supported by the NASA/Baylor Translational Research Institute for Space Health (TRISH) through Cooperative Agreement NNX16AO69A. Work was also performed under the auspices of the U.S. Department of Energy by Lawrence Livermore National Laboratory under contract DE-AC52-07NA27344. This work was also supported with funding from the Laboratory Directed Research Development program at LLNL.

Chapter 3 References:

1. Hewlings SJ, Kalman DS. Curcumin: A Review of Its Effects on Human Health. Foods. 2017;6(10).

2. Gopinath H, Karthikeyan K. Turmeric: A condiment, cosmetic and cure. Indian J Dermatol Venereol Leprol. 2018;84(1):16-21.
3. Xu XY, Meng X, Li S, Gan RY, Li Y, Li HB. Bioactivity, Health Benefits, and Related Molecular Mechanisms of Curcumin: Current Progress, Challenges, and Perspectives. Nutrients. 2018;10(10).
4. Kunnumakkara AB, Bordoloi D, Padmavathi G, Monisha J, Roy NK, Prasad S, et al. Curcumin, the golden nutraceutical: multitargeting for multiple chronic diseases. Br J Pharmacol. 2017;174(11):1325-48.
5. Lao CD, Ruffin MTt, Normolle D, Heath DD, Murray SI, Bailey JM, et al. Dose escalation of a curcuminoid formulation. BMC Complement Altern Med. 2006;6:10.
6. Aggarwal BB, Surh Y-J, Shishodia S. The molecular targets and therapeutic uses of curcumin in health and disease. New York, NY: Springer; 2007. xxi, 489 p. p.
7. Weiss JF, Landauer MR. Protection against ionizing radiation by antioxidant nutrients and phytochemicals. Toxicology. 2003;189(1-2):1-20.
8. Srinivasan M, Rajendra Prasad N, Menon VP. Protective effect of curcumin on gamma-radiation induced DNA damage and lipid peroxidation in cultured human lymphocytes. Mutat Res. 2006;611(1-2):96-103.
9. Jagetia GC, Rajanikant GK. Acceleration of wound repair by curcumin in the excision wound of mice exposed to different doses of fractionated gamma radiation. Int Wound J. 2012;9(1):76-92.
10. Abraham SK, Sarma L, Kesavan PC. Protective effects of chlorogenic acid, curcumin and beta-carotene against gamma-radiation-induced in vivo chromosomal damage. Mutat Res. 1993;303(3):109-12.
11. Anand P, Kunnumakkara AB, Newman RA, Aggarwal BB. Bioavailability of curcumin: problems and promises. Mol Pharm. 2007;4(6):807-18.
12. Rinwa P, Kumar A. Piperine potentiates the protective effects of curcumin against chronic unpredictable stress-induced cognitive impairment and oxidative damage in mice. Brain Res. 2012;1488:38-50.
13. Shoba G, Joy D, Joseph T, Majeed M, Rajendran R, Srinivas PS. Influence of piperine on the pharmacokinetics of curcumin in animals and human volunteers. Planta Med. 1998;64(4):353-6.
14. Feng T, Wei Y, Lee RJ, Zhao L. Liposomal curcumin and its application in cancer. Int J Nanomedicine. 2017;12:6027-44.
15. Li L, Ahmed B, Mehta K, Kurzrock R. Liposomal curcumin with and without oxaliplatin: effects on cell growth, apoptosis, and angiogenesis in colorectal cancer. Mol Cancer Ther. 2007;6(4):1276-82.
16. Bisht S, Feldmann G, Soni S, Ravi R, Karikar C, Maitra A, et al. Polymeric nanoparticle-encapsulated curcumin ("nanocurcumin"): a novel strategy for human cancer therapy. J Nanobiotechnology. 2007;5:3.
17. Fischer NO, Weilhammer DR, Dunkle A, Thomas C, Hwang M, Corzett M, et al. Evaluation of nanolipoprotein particles (NLPs) as an in vivo delivery platform. PLoS One. 2014;9(3):e93342.
18. He W, Evans AC, Rasley A, Bourguet F, Peters S, Kamrud KI, et al. Cationic HDL mimetics enhance in vivo delivery of self-replicating mRNA. Nanomedicine. 2020;24:102154.

19. He W, Felderman M, Evans AC, Geng J, Homan D, Bourguet F, et al. Cell-free production of a functional oligomeric form of a Chlamydia major outer-membrane protein (MOMP) for vaccine development. J Biol Chem. 2017;292(36):15121-32.
20. He W, Scharadin TM, Saldana M, Gellner C, Hoang-Phou S, Takanishi C, et al. Cell-free expression of functional receptor tyrosine kinases. Sci Rep. 2015;5:12896.
21. Ghosh M, Ryan RO. ApoE enhances nanodisk-mediated curcumin delivery to glioblastoma multiforme cells. Nanomedicine (Lond). 2014;9(6):763-71.
22. Ghosh M, Singh AT, Xu W, Sulchek T, Gordon LI, Ryan RO. Curcumin nanodisks: formulation and characterization. Nanomedicine. 2011;7(2):162-7.
23. Krishnamoorthy A, Tavoosi N, Chan GKL, Liu J, Ren G, Cavigiolio G, et al. Effect of curcumin on amyloid-like aggregates generated from methionine-oxidized apolipoprotein A-I. FEBS Open Bio. 2018;8(2):302-10.
24. Wilson PF, Nham PB, Urbin SS, Hinz JM, Jones IM, Thompson LH. Inter-individual variation in DNA double-strand break repair in human fibroblasts before and after exposure to low doses of ionizing radiation. Mutat Res. 2010;683(1-2):91-7.
25. He W, Luo J, Bourguet F, Xing L, Yi SK, Gao T, et al. Controlling the diameter, monodispersity, and solubility of ApoA1 nanolipoprotein particles using telodendrimer chemistry. Protein Sci. 2013;22(8):1078-86.
26. Vasudevan S, Prabhune AA. Photophysical studies on curcumin-sophorolipid nanostructures: applications in quorum quenching and imaging. R Soc Open Sci. 2018;5(2):170865.
27. Mortezaee K, Salehi E, Mirtavoos-Mahyari H, Motevaseli E, Najafi M, Farhood B, et al. Mechanisms of apoptosis modulation by curcumin: Implications for cancer therapy. J Cell Physiol. 2019;234(8):12537-50.
28. Goel A, Aggarwal BB. Curcumin, the golden spice from Indian saffron, is a chemosensitizer and radiosensitizer for tumors and chemoprotector and radioprotector for normal organs. Nutr Cancer. 2010;62(7):919-30.
29. Kunnumakkara AB, Diagaradjane P, Anand P, Harikumar KB, Deorukhkar A, Gelovani J, et al. Curcumin sensitizes human colorectal cancer to capecitabine by modulation of cyclin D1, COX-2, MMP-9, VEGF and CXCR4 expression in an orthotopic mouse model. Int J Cancer. 2009;125(9):2187-97.
30. Li J, Xiang S, Zhang Q, Wu J, Tang Q, Zhou J, et al. Combination of curcumin and bicalutamide enhanced the growth inhibition of androgen-independent prostate cancer cells through SAPK/JNK and MEK/ERK1/2-mediated targeting NF-kappaB/p65 and MUC1-C. J Exp Clin Cancer Res. 2015;34:46.
31. Fu H, Wang C, Yang D, Wei Z, Xu J, Hu Z, et al. Curcumin regulates proliferation, autophagy, and apoptosis in gastric cancer cells by affecting PI3K and P53 signaling. J Cell Physiol. 2018;233(6):4634-42.
32. Rana C, Piplani H, Vaish V, Nehru B, Sanyal SN. Downregulation of PI3-K/Akt/PTEN pathway and activation of mitochondrial intrinsic apoptosis by Diclofenac and Curcumin in colon cancer. Mol Cell Biochem. 2015;402(1-2):225-41.
33. Wang Z, Liu F, Liao W, Yu L, Hu Z, Li M, et al. Curcumin suppresses glioblastoma cell proliferation by p-AKT/mTOR pathway and increases the PTEN expression. Arch Biochem Biophys. 2020;689:108412.

34. Qiang Z, Meng L, Yi C, Yu L, Chen W, Sha W. Curcumin regulates the miR-21/PTEN/Akt pathway and acts in synergy with PD98059 to induce apoptosis of human gastric cancer MGC-803 cells. J Int Med Res. 2019;47(3):1288-97.
35. Wang X, Hang Y, Liu J, Hou Y, Wang N, Wang M. Anticancer effect of curcumin inhibits cell growth through miR-21/PTEN/Akt pathway in breast cancer cell. Oncol Lett. 2017;13(6):4825-31.
36. Li X, Xie W, Xie C, Huang C, Zhu J, Liang Z, et al. Curcumin modulates miR-19/PTEN/AKT/p53 axis to suppress bisphenol A-induced MCF-7 breast cancer cell proliferation. Phytother Res. 2014;28(10):1553-60.
37. Zhang Q, Qiao H, Wu D, Lu H, Liu L, Sang X, et al. Curcumin potentiates the galbanic acid-induced anti-tumor effect in non-small cell lung cancer cells through inhibiting Akt/mTOR signaling pathway. Life Sci. 2019;239:117044.
38. Mosieniak G, Adamowicz M, Alster O, Jaskowiak H, Szczepankiewicz AA, Wilczynski GM, et al. Curcumin induces permanent growth arrest of human colon cancer cells: link between senescence and autophagy. Mech Ageing Dev. 2012;133(6):444-55.
39. Deng L, Wu X, Zhu X, Yu Z, Liu Z, Wang J, et al. Combination effect of curcumin with docetaxel on the PI3K/AKT/mTOR pathway to induce autophagy and apoptosis in esophageal squamous cell carcinoma. Am J Transl Res. 2021;13(1):57-72.
40. Lv Xiao-ai WB, Xu Xiao-hong, Pan Lei, Wang Bin, Dong Xiao-xue, Zheng Chen-huia and Du Qi-weia Curcumin re-sensitizes multidrug resistant (MDR) breast cancer to cisplatin through inducing autophagy by decreasing CCAT1 expression. RSC Advances. 2017;7:33572-9.
41. Deng XZ, Geng SS, Luo M, Chai JJ, Xu Y, Chen CL, et al. Curcumin potentiates laryngeal squamous carcinoma radiosensitivity via NF-KappaB inhibition by suppressing IKKgamma expression. J Recept Signal Transduct Res. 2020;40(6):541-9.
42. Okunieff P, Xu J, Hu D, Liu W, Zhang L, Morrow G, et al. Curcumin protects against radiation-induced acute and chronic cutaneous toxicity in mice and decreases mRNA expression of inflammatory and fibrogenic cytokines. Int J Radiat Oncol Biol Phys. 2006;65(3):890-8.
43. Sordillo PP, Helson L. Curcumin and cancer stem cells: curcumin has asymmetrical effects on cancer and normal stem cells. Anticancer Res. 2015;35(2):599-614.
44. Kunwar A, Barik A, Mishra B, Rathinasamy K, Pandey R, Priyadarsini KI. Quantitative cellular uptake, localization and cytotoxicity of curcumin in normal and tumor cells. Biochim Biophys Acta. 2008;1780(4):673-9.
45. Usharani P, Mateen AA, Naidu MU, Raju YS, Chandra N. Effect of NCB-02, atorvastatin and placebo on endothelial function, oxidative stress and inflammatory markers in patients with type 2 diabetes mellitus: a randomized, parallel-group, placebo-controlled, 8-week study. Drugs R D. 2008;9(4):243-50.
46. Ryan JL, Heckler CE, Ling M, Katz A, Williams JP, Pentland AP, et al. Curcumin for radiation dermatitis: a randomized, double-blind, placebo-controlled clinical trial of thirty breast cancer patients. Radiat Res. 2013;180(1):34-43.
47. Kalpravidh RW, Siritanaratkul N, Insain P, Charoensakdi R, Panichkul N, Hatairaktham S, et al. Improvement in oxidative stress and antioxidant parameters in beta-thalassemia/Hb E patients treated with curcuminoids. Clin Biochem. 2010;43(4-5):424-9.
48. Ban C, Jo M, Park YH, Kim JH, Han JY, Lee KW, et al. Enhancing the oral bioavailability of curcumin using solid lipid nanoparticles. Food Chem. 2020;302:125328.

49. Wang W, Chen T, Xu H, Ren B, Cheng X, Qi R, et al. Curcumin-Loaded Solid Lipid Nanoparticles Enhanced Anticancer Efficiency in Breast Cancer. Molecules. 2018;23(7).
50. Dolati S, Aghebati-Maleki L, Ahmadi M, Marofi F, Babaloo Z, Ayramloo H, et al. Nanocurcumin restores aberrant miRNA expression profile in multiple sclerosis, randomized, double-blind, placebo-controlled trial. J Cell Physiol. 2018;233(7):5222-30.
51. Ahmadi M, Agah E, Nafissi S, Jaafari MR, Harirchian MH, Sarraf P, et al. Safety and Efficacy of Nanocurcumin as Add-On Therapy to Riluzole in Patients With Amyotrophic Lateral Sclerosis: A Pilot Randomized Clinical Trial. Neurotherapeutics. 2018;15(2):430-8.
52. Thompson LH. Recognition, signaling, and repair of DNA double-strand breaks produced by ionizing radiation in mammalian cells: the molecular choreography. Mutat Res. 2012;751(2):158-246.
53. Redon CE, Dickey JS, Bonner WM, Sedelnikova OA. gamma-H2AX as a biomarker of DNA damage induced by ionizing radiation in human peripheral blood lymphocytes and artificial skin. Adv Space Res. 2009;43(8):1171-8.
54. FitzGerald JE, Grenon M, Lowndes NF. 53BP1: function and mechanisms of focal recruitment. Biochem Soc Trans. 2009;37(Pt 4):897-904.
55. Ogiwara H, Ui A, Shiotani B, Zou L, Yasui A, Kohno T. Curcumin suppresses multiple DNA damage response pathways and has potency as a sensitizer to PARP inhibitor. Carcinogenesis. 2013;34(11):2486-97.
56. Lee JC, Kinniry PA, Arguiri E, Serota M, Kanterakis S, Chatterjee S, et al. Dietary curcumin increases antioxidant defenses in lung, ameliorates radiation-induced pulmonary fibrosis, and improves survival in mice. Radiat Res. 2010;173(5):590-601.
57. Yu C, Yang B, Najafi M. Targeting of cancer cell death mechanisms by curcumin; implications to cancer therapy. Basic Clin Pharmacol Toxicol. 2021.
58. Martinez-Castillo M, Villegas-Sepulveda N, Meraz-Rios MA, Hernandez-Zavala A, Berumen J, Coleman MA, et al. Curcumin differentially affects cell cycle and cell death in acute and chronic myeloid leukemia cells. Oncol Lett. 2018;15(5):6777-83.

Chapter 4: Curcumin nanoparticles alter gene expression and pathway activation in primary human fibroblasts following simulated ionizing radiation exposures relevant to deep space missions

Authors:

Angela C. Evans[1], Aimy Sebastian[2], Kelly Martin[2], Nick Hum[2], Gaby Loots[2], Elizabeth Wheeler[2], Graça Almeida-Porada[3], Christopher D. Porada[3], Paul F. Wilson[1], and Matthew A. Coleman[1,2]

[1]Department of Radiation Oncology, University of California Davis, Sacramento, CA, USA.

[2]Lawrence Livermore National Laboratory, Livermore, CA, USA.

[3]Wake Forest Institute for Regenerative Medicine, Winston-Salem, NC, USA

4.1 Abstract

Environmental radiation exposures in deep space pose significant health risks and may lead to acute or latent ionizing radiation (IR)-induced toxicities including hematopoietic depletion, cellular dysfunction, cognitive neurological deficits, or secondary cancer development. Therefore, for future long-term space travel, there is a need to develop safe and effective radiological protectants or countermeasures. An ideal radiation countermeasure needs to be readily available, have a long shelf-life, show little to no toxicity *in vivo*, and show efficacy when administered concomitantly with other supplements while onboard the spacecraft (1). It has been suggested that food-derived compounds may satisfy these criteria and include natural products such as vitamins (e.g. vitamin C, vitamin E), polyphenols (e.g. curcumin), as well as non-polyphenols (e.g. caffeine) (2, 3). Here, we demonstrate that curcumin, a natural antioxidant found within the spice turmeric, shows potential as a non-toxic and safe pharmaceutical countermeasure for use on deep space

missions. We solubilized curcumin within a nanolipoprotein particle (NLP) disc and treated normal human fetal lung fibroblasts with 10 μg/ml [27 uM] curcumin prior to (radioprotection) or shortly after (radiomitigation) simulated space radiation exposures at the Nasa Space Radiation Laboratory (NSRL). RNA was isolated from cells for differential transcriptomic analyses to identify differentially expressed genes and biological pathways in cNLP radioprotection and radiomitigation treatments compared to IR alone controls. Namely, curcumin NLP treatment altered gene expression differently than IR-alone control groups, activated key antioxidant response genes within the Nrf2 pathway, and modulated select p53 transcripts independent of IR exposures and more so than curcumin dissolved in DMSO. These findings may be useful for establishing curcumin NLPs as effective radiation medical countermeasures (MCM) against environmental IR exposures in deep space.

4.2 Introduction

Environmental radiation exposures in space, comprised of complex electromagnetic and particulate ionizing radiation (IR) mixtures, pose great risks to human health and especially when traveling beyond low earth orbit (LEO) (Figure 4.1). Associated sources of radiation in space include the sun's solar plasma, Van Allen radiation belts, high-proton flux of solar particle events (SPE), as well as chronic low-dose exposures to galactic cosmic radiation (GCR) (4). Radiation risks for astronauts traveling beyond LEO, such as a planned three-year exploration to Mars, increase following exposures to these unique IR qualities. It is believed that IR exposures throughout long-duration space flight will primarily arise from the potential for an acute, high-dose exposure to a SPE as well as the chronic low-dose exposure to GCR and its associated heavy ion (HZE) species (5).

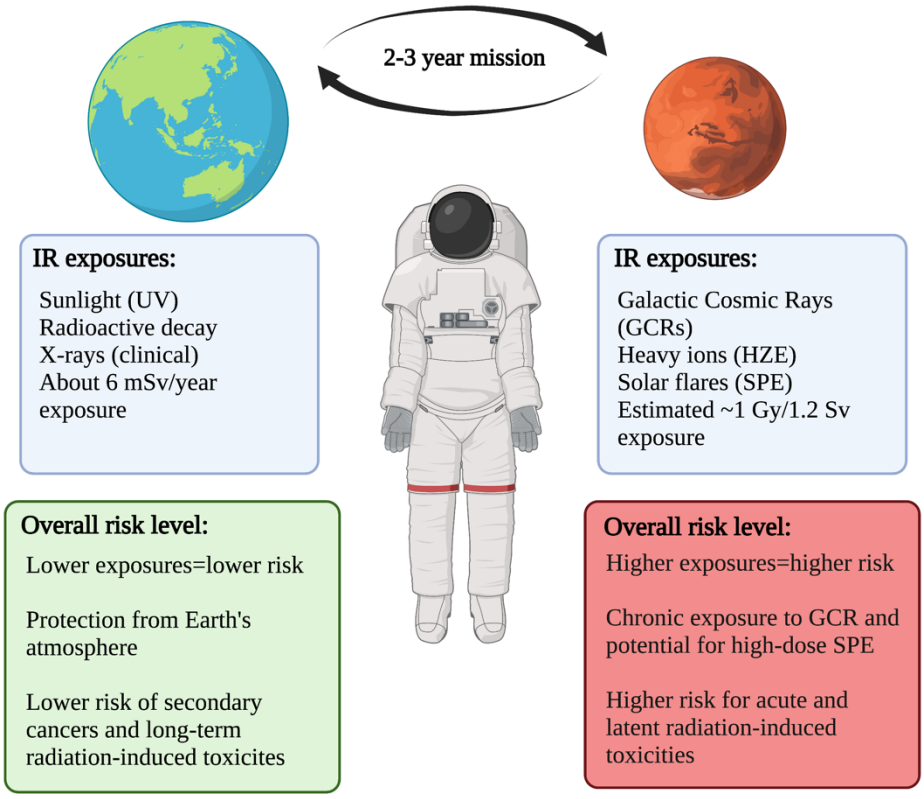

Figure 4.1: Environmental IR exposure types and associated risks differ between Earth and space. *Left:* Earth-bound ionizing radiation exposures include ultraviolet rays as well as minimal exposures to radioactive elements within the Earth's crust. Occasional acute exposures may also occur in the clinic, such as an X-ray or a radiation therapy treatment. *Right:* Throughout long-term space travel, such as a trip to Mars, astronauts will be exposed to more complex radiation qualities, including GCRs and SPEs. While traveling throughout space, astronauts will also be exposed to higher overall doses, increasing his or her risk for developing subsequent IR-induced toxicities.

Cumulative IR exposures for astronauts on a 2-3 year Mars mission is estimated to be about 0.5-1 Gy absorbed dose, or 0.7-1.2 Sv biological equivalent dose (4, 6, 7). Given their high charge and radiation quality factor weightings, HZE particles contribute about 87% of total dose equivalent in free space. However, beyond typical spacecraft shielding, this total dose equivalent becomes predominated by protons and light ions (7). Space exposure, like other types of IR, may lead to skin lesions (primarily through high-dose SPE flares), hematological and immune system dysfunction, neural behavioral changes, cardiovascular disease, or secondary cancers (4, 8).

Acute radiation syndrome (ARS), also known as radiation sickness, is characterized by high-doses (>4 Gy) of total body irradiation delivered over a very short period of time (usually within minutes). Although space radiation is generally characterized by chronic low-dose GCR particles, ARS symptoms may occur in the event of an acute, high-dose SPE (4, 6). In the event of ARS onset, astronauts may develop rapid fevers, infections, disorientation, and death if not promptly treated (9).

Given the increased radiation risks associated with space flight beyond LEO, there remains a need to better understand the relative biological effectiveness (RBE) following these complex mixed-ion exposures. Moreover, learning more about the RBE induced by GCR exposures will aid in the development of effective radiological protectants and countermeasures.

As of 2018, the NASA Space Radiation Laboratory (NSRL) at Brookhaven National Laboratory can simulate the deep space environment through their full 33-ion or simplified 5-ion GCR simulator beams (7). In either case, these mixed-ion beams were designed to approximate the relevant particle flux that would hit target tissues and organs within the spacecraft environment (7). To date, there are limited published studies investigating the biological effects following GCR-simulated exposures. Regardless, several studies have tested the effects of single-ion protons or HZE particles *in vitro* and *in vivo* which are still relevant for deep space missions and for estimating radiation-induced toxicities. Specifically, Rodman et al. discovered that human hematopoiesis was altered following proton and Fe-56 exposures and that 20 cGy Fe-56 ion exposures led to leukemogenic-like transformations *in vivo* (10). In addition, a mixture of sequential exposures to proton and Fe-56 ions led to marked biological damage in both hematopoietic stem cell and mesenchymal stem cell lineages (10, 11). Furthermore, mitochondrial dysfunction in mouse livers was identified following 0.2 Gy of Fe-56, Si-28, and O-16 HZE

exposures (12). It remains evident that a better understanding of human responses to mixed field GCR exposures, including further evidence for potential mechanisms at play, is needed to minimize radiation-induced cellular damage and develop effective countermeasures for deep space flight.

There are two main radiation countermeasure strategies for deep space flight missions; enhancing the radio-resistance of one's body prior to space flight through preventative care measures or supplementing the body with pharmacological agents throughout the mission to combat radiation-induced toxicities (1). As a strategy to address the latter, current radiation protection agents of interest include natural food-derived compounds or nutripharmaceuticals due to their 1) minimal toxicity profiles, 2) ease of combining them with other medications on board, and 3) long shelf life (1). Several natural products have been explored as radiation protective agents to date, including vitamins (Vitamin C, Vitamin E, Vitamin A), polyphenols (green tea, resveratrol, curcumin), and non-polyphenols (caffeine) (2). Within this chapter, we will focus on curcumin, which has been explored as a radiation protection agent in a variety of model systems and is well-tolerated for human consumption (13).

Curcumin has long been sought out for its pleotropic health benefits, including antioxidant and anti-inflammatory properties. Although curcumin bioavailability is normally quite low, we showed in the previous chapter (Chapter 3) that curcumin can be readily formulated into a nanodisc (cNLP), increasing its bioavailability in cell culture without compromising feasibility of formulation and ease of administration. We also demonstrated that cNLPs have a mild radioprotective effect in cells exposed to Cs-137 gamma rays over empty NLP controls and a comparable radioprotective effect to curcumin dissolved in DMSO (Chapter 3, Figure 3.8).

In this chapter (Chapter 4), we expand upon our Chapter 3 findings and investigate the transcriptional profile, DNA damage kinetics, and biological pathways that are altered in human fetal lung fibroblasts following curcumin treatment and IR exposures. Our study investigates the effect of 5-ion simulated GCR exposures compared to single ion proton particles, HZE species (Fe-56), and low-LET gamma rays. We examined the radioprotective and radiomitigative qualities of cNLPs on simulated GCR exposures as well as the impact that they have on downstream biological pathways in normal human fibroblasts. These findings illustrate the potential of cNLPs to serve as a novel radiation countermeasure for astronauts traveling in deep space, as well as elucidate potential pathways of interest for optimizing additional radiotherapeutics for future Mars missions.

4.3 Materials and Methods

Cell culture

AG05965/MRC-5 normal primary human fetal lung fibroblasts (derived from Caucasian male) were maintained in MEMα with 1X GlutaMAX media (GIBCO/Invitrogen #32571). Media was supplemented with 15% FBS, 0.8% PenStrep (GIBCO/Invitrogen #15140), 0.8% MEM Vitamins (GIBCO/Invitrogen #11120), 0.8% MEM (Essential) Amino Acids Solution (GIBCO/Invitrogen #11130), 0.8% MEM Non-Essential Amino Acids Solution (GIBCO/Invitrogen #11140), and 4 mM NaOH. Cell culture media was filtered through a 0.2-micron PES filter before use. Cells were cultured in a 37°C incubator with 5% CO_2. Experiments were conducted with cells below 20 passages.

Irradiation Experiments

Confluent MRC-5 fibroblasts in T-25 flasks (transcriptomics) or Nunc flaskettes (DNA damage immunohistochemistry) were shipped to the Nasa Space Radiation Laboratory (NSRL) at Brookhaven National Laboratory in Upton, NY at least 24 hours prior to irradiation experiments. At NSRL, radiation protection groups were pre-treated for ~18 hours with 10 μg/ml [27 μM] cNLPs, 10 μg/ml [27 μM] curcumin in DMSO (curDMSO), or 0.1% DMSO (IR alone) control. During active beam time, cells were irradiated with the following ion species: 5-ion SimGCRSim (75cGy), Fe-56 particles (25 or 50 cGy), O-16 particles (25 or 50 cGy), H-1 protons (50 or 100 cGy), Si-28 particles (25 or 50 cGy), and Cs-137 gamma rays (50 or 100 cGy). For radiation mitigation groups, cells were treated with 10 μg/ml [27 μM] cNLPs 15 minutes after the cells were irradiated. Note: Repeat experiments of the gamma irradiation experiments were also performed at Lawrence Livermore National Laboratory in Livermore, CA. SHAM samples are not irradiated but were treated and collected in the same manner alongside corresponding irradiated samples.

For the purposes of this study, top priority irradiation groups most relevant to space flight (GCR and H-1 particles) are listed in the main chapter figures for direct comparison to gamma irradiated groups. Fe-56 irradiations were also included in the main text as needed to perform a HZE particle comparison. Second priority irradiation groups consisted of additional HZE species (Silicon-28 and Oxygen-16) irradiations and served to investigate biological effects of LET differences. The second priority IR groups and corresponding figures are primarily listed in the Appendix. Table 4.1 outlines the dose(s) of exposure applied per IR quality and associated LET levels.

IR Type	Dose(s) of Exposure (cGy)	LET (keV/µM)		
SHAM	0	N/A		
Gamma	50, 100	0.8		
Proton	50, 100	1.26		
Oxygen	25, 50	20.9		
Silicon	25, 50	50.47		
Fe	25, 50	151.4		
GCR	75	Ion	Fraction	LET
		1 GeV ^{1}H	0.35	0.22 keV/µM
		600 MeV/n ^{28}Si	0.01	50.47 keV/µM
		250 MeV/n ^{4}He	0.18	1.58 keV/µM
		350 MeV/n ^{16}O	0.06	20.90 keV/µM
		600 MeV/n ^{56}Fe	0.01	174.07 keV/µM
		250 MeV ^{1}H	0.39	0.39 keV/µM

Table 4.1. Various qualities of IR used within this chapter and corresponding LET levels.

DNA Damage

a. Cell collections

Confluent MRC-5 cells (see above "Cell culture") were irradiated at NSRL and then returned to incubator for deactivation. Samples were fixed at 15, 120, 360 and 1440 min following IR by aspirating medium, rinsing gently 2X with 1X DPBS (+$Ca^{2+/}Mg^{2+}$), and fixed for 15 min with 4% Paraformaldehyde in 1X PBS. Following fixation, PFA was aspirated and flaskettes were rinsed 3X with DPBS for 5 min each on rocker and then filled with DPBS, capped, and resealed with Parafilm and stored at 4°C until immunostaining.

b. Immunohistochemistry

After cell fixation (see above "Cell collections"), cells were immunostained in the same manner as is written in Chapter 3. In brief, chambers were rinsed (2x5 min) with room-temperature (RT) DPBS on rocker, permeabilized with ice-cold PBS with 0.5% Triton X-100 for 10 minutes, then rinsed (2x5 min) with RT DPBS. Samples were then treated with Image-iT™ FX Signal Enhancer solution (Thermo Fisher) for 30 minutes and then rinsed (2x5 min) with RT DPBS. Samples were then blocked with 2% goat serum, 2% FBS, 1% BSA, 0.1% Triton X-100, and 0.05% Tween-20 in PBS at RT for 30–60 minutes on a rocker and rinsed with RT DPBS. After slides were separated from cassette, primary antibody solutions of 1:250 Upstate mouse anti-phosphoH2AX JBW301 (Millipore) and 1:250 rabbit anti-53BP1 (Novus) in PBS with 1% BSA were then loaded on slide, overlayed with coverslip, and incubated horizontally in a 37°C humid chamber for 30–60 minutes. Slides were rinsed (3x5 minutes) in RT DPBS in covered Coplin jars. Secondary antibodies 1:500 Molecular Probes Alexa-488-conjugated goat anti-mouse IgG (Thermo Fisher Scientific) and 1:500 Molecular Probes Alexa-594-conjugated goat anti-rabbit IgG (Thermo Fisher Scientific) were prepped in PBS alone (no BSA) and mounted on slide with overlaying coverslip and incubated horizontally in a dark 37°C humid chamber for 30–60 minutes. Slides were then rinsed with (2x5 min) and then (1x10 min) washes in DPBS. Slides were then incubated in freshly prepared RT 3.7% paraformaldehyde in PBS for 10 minutes followed by (2x5 min) rinses with DPBS. After the final rinse, excess PBS was removed from slides and slides were treated with RT Molecular Probes ProLong Gold with 0.2 µg/ml DAPI (Thermo Fisher) and overlayed with a 24 mm x 50 mm coverslip. Slides were cured overnight at RT in a light-tight slide box and then transferred to the refrigerator the following day and stored at 4°C until imaging.

Slides were imaged on a Carl Zeiss microscope using Zen Software at 63x magnification. Over 250 cells were counted per experimental time point.

Transcriptomics

a. Cell collections

After irradiation, cells were left undisturbed in a 37°C incubator with 5% CO_2 for 24 hours. After 24 hours of incubation, cell media was aspirated and cells were trypsinized with ~2 ml of 0.25% Trypsin:EDTA. After trypsinization, fresh media was added, and the cells were pooled amongst treatment groups and aliquoted into 15-ml conical tubes. Cells were then centrifuged at 1500 rpm for 3 minutes, supernatant was discarded, and then the pellet was re-suspended in ~3 mL 1X DPBS ($+Ca^{2+}/Mg^{2+}$) and centrifuged again at 1500 rpm for 3 minutes. Following centrifugation, the resulting supernatant was discarded and ~350 µL of RNALater solution (Qiagen) was added on top of the cell pellet. Tubes were then placed in -20°C for short-term storage and -80°C for long term storage until RNA extraction for RNA sequencing or quantitative real-time PCR.

b. RNA extraction

Cell pellets were prepared for RNA extraction by removing RNALater solution and mixing cell contents with RLT storage buffer (Qiagen) supplemented with 10 µl beta-mercaptoethanol per ml RLT. Total RNA was extracted using the RNeasy Mini Kit (Qiagen) according to the manufacturer's instructions. RNA was eluted in RNase-free water. RNA concentrations were quantified using a Qubit RNA HS Assay Kit (Thermo Fisher Scientific) and Nanodrop One^C (Thermo Fisher Scientific). RNA quality was determined via A260/280 and A260/A230 absorbance via Nanodrop. A260/A280 values averaged 2.045 and A260/A230 values averaged

2.038. The average RIN value collected was 9.81 and was measured with the RNA 6000 Nano kit run on an Agilent 2100 Bioanalyzer (Agilent Technologies).

c. RNA sequencing

All cDNA libraries were prepared from 100 ng of total isolated RNA per manufacturer specification for RNA sequencing using Illumina TruSeq RNA Library Preparation kit version 2.0 (Illumina Inc.) and run on an Illumina Nextseq 500 using the High Output 75 cycles kit (Illumina Inc.). Raw sequence data generated from Illumina NextSeq500 was de-multiplexed and converted into fastq files using Illumina's bcl2fastq software using default parameters. Read quality was assessed using FastQC [PMID: 2860544]. Reads were then aligned to human reference genome hg38 with STAR [PMID: 23104886]. Subsequently, gene-wise read counts were calculated using 'featureCounts' [PMID: 24227677], using hg38 gene annotation. The sequencing data were then normalized using RUVseq [PMID: 25150836] to correct for batch effects and other unwanted variations. Differentially expressed genes were identified using edgeR [PMID: 19910308]. Genes with false discovery rate adjusted p-value (FDR) less than 0.05 and $\log_2$ fold change greater than +/-1 were considered as significantly differentially expressed genes unless otherwise specified. All RNAseq data will be made publicly available through GeneLab (genelab.nasa.gov) and NCBI GEO (www.ncbi.nlm.nih.gov/geo/) prior to publication.

d. Quantitative real-time PCR

Quantitative real-time PCR (qPCR) was used to analyze the transcript expression level differences across irradiation groups on a selected panel of TP53-responsive and antioxidant-responsive transcripts. RNA extracted from cells was converted to cDNA prior to qPCR analysis.

Here, 2 µg of total RNA was converted to cDNA using the High-Capacity RNA-to-cDNA kit (Applied Biosystems) according to the manufacturer's instructions. cDNA was diluted 1:50 in 1X TE buffer and stored at -20°C in preparation for quantitative real-time PCR.

Each qPCR reaction used 5x TUFF TAQ QPCR Master Mix+Rox (Rebel Bioscience), TaqMan™ primers (Table 4.13), pre-amplified cDNA, and nuclease-free water for a total volume of 20 µL per reaction. Each transcript was analyzed in triplicate. Reactions were placed in a 7900HT Fast Real-Time PCR machine (Applied Biosystems). The following parameters were used: 95°C for 10 minutes, followed by 40 cycles of (95°C for 15 seconds, 60°C for 1 minute). The cycle threshold (Ct) values from the qPCR curves were extracted at the logarithmic growth phase of the curve. The delta-delta Ct methods was used to calculate the fold changes ($2^{-\Delta\Delta Ct}$). All groups containing DMSO were normalized to a SHAM+DMSO control. All groups that did not contain DMSO were normalized to a SHAM (no DMSO) control. GAPDH was used as the normalizer gene across all samples as has been previously demonstrated in other IR response studies as well as curcumin treated cells (14-16). We also verified in our dataset that GAPDH levels were not changing and could be used as an appropriate normalizer gene (data not shown). The $\log_2$ of the linear fold changes was calculated for comparisons.

Statistical Analysis

A p-value of 0.05 was used as a cutoff to determine statistical significance. P-values are labeled as <0.05 (*), <0.01 (**), <0.001 (***), and <0.0001 (****) throughout the manuscript unless otherwise specified. For RNA sequencing, differentially expressed genes were identified in comparison to SHAM controls using edgeR (see "RNA sequencing") and satisfied the following criteria: $\log_2$ fold change (+/-1), $p<0.05$, FDR<0.05. For DNA damage immunohistochemistry,

statistical analysis is One-way ANOVA with Dunnett's multiple comparisons test using GraphPad Prism software (all groups compared to SHAM (those without cNLP) or SHAM+cNLP (those with cNLP)). Induced foci counts/cell were calculated by subtracting the averaged foci counts for the SHAM values determined for curDMSO, cNLP, or DMSO alone control groups from the raw foci counts per treatment. Statistical analysis amongst foci counts at the 15-minute time point was determined by One-Way ANOVA with Turkey's multiple comparisons test (Gamma vs. Gamma+cNLP and Oxygen vs. Oxygen+cNLP). GraphPad Prism software and Biorender.com were used for figure illustrations.

4.4 Results

DNA double stranded break (DSB) foci induction was used to characterize the DNA damage response to different qualities of ionizing radiation

We measured the effect on the DNA damage response following IR exposures by quantifying DNA DSB-associated nuclear foci stained for gamma-H2AX/phospho-ser139 and 53BP1 (Figure 4.2a). At 15 minutes post-IR, all treatment groups resulted in peak DNA DSB associated gamma H2AX/53BP1 foci counts (Figure 4.3, Appendix Figure A.4.1, Appendix Table A.4.1). Here, 75 cGy GCR exposures had the highest average foci/cell count at 10.7, followed by 50 cGy protons (10.2 foci/cell) and then 50 cGy gamma (9 foci/cell) at the 15-minute time point. The highest-LET ion species (Fe-56 irradiated samples) resulted in the lowest average foci/cell, at roughly 6.6 total foci/cell and 3.6 foci/cell induced at the 15-minute time point (Table 4.2). When accounting for induced foci per cGy of exposure (Induced foci/cGy), protons and gamma-irradiated samples demonstrated the highest foci counts, at 0.142 and 0.118 induced foci/cGy, respectively. In addition, the highest-LET ion species Fe-56 demonstrated the least number of induced foci/cGy at

~0.071 (Table 4.2, Appendix Table A.4.2). Although the induction of DNA DSBs differed per IR quality, all IR species had peak DNA damage foci induction at the 15-minute time point and gradually reduced DNA damage foci expression over time, with proton, Fe-56, GCR, and O-16 irradiated groups returning to background levels of foci indistinguishable from SHAM groups by 24 hours after exposure (Figure 4.3, Figure A.4.1).

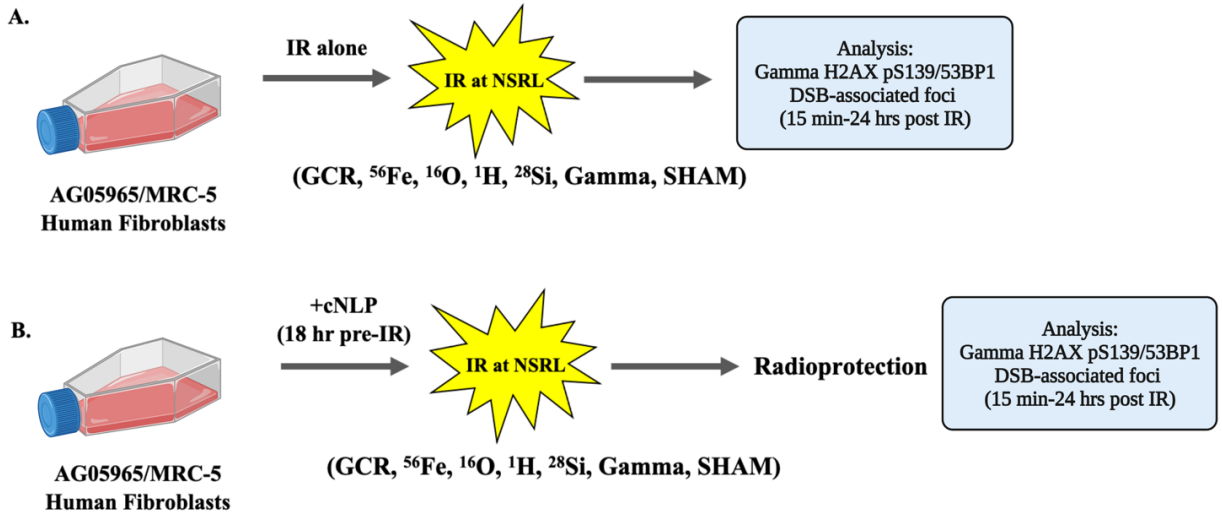

Figure 4.2: DNA damage study design. (a). Normal human MRC-5 fibroblasts were grown to confluency and irradiated with SimGCRSim (GCR), Fe-56, O-16, H-1 protons, Si-28, or gamma irradiation prior to DNA damage analysis. (b). Normal human MRC-5 fibroblasts were grown to confluency and pre-treated for 18 hours with cNLPs to analyze radioprotection following SimGCRSim (GCR), Fe-56, O-16, H-1 protons, Si-28, or gamma irradiation prior to DNA damage analysis.

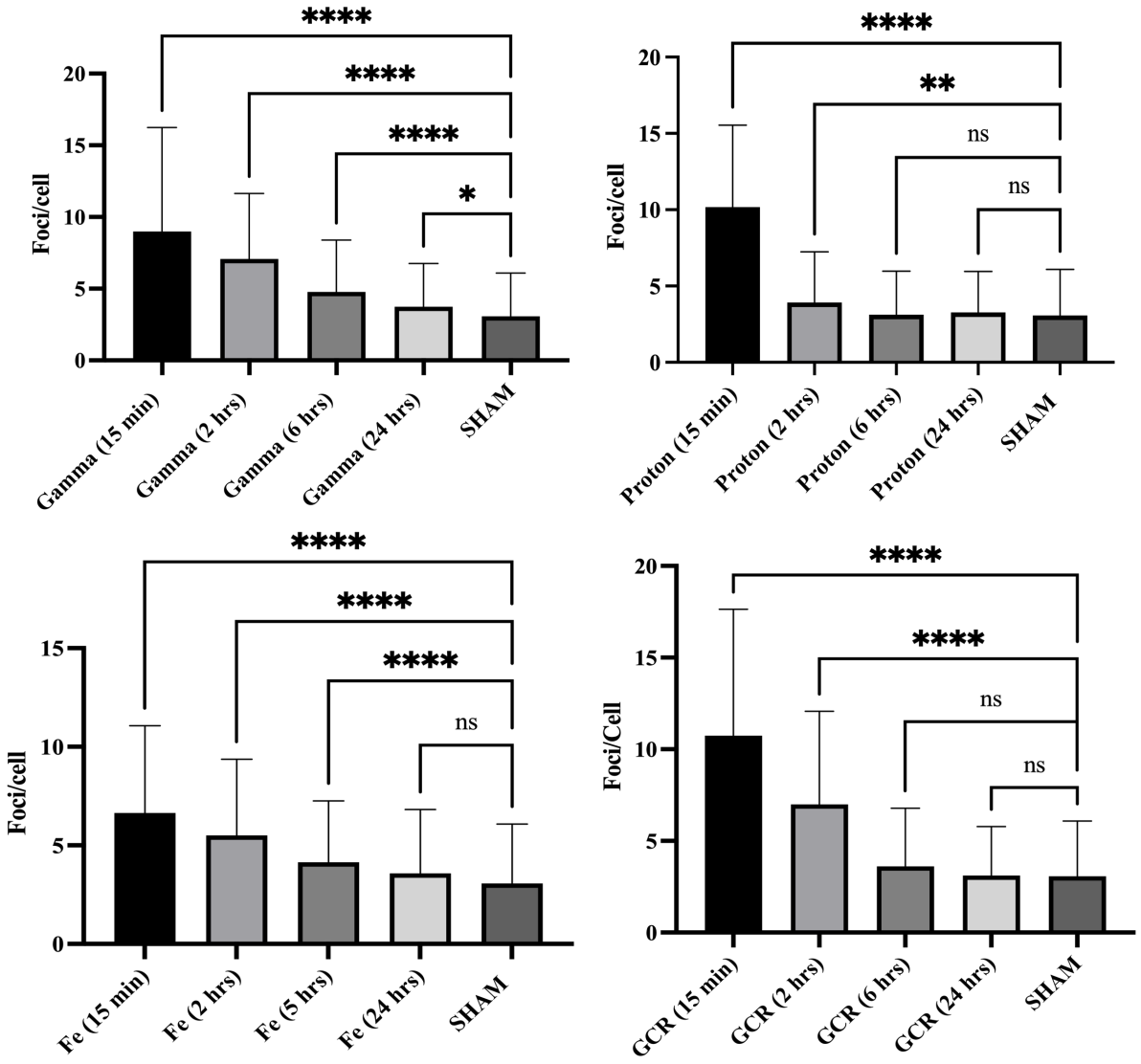

Figure 4.3: DNA damage foci counts when fixed 15 minutes-24 hours after ionizing radiation exposures. Shown are the gamma H2AX/53BP1 overlapping foci/cell averages with standard deviation. Doses of exposure are the following: Gamma (50 cGy), Proton (50 cGy), Fe-56 (50 cGy), and 5-ion SimGCRSim (GCR) (75 cGy). Analysis is One-way ANOVA with Dunnett's multiple comparisons test (all groups compared to SHAM). Foci counts for Si-28 and O-16 irradiations can be found in the Appendix (Figure A.4.1). Quantification of the foci counts in all IR groups can be found in the Appendix (Table A.4.1).

IR	Dose (cGy)	Time point	Average foci/cell	Induced foci/cell	Induced foci/cGy
SHAM	0	15 min/24 hrs	3.1		
GCR	75	15 min	10.7	7.7	0.102
Proton	50	15 min	10.2	7.1	0.142
Gamma	50	15 min	9	5.9	0.118
Fe	50	15 min	6.6	3.6	0.071

Table 4.2: Induced DNA DSB foci on human MRC-5 fibroblasts treated with IR-alone.

RNA sequencing analysis demonstrates the unique responses to different qualities of ionizing radiation

Six qualities of ionizing radiation with varying linear energy transfers (LET) (gamma rays, Si-28 particles, H-1 (proton) particles, O-16 particles, Fe-56 particles, and 5-ion simulated galactic cosmic radiation (GCR)) were applied to primary human MRC-5 fibroblasts and subjected to RNA sequencing analysis (Table 4.1, Figure 4.4a). Total up-regulated and down-regulated differentially expressed genes per IR species of interest compared to SHAM unirradiated control cells are shown (Table 4.3, Appendix Table A.4.3). GCR exposures had the most differentially expressed genes, with 559 up-regulated and 833 down-regulated genes over SHAM controls (Table 4.3). Interestingly, IR species with higher LETs, including Fe-56, Si-28, and O-16 had the least differentially expressed genes; 95, 103, and 64, respectively (Table 4.3, Appendix Table A.4.3). We then investigated total up- or down-regulated differentially expressed genes amongst gamma, proton, Fe-56, and GCR irradiated groups to identify uniquely differentially expressed genes as well as overlapping gene hits amongst these IR qualities (Figure 4.5). Gamma IR exposures demonstrated the least amount of uniquely expressed differential genes (20/125 or 16%), followed by Fe-56 (29/95 or 30.5%) and proton (129/328 or 39.3%). By far, GCR irradiated groups had the most uniquely differentially expressed genes compared to other IR species, with 1215/1392 or 87.3% of total differential gene hits unique to GCR groups. When looking at those differentially

expressed genes in common amongst IR groups, we found 30 overlapping differentially expressed genes across all IR types (Figure 4.5). Interestingly, differentially expressed genes within the gamma irradiated group demonstrated ~84% overlap (105/125 genes) with at least 1 other IR group, with the majority of overlapping differentially expressed genes coinciding with proton irradiated samples (78% or 98/125 genes). In Fe-56 irradiated samples, we found that 14/95 genes (14.7%) overlapped solely with GCR-irradiated groups whereas only 7 (7.3%) and 5 (5.3%) of genes overlapped with proton or gamma irradiated groups, respectively (Figure 4.5). Lastly, GCR-irradiated groups demonstrated the largest variability in gene hits compared to other IR species, with only 161/1392 (11.6%) of differentially expressed genes overlapping with proton samples, 69/1392 (5%) overlapping with gamma irradiated samples, and 46/1392 (3.3%) overlapping with Fe-56 irradiation groups (Figure 4.5).

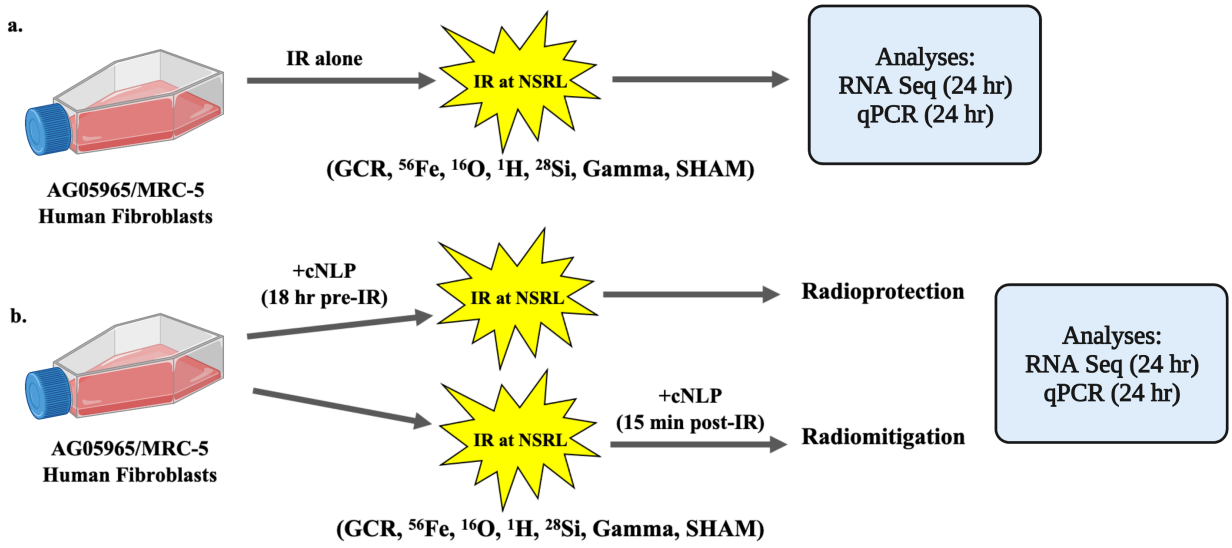

Figure 4.4: Transcriptomics study design. (a). Normal human MRC-5 fibroblasts were grown to confluency and irradiated with SimGCRSim (GCR), Fe-56, O-16, H-1 protons, Si-28, or gamma irradiation prior to differential gene expression analyses. (b). Normal human MRC-5 fibroblasts were grown to confluency and pre-treated for 18 hours with cNLPs to analyze radioprotection, or 15 minutes after IR to investigate radiomitigation following SimGCRSim (GCR), Fe-56, O-16, H-1 protons, Si-28, or gamma irradiations.

IR type	Dose (cGy)	Up-regulated DEG	Down-regulated DEG	Total DEG
Gamma	100	8	117	125
Proton	100	82	246	328
Fe	50	22	73	95
GCR	75	559	833	1392

Table 4.3: Total numbers of differentially expressed genes in irradiated samples as determined via RNA sequencing. *Note: The differentially expressed genes for Si-28 and O-16 irradiations can be found in the Appendix (Table A.4.3).*

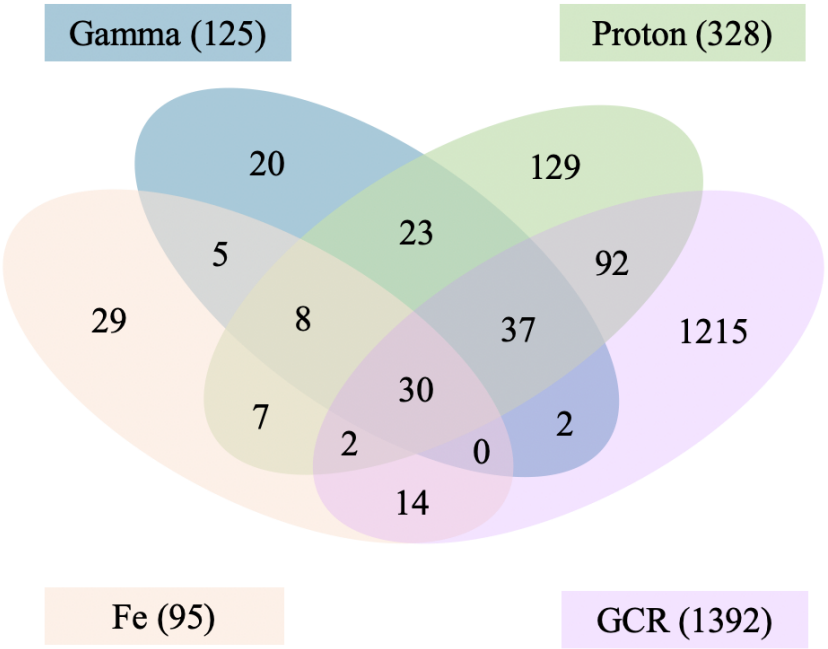

Figure 4.5: Overlapping differentially expressed genes amongst IR groups. Venn diagram of the differentially expressed genes amongst gamma, Fe-56, proton, and GCR irradiated groups. Gene hits were identified as either up-regulated or down-regulated within each IR group and satisfied the following criteria (log_2 fold change +/-1, $p<0.05$, FDR<0.05).

We then investigated the top up-regulated and down-regulated genes per IR quality of interest and their associated biological pathways using the GeneCards: The Human Gene Database (https://www.genecards.org/). Overall, the top differentially expressed genes in gamma irradiated cells were associated with immune signaling, stress, cell cycle arrest, and dysregulated mitosis (Table 4.4a). In proton irradiated samples, dysregulated neural trafficking, calcium signaling, Na+/K+ homeostasis, and metabolic processes predominated (Table 4.4b). Similar to proton IR, the top differentially expressed genes in high-LET Fe-56 samples revolved around neural trafficking and calcium signaling homeostasis. However, in contrast to other IR species, the top differentially expressed genes in Fe-56 samples also resulted in dysregulated hemoglobin function, oxygen transport, and muscle movement (Table 4.4c). In GCR-irradiated samples, the top 20 up-regulated genes had the strongest average differential expression out of all IR species tested, with an average $\log_2$ fold change of 9.6, and were involved the host-defense immune response, including phagocyte-mediated host-defense as well as serum complement pathways. GCR-irradiated groups also modulated a host of additional biological pathways, including p53, TGF-Beta, ERK, BMP signaling, and GPCRs (Table 4.4d). The lists of the top up-regulated and down-regulated genes and associated pathways for gamma, proton, Fe-56, and GCR-irradiated samples are listed in Tables 4.4(a-d).

Gamma Irradiation (100 cGy)				
Gene	**Log_2 Fold Change**	**P-Value**	**FDR**	**Biological Pathways**
FOS	1.31	4.70E-10	8.31E-08	Transcriptional regulation (Cell proliferation, differentiation, cell transformation)
RNU4-2	2.59	4.94E-05	4.26E-03	Unknown (snRNA)
FOSB	1.92	2.46E-11	5.27E-09	Transcriptional regulation (Cell proliferation, differentiation, cell transformation)
SNORA73B	1.43	6.96E-05	5.80E-03	Metabolism, oxidative stress, lipotoxicity[1]
MIR3648-1	2.35	2.20E-17	1.02E-14	Endoplasmic reticulum stress, Cell proliferation[2]
MIR3648-2	2.56	3.99E-17	1.68E-14	Endoplasmic reticulum stress, Cell proliferation[2]
MIR663A	3.25	1.28E-09	2.18E-07	Proliferation, TGF-Beta (negative regulator)
SSC4D	1.05	4.27E-04	2.65E-02	Innate and adaptive immunity, scavenger receptor activity
E2F2	-6.08	1.60E-07	2.32E-05	Cell cycle regulation, DNA replication
HGC6.3	-4.83	7.30E-04	4.10E-02	Increased in various cancers
CDC25C	-3.5	1.35E-13	3.71E-11	Cell cycle (Mitosis activator)
NUF2	-3.08	2.25E-28	3.58E-25	Chromosomal segregation
ERCC6L	-3.01	4.94E-13	1.33E-10	Cell cycle (mitosis)
SGO1	-2.94	1.87E-07	2.68E-05	Cell cycle (mitosis)
NEK2	-2.91	1.43E-22	1.14E-19	Cell cycle (mitosis)
NDC80	-2.68	8.81E-26	1.05E-22	Cell cycle (microtubule-kinetochore)
SPC25	-2.67	2.29E-10	4.20E-08	Cell cycle (microtubule-kinetochore)
KIF18B	-2.64	3.56E-17	1.59E-14	Cell cycle (Microtubule)
ASF1B	-2.53	4.06E-15	1.38E-12	Cell cycle (histone chaperone protein/chromatin)
DEPDC1	-2.51	1.45E-27	2.07E-24	DNA transcription (negative regulator)
BUB1B	-2.50	2.86E-20	1.71E-17	Cell cycle (spindle checkpoint function at kinetochore)
MKI67	-2.48	5.49E-32	3.67E-28	Dispersion of chromosomes in cytoplasm
UBE2C	-2.42	7.69E-32	3.67E-28	Ubiquitinylation (E2 ubiquitin conjugating enzyme)
KIF2C	-2.40	1.99E-22	1.43E-19	Cell cycle (microtubule)
CDK1	-2.40	5.21E-31	1.24E-27	Cell cycle regulation, DNA damage response
FAM111B	-2.39	3.51E-10	6.28E-08	DNA replication/peptidase (Ref: Uniprot)
ZNF367	-2.36	3.31E-05	3.08E-03	DNA transcription factor binding
CDC20	-2.31	1.07E-39	1.53E-35	Cell cycle regulation (nuclear movement, chromosome separation)

Table 4.4a: Top up-regulated and down-regulated genes based on gamma IR exposure and associated biological pathways. [1]Sletten, A.C et al. (2021). Loss of SNORA73 reprograms cellular metabolism and protects against steatohepatitis. *Nat Commun*. 12, 5214. https://doi.org/10.1038/s41467-021-25457-y.

[2]Rashid, F et al. (2017). Induction of miR-3648 Upon ER Stress and Its Regulatory Role in Cell Proliferation. *Int. J. Mol. Sci.*, 18, 1375. https://doi.org/10.3390/ijms18071375

Proton Irradiation (100 cGy)				
Gene	**Log_2 Fold Change**	**P-Value**	**FDR**	**Biological Pathways**
GPM6A	8.43	1.96E-17	2.18E-14	Neural differentiation/plasticity, Ca^{2+} channel signaling
ADGRV1	4.88	1.69E-03	2.18E-02	GPCR-hearing and vision
CAMK2B	4.21	1.56E-14	7.52E-12	Calcium signaling
MPO	4.19	1.32E-04	3.19E-03	Immunity, myeloid cells
OLFM1	4.15	1.34E-15	7.43E-13	Neural cell growth
NSG2	3.68	8.48E-04	1.30E-02	Neural trafficking
AC141424.1	3.66	8.14E-09	1.00E-06	lncRNA (unknown)
ATP1A3	3.63	1.29E-10	2.63E-08	Na+/K+ pump
TSPAN7	3.47	5.20E-08	5.08E-06	Cell growth, development
PDE2A	3.45	1.63E-05	6.17E-04	Calcium signaling
NAP1L2	3.20	1.91E-03	2.36E-02	Neural cell proliferation
RNU4-2	3.17	2.10E-07	1.75E-05	Unknown (snRNA)
MIR663A	2.63	1.50E-05	5.81E-04	Immune dysregulation[1]
HPCA	2.60	2.17E-03	2.57E-02	Neuron-specific calcium binding
GPM6B	2.54	3.67E-09	4.95E-07	Membrane trafficking, cell to cell communication (brain)
PLP1	2.50	6.62E-06	2.94E-04	Myelin sheath maintenance, axonal survival
ENPP4	2.34	2.19E-03	2.58E-02	Innate immunity (blood coagulation)
AGAP2	2.24	3.36E-08	3.63E-06	Anti-apoptosis of nerves, neural PI3K (activation)
GRIN2C	2.23	2.26E-03	2.64E-02	Learning, memory (NMDA receptor development)
RN7SL2	2.21	6.63E-05	1.83E-03	scRNA (unknown)
HGC6.3	-7.6	6.51E-05	1.81E-03	lncRNA (unknown)
KCNJ5	-5.64	6.35E-04	1.06E-02	K+ channel tetramer
TMEM74B	-5.62	1.63E-04	3.73E-03	Autophagy
CCL11	-5.08	6.36E-09	8.12E-07	Chemokine (Immune system and inflammation)
ACRBP	-5.06	1.15E-03	1.64E-02	Sperm and various cancers
LINC01909	-4.8	5.18E-03	4.70E-02	lncRNA (unknown)
MIR616	-4.46	1.95E-03	2.39E-02	Proliferation, expressed in cancers
LMO2	-3.77	5.76E-04	9.83E-03	Hematopoietic development and erythropoiesis
MIR641	-3.57	8.34E-04	1.29E-02	Bone/Chondrocyte growth
LNCOC1	-3.45	5.89E-04	1.00E-02	lncRNA (Ovarian cancer)
ESCO2	-3.42	1.82E-06	1.01E-04	Cell cycle (mitosis)
NEK2	-3.20	4.89E-17	4.15E-14	Cell cycle (mitosis)
ASPDH	-3.18	2.83E-03	3.09E-02	Oxidoreductase activity, aspartate dehydrogenase activity
ADH1C	-3.17	4.36E-08	4.50E-06	Metabolism (alcohol dehydrogenase)
SNORD14D	-2.94	2.36E-03	2.72E-02	snoRNA (unknown)
CENPA	-2.79	1.59E-11	4.10E-09	Cell cycle (centromere regulation)
BCL2A1	-2.74	1.57E-04	3.63E-03	Apoptosis (anti), Inflammation (NF-kB)
ADH1B	-2.72	3.92E-11	8.76E-09	Metabolism (alcohol dehydrogenase)

Proton Irradiation (100 cGy) (continued)				
Gene	**Log_2 Fold Change**	**P-Value**	**FDR**	**Biological Pathways**
SAPCD2	-2.65	1.80E-10	3.51E-08	Cell proliferation (positive regulator), protein localization to cortex (negative regulator)
HGFAC	-2.61	1.25E-03	1.74E-02	Hepatocyte growth factor activation

Table 4.4b: Top up-regulated and down-regulated genes based on proton IR exposure and associated biological pathways. [1]Geng et al. (2019). MicroRNA-663 induces immune dysregulation by inhibiting TGF-β1 production in bone marrow-derived mesenchymal stem cells in patients with systemic lupus erythematosus. *Cell Mol Immunol*.;16(3):260-274. doi: 10.1038/cmi.2018.1.

Fe-56 Irradiation (50 cGy)				
Gene	**Log_2 Fold Change**	**P-Value**	**FDR**	**Biological Pathways**
GPM6A	7.84	4.27E-20	6.14E-16	Neural differentiation and plasticity, Calcium channel signaling
CAMK2B	5.89	4.63E-09	1.96E-06	Calcium/calmodulin binding
KIF1A	4.92	1.75E-10	1.18E-07	Organelle transport across microtubules
NSG2	4.44	1.21E-05	2.14E-03	Neural development
SLC17A7	3.75	1.94E-10	1.21E-07	Na/Pi transporter in brain (glutamate transport)
NAP1L2	3.63	2.47E-04	2.24E-02	Neural cell proliferation
SLC8A2	3.61	2.02E-04	1.97E-02	Calcium signaling
ATP1A3	3.37	1.44E-04	1.51E-02	Na+/K+ pump
SPOCK2	3.34	2.32E-08	8.79E-06	Calcium and ECM binding
CHD5	2.8	1.29E-05	2.21E-03	DNA binding
DLGAP3	2.79	8.78E-07	2.26E-04	Neurotransmitter receptor activity (postsynaptic)
TAGLN3	2.28	1.00E-04	1.15E-02	CNS development
KIF5C	2.15	9.03E-05	1.07E-02	CNS cargo transport
SCN1A	2.02	8.17E-05	1.00E-02	Voltage-gated Na+ channels (brain)
FOSB	1.92	1.11E-08	4.42E-06	Transcriptional regulation (Cell proliferation, differentiation, cell transformation)
SULT4A1	1.79	9.23E-05	1.08E-02	Neurotransmitter metabolism
DDN	1.70	3.60E-06	7.61E-04	Transcription factor activity (RNA polymerase II)
AGAP2	1.65	6.19E-06	1.20E-03	Anti-apoptosis of nerves, neural PI3K (activation)
NRXN1	1.65	7.07E-04	4.96E-02	Calcium-dependent neural synapse regulation (CNS)
EBI3	1.44	1.30E-05	2.21E-03	Inflammatory response (IL27), JAK/STAT pathway
HBB	-5.21	1.35E-07	4.35E-05	Hemoglobin, oxygen transport
TNNT3	-4.98	2.46E-11	3.22E-08	Troponin synthesis (muscle contraction)
CP	-4.88	1.28E-05	2.21E-03	Fe movement through blood and organs
HBA2	-4.63	1.45E-09	7.51E-07	Hemoglobin, oxygen transport
HBA1	-4.6	1.46E-09	7.51E-07	Hemoglobin, oxygen transport
MYL1	-4.22	4.14E-11	4.25E-08	Calcium ion binding for muscle

Fe-56 Irradiation (50 cGy) (continued)				
Gene	**Log_2 Fold Change**	**P-Value**	**FDR**	**Biological Pathways**
AMPD1	-4.16	2.85E-04	2.51E-02	Muscle movement
CKM	-3.95	1.92E-09	9.22E-07	Energy homeostasis (heart, muscle)
MYH1	-3.78	1.67E-13	4.81E-10	Myosin (muscle contraction)
MYH8	-3.65	1.07E-11	1.71E-08	Myosin (muscle contraction) and actin filament binding
MYH4	-3.59	5.69E-11	4.90E-08	Actin binding, ATP hydrolysis, muscle contraction, RNA binding
PTPRC	-3.45	1.14E-04	1.28E-02	B and T cell signaling, cytokine signaling
HGC6.3	-3.44	2.37E-04	2.18E-02	lncRNA (unknown)
MYLPF	-3.36	3.64E-10	2.12E-07	Calcium ion binding, skeletal muscle development
MYH2	-3.35	5.91E-06	1.19E-03	Skeletal muscle contraction
MYBPC2	-3.29	1.56E-06	3.71E-04	Myosin binding (heart)
TNNI2	-2.68	1.28E-05	2.21E-03	Calcium-dependent muscle contraction
EVI2B	-2.56	2.54E-04	2.28E-02	Hematopoiesis (granulocyte differentiation)
CYYR1-AS1	-2.32	4.65E-05	6.30E-03	lncRNA (unknown)
KIF18B	-2.03	3.57E-11	4.25E-08	Cell cycle (Microtubule)

Table 4.4c: Top up-regulated and down-regulated genes based on Fe-56 exposure and associated biological pathways.

GCR Irradiation (75 cGy)				
Gene	**Log_2 Fold Change**	**P-Value**	**FDR**	**Biological Pathways**
DEFA1	29.94	9.34E-55	3.66E-52	Phagocyte-mediated host defense
DEFA1B	29.94	9.34E-55	3.66E-52	Phagocyte-mediated host defense, Innate Immune system
DEFA3	28.86	8.27E-53	3.00E-50	Phagocyte-mediated host defense, Innate Immune system
SASH3	10.1	1.12E-07	7.96E-07	Cell signaling (lymphocytes)
C1QC	8.92	1.43E-07	9.97E-07	Serum complement pathway
C1QB	8.55	1.46E-07	1.02E-06	Serum complement pathway
LTF	8.39	6.27E-05	2.55E-04	Non-specific immunity (transferrin), cell growth, differentiation
PIK3R5	8.03	4.09E-04	1.38E-03	Neuropathic pain signaling, DNA damage response (ATM), cell growth, cell proliferation
GPR183	6.44	1.23E-34	1.56E-32	GPCR signaling (B lymphocytes), peptide ligand-binding receptors
S100A9	5.94	8.38E-23	4.33E-21	Calcium signaling, Inflammation (TLR4), Immune Signaling
PCDH1	5.36	2.30E-174	1.67E-170	Neural cell adhesion, neural development
LINC00862	5.12	9.49E-11	1.13E-09	lncRNA (unknown)

GCR Irradiation (75 cGy) (continued)				
Gene	**Log_2 Fold Change**	**P-Value**	**FDR**	**Biological Pathways**
AC141424.1	5.05	7.41E-13	1.23E-11	lincRNA (unknown)
PDGFB	4.91	3.58E-124	1.30E-120	Platelet derived growth factor (cell proliferation, cell migration, survival and chemotaxis)
ZNF385B	4.83	1.38E-16	3.80E-15	p53 binding and p53 induced intrinsic apoptosis
DCSTAMP	4.75	9.71E-19	3.39E-17	Dendritic cell immunity and bone homeostasis
S100A8	4.58	3.53E-09	3.24E-08	Inflammatory process (pro) and immune response activator
ELN	4.54	2.79E-20	1.11E-18	Organ elasticity, Phospholipase C pathway
SALRNA2	4.39	3.16E-09	2.92E-08	lncRNA (unknown)
SLCO5A1	4.30	4.25E-12	6.32E-11	Transporter activity (solute carrier organic anion transporter)
OR11H2	-5.43	1.82E-02	3.85E-02	GPCR signaling (olfactory)
LINC01497	-5.08	1.61E-04	5.97E-04	lncRNA (unknown)
CYYR1-AS1	-4.83	1.15E-04	4.41E-04	lncRNA (unknown)
BCL2A1	-3.92	9.31E-10	9.45E-09	Apoptosis (anti), Inflammation (NF-kB)
IFIT1	-3.81	3.46E-32	3.78E-30	Interferon signaling
TNFSF10	-3.71	8.58E-13	1.41E-11	TNF receptor binding, TGF-Beta signaling, ERK signaling
NR0B1	-3.62	1.07E-04	4.13E-04	Gene transcription (Retinoic acid receptor)
SLC51B	-3.6	3.86E-09	3.52E-08	Drug Induction of Bile Acid
SLC7A14	-3.39	1.84E-17	5.50E-16	Cationic amino acid transport
HCAR2	-3.38	4.68E-05	1.96E-04	GPCR signaling, Peptide ligand-binding receptors
LCNL1	-3.38	2.81E-09	2.60E-08	Small molecule binding
AC061992.2	-3.32	8.85E-05	3.47E-04	lncRNA (unknown)
NPTX1	-3.31	1.86E-24	1.13E-22	Neural synapse regulation
CLDN11	-3.31	1.75E-64	1.01E-61	Cell polarity, signal transduction, oligodendrocyte proliferation/migration
TMEM100	-3.31	2.96E-06	1.59E-05	Bone Morphogenic Protein (BMP) signaling pathway
KCNJ2	-3.26	1.33E-49	4.02E-47	K+ channel modulator (neural and muscle tissues)
HCAR3	-3.13	4.63E-03	1.19E-02	GPCR signaling (cell junctions)
HKDC1	-3.00	3.30E-06	1.76E-05	Glucose metabolism
MYCBPAP	-2.99	1.71E-07	1.18E-06	Spermatogenesis
SLITRK5	-2.91	1.49E-25	1.00E-23	Neural tissue modulation

Table 4.4d: Top up-regulated and down-regulated genes based on GCR exposure and associated biological pathways.

The DAVID NCBI database (https://david.ncifcrf.gov/) was then applied to investigate gene ontology (GO) analysis and functional annotation clustering on the total numbers of up- and down-regulated differentially expressed genes in gamma, proton, Fe-56, and GCR-irradiated samples (Table 4.5a-b). Similarities amongst all IR exposures included dysregulated microtubule activity associated with increased cell cycle arrest as well as modulated protein kinase activity (Table 4.5a). We also found overlapping biological functions involved in ubiquitin regulation, metabolism, hemoglobin transport, and muscle contraction amongst two or more IR species (Table 4.5a). GO clusters also identified unique biological processes based on IR quality. For example, DNA damage checkpoint functions (gamma IR), cAMP signaling (proton IR), nitric oxide transport and oxygen binding (Fe-56 IR), as well as multiple GCR-specific responses involving immune regulation, lipid homeostasis, and downstream receptor tyrosine kinase signaling cascades predominated (Table 4.5b). In accordance with the increased numbers of differentially expressed genes found in the GCR-irradiated cells, we found that GCR exposures also associated with the greatest variety of biological functions and processes (Table 4.5b).

Shared Gene Ontology (GO) processes and functions
Microtubule motor activity (Gamma, Proton, Fe-56, GCR)
Mitotic cell cycle phase transition and cell cycle checkpoints (Gamma, Proton, Fe-56)
Ubiquitin regulation (Gamma, Proton)
Protein kinase activity (Gamma, Proton, Fe-56, GCR)
Mitotic spindle organization (chromosome stability and segregation) (Proton, Fe-56, GCR)
Muscle contraction (Fe-56 and GCR)
Metabolic processes (proton, GCR)
Hemoglobin binding (Fe-56, GCR)

Table 4.5a: Shared Gene Ontology (GO) functions associated with differentially expressed genes following various qualities of IR exposures.

Unique Gene Ontology (GO) processes and functions
Gamma: DNA replication checkpoints, DNA damage response, Drug/xenobiotic stimuli response
Proton: cAMP mediated signaling, Endothelial proliferation, Vascular muscle cell proliferation, Chemokine activity
Fe-56: Nitric oxide transport, Oxygen binding/transport
GCR: Integrin signaling, Transmembrane receptor signaling, Deamination of cytosine/cytidine/deoxycytidine, Muscle contraction (cardiac) and motor activity, Cardiac cell morphogenesis and ETM transition, Cholesterol homeostasis, Lipid transport activity, Immune response (chemotaxis), Steroid metabolism, Dehydrogenase (NAD+) activity, oxidoreductase activity, SMAD protein phosphorylation/signal transduction, BMP signaling , Ephrin signaling (RTKs), GPCR activity, Cell defense to bacteria, fungi, JAK/STAT cascade pathway, IL7 signaling

Table 4.5b: Unique Gene Ontology (GO) functions associated with differentially expressed genes following various qualities of IR exposures.

Curcumin NLPs administered as a radioprotectant do not consistently alter DNA damage foci induction

Following IR-alone exposures, we next sought to investigate whether curcumin NLPs may alter the DNA DSB associated nuclear foci or transcriptomic findings when administered as a radiation protection agent (Figure 4.2b, Figure 4.4b). First, we tested the effects of cNLPs as radiation protectants on DNA DSBs (Figure 4.2b). Similar to IR alone groups, at 15 minutes post-IR, all groups treated with cNLP radioprotection resulted in peak DNA DSB associated gamma H2AX/53BP1 foci counts (Figure 4.6, Appendix Figure A.4.2). At the 15-minute fixation time point, GCR+cNLP samples had the highest mean foci/cell (average foci/cell=11.5), and Fe-56+cNLP samples had the lowest mean foci/cell (average foci/cell=5.9). The mean foci/cell

averages in IR+cNLP radioprotective groups from 15 minutes to 24 hours after exposure can be found in the Appendix (Table A.4.4). When accounting for the differences in induced foci/cell averages, gamma+cNLP and O-16+cNLP treatments were the only IR groups that had statistically significant differences at the 15-minute time point compared to IR alone controls (Table 4.6, Table A.4.5), however, these decreases in DNA DSBs were not consistent across all fixation time points. In addition, we found that the proton+cNLP group had the highest induced foci/cGy (0.132), followed by GCR+cNLP (0.112) (Table 4.6, Table A.4.5). Similar to IR alone, the high-LET Fe-56+cNLP group had the lowest average induced foci count/cGy, at 0.056 (Table 4.6).

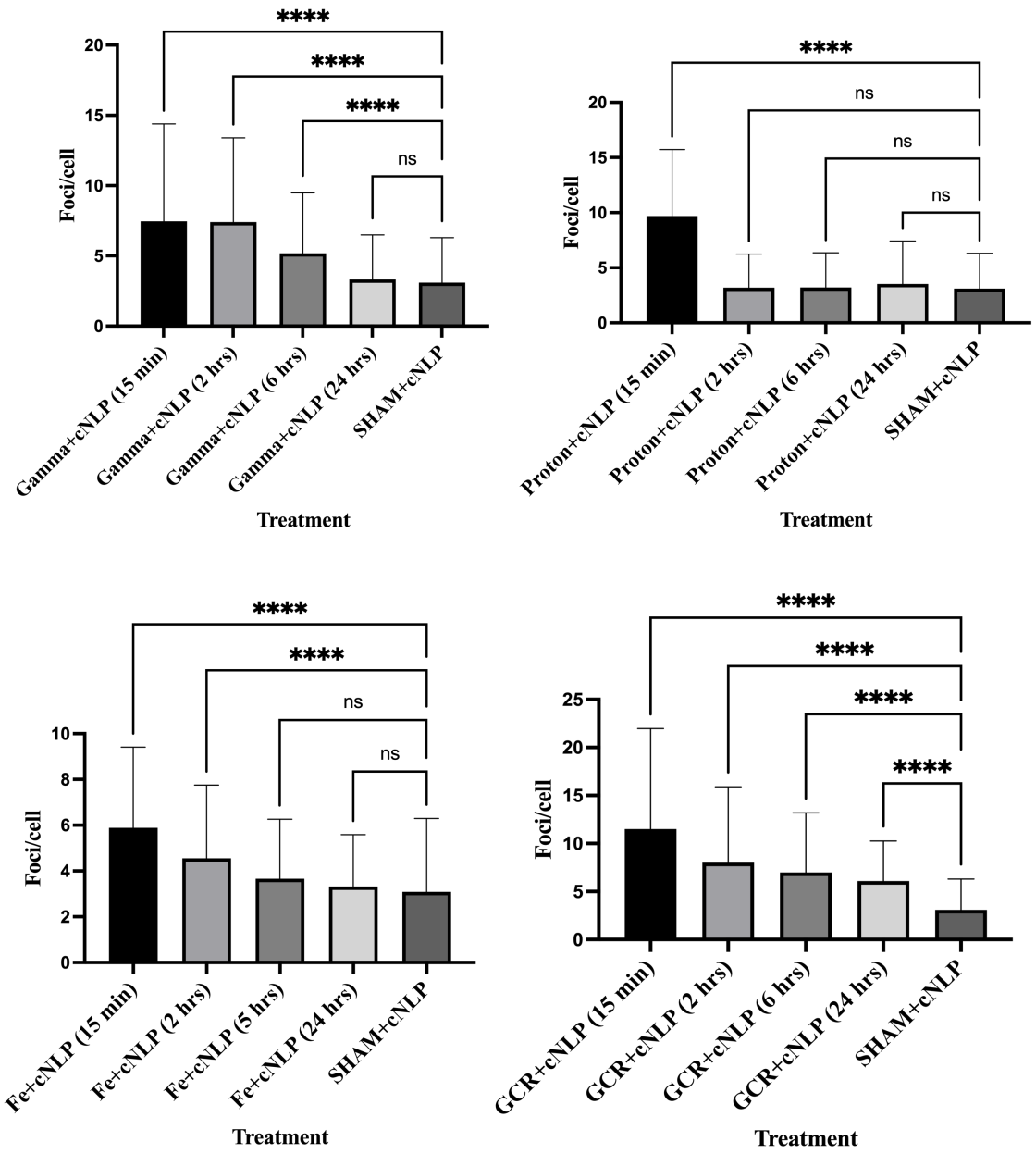

Figure 4.6: DNA damage foci counts on cNLP pre-treated cells when fixed at 15 minutes-24 hours after ionizing radiation exposures. Shown are the average foci/cell with standard deviation. Doses of exposure are the following: Gamma+cNLP (50 cGy), Proton+cNLP (50 cGy), Fe-56+cNLP (50 cGy), and 5-ion SimGCRSim+cNLP (GCR+cNLP) (75 cGy). Analysis is One-way ANOVA with Dunnett's multiple comparisons test (all groups compared to SHAM+cNLP control). Foci counts for Si-28+cNLP and O-16+cNLP treatments can be found in the Appendix (Figure A.4.2). Quantification of the foci counts in all IR groups+cNLP can be found in the Appendix (Table A.4.4).

Treatment	Dose (cGy)	Time point	Average foci/cell	Induced foci/cell	Induced foci/cGy
Gamma	50	15 min	9	5.9	0.118
Gamma+cNLP	50	15 min	7.5*	4.4	0.087
Proton	50	15 min	10.2	7.1	0.142
Proton+cNLP	50	15 min	9.7	6.6	0.132
Fe	50	15 min	6.6	3.6	0.071
Fe+cNLP	50	15 min	5.9	2.8	0.056
GCR	75	15 min	10.7	7.7	0.102
GCR+cNLP	75	15 min	11.5	8.4	0.112

Table 4.6: Comparison of DNA DSB foci kinetics on human MRC-5 fibroblasts treated with IR alone or IR+cNLP radiation protection treatment. **Note: Gamma+cNLP foci induction was significantly different than Gamma IR alone at the 15-minute time point as determined by One-Way ANOVA with Turkey's multiple comparisons test ($p<0.001$).*

Curcumin NLPs administered as a radioprotectant altered DEGs and pathways based on RNA sequencing analysis

We next sought to investigate if curcumin NLPs (cNLPs) administered as a radioprotective agent may alter the DEG and downstream biological pathways following simulated space radiation exposures. We administered cNLPs to human MRC-5 fibroblasts approximately 18 hours before exposure to gamma rays, simulated GCR, or corresponding single-ion IR species (Figure 4.4b). Total numbers of differentially expressed genes across groups were determined via RNA sequencing and can be found in the Appendix (Table A.4.6).

We first examined the effect of cNLP radioprotection on gamma IR exposures. Overall, there were 8 up-regulated/117 down-regulated genes in the gamma IR alone group and 69 up-regulated/161 down-regulated genes in the gamma+cNLP radioprotective group (Figure 4.7). When comparing gamma IR alone to gamma IR+cNLP, we found 0 overlapping up-regulated genes and 94 overlapping down-regulated genes. We also identified 69 up-regulated and 67 down-regulated genes in the gamma+cNLP groups that were not similarly differentially expressed in the

gamma IR alone control group (Figure 4.7). Interestingly, FOS and RNU-4 were both up-regulated in gamma IR alone (log_2 fold change of 1.3 and 2.5, respectively) and down-regulated in gamma+cNLP (log_2 fold change -1.5 and -12.5, respectively). We then utilized the DAVID NCBI database to investigate the impact of differentially expressed genes on downstream biological pathways between gamma or gamma+cNLP radioprotective groups (Table 4.7). We ran total up-regulated and down-regulated genes hits for each treatment and then concatenated the findings for gamma IR alone or gamma+cNLP pathway analysis. Overall, we found 5 shared biological pathways between gamma alone and gamma+cNLP treatments, including cell cycle and p53 signaling modulation. We also discovered unique biological pathways in the gamma IR alone group that were not impacted in the gamma+cNLP radioprotection group, including various cancer and DNA damage repair pathways. We did not identify any unique biological pathways in the gamma+cNLP group that were not also impacted by gamma IR alone (Table 4.7).

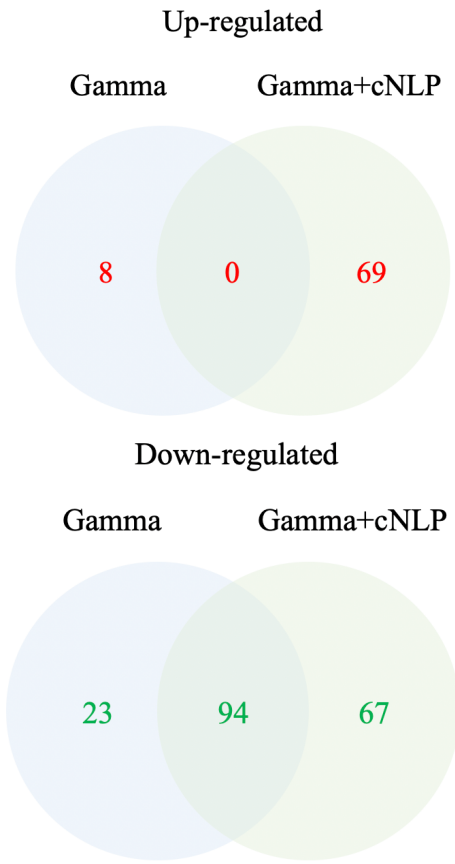

Gamma Irradiation (100 cGy) + cNLP Radioprotection			
Gene	**Log_2 Fold Change**	**P-Value**	**FDR**
SNORD43	7.95	9.16E-04	1.24E-02
ENAM	2.40	3.77E-03	3.51E-02
KCNN4	2.27	1.12E-03	1.44E-02
RNF224	2.21	3.63E-03	3.44E-02
CCDC65	1.90	2.39E-05	7.32E-04
TNIP3	1.80	1.11E-03	1.43E-02
TIAF1	1.72	3.93E-03	3.63E-02
GCSAM	1.71	1.21E-05	4.29E-04
EFCAB6	1.71	2.58E-04	4.78E-03
PEAK3	1.71	5.81E-03	4.78E-02
MIR186	-13.97	2.38E-05	7.32E-04
RNU4-2	-12.58	2.52E-05	7.70E-04
E2F2	-9.84	1.97E-08	1.70E-06
POU2F3	-9.77	2.58E-04	4.78E-03
SYNE4	-8.27	4.85E-03	4.24E-02
MYH13	-7.04	3.62E-03	3.43E-02
MEOX2	-6.03	1.57E-03	1.87E-02
DLGAP5	-5.65	2.42E-29	8.66E-26
CNTNAP2	-5.62	1.03E-04	2.37E-03
CENPA	-5.31	1.92E-13	5.39E-11

Figure 4.7: Differentially expressed genes in gamma irradiated groups with and without cNLP radioprotection treatment. Left: Venn diagrams show the differentially expressed genes via RNA sequencing analysis in MRC-5 cells exposed to 100 cGy gamma rays with and without cNLP radioprotection. Right: The top differentially expressed genes in gamma+cNLP radiation protection treatment. Up-regulated genes are in red and down-regulated genes are in green. Differentially expressed genes satisfied the following criteria: log2 fold change (+/-1), $p<0.05$, FDR<0.05.

Biological pathway	Gamma alone	Gamma+cNLP	Differentially Expressed Genes
hsa04110:Cell cycle	✓	✓	PLK1, BUB1B, TTK, CDC6, PKMYT1, CDC25C, CCNA2, CDC20, CCNB2, CCNB1, CDC45, ORC1, CCNE2, E2F1, CDK1, E2F2, BUB1, MAD2L1
hsa04114:Oocyte meiosis	✓	✓	SGO1, CDC20, CCNB2, CCNB1, CCNE2, PLK1, CAMK2A, CDK1, PKMYT1, CDC25C, BUB1, MAD2L1
hsa04914:Progesterone-mediated oocyte maturation	✓	✓	CCNA2, CCNB2, CCNB1, PLK1, CDK1, PKMYT1, CDC25C, BUB1, MAD2L1
hsa04115:p53 signaling pathway	✓	✓	CCNB2, CCNB1, RRM2, CCNE2, CDK1, GTSE1
hsa05161:Hepatitis B	✓	✓	CCNA2, CCNE2, E2F1, BIRC5, E2F2, FOS
hsa03460:Fanconi anemia pathway	✓		BLM, RAD51, EME1, FANCD2, FANCA
hsa03440:Homologous recombination	✓		BLM, RAD51, EME1
hsa05206:MicroRNAs in cancer	✓		CCNE2, CDCA5, E2F1, E2F2, KIF23, CDC25C
hsa05170:Human immunodeficiency virus 1 infection	✓		CCNB2, CCNB1, CDK1, FOS, CDC25C
hsa04068:FoxO signaling pathway	✓		PLK4, CCNB2, CCNB1, PLK1
hsa05200:Pathways in cancer	✓		CCNA2, RAD51, CCNE2, E2F1, BIRC5, E2F2, FOS
hsa05212:Pancreatic cancer	✓		RAD51, E2F1, E2F2
hsa05222:Small cell lung cancer	✓		CCNE2, E2F1, E2F2
hsa05169:Epstein-Barr virus infection	✓		CCNA2, CCNE2, E2F1, E2F2
hsa05203:Viral carcinogenesis	✓		CCNA2, CDC20, CCNE2, CDK1
hsa05215:Prostate cancer	✓		CCNE2, E2F1, E2F2
hsa01522:Endocrine resistance	✓		E2F1, E2F2, FOS
hsa05207:Chemical carcinogenesis - receptor activation	✓		E2F1, BIRC5, FOS, CDC6
hsa04218:Cellular senescence	✓		CCNA2, CCNB2, CCNB1, CCNE2, CDK1, E2F1, E2F2, MYBL2, FOXM1
hsa05166:Human T-cell leukemia virus 1 infection	✓		CCNA2, CDC20, CCNB2, CCNE2, E2F1, BUB1B, E2F2, FOS, MAD2L1

Table 4.7: Biological pathways impacted by gamma IR alone or gamma+cNLP radioprotection treatment.

Note: Differentially expressed gene hits per pathway are colored as follows: Black-colored genes (differentially expressed in both treatment group pathways), orange-colored genes (differentially expressed in the pathways involving in cNLP radioprotection group only), blue-colored genes (differentially expressed in the pathways involving gamma alone group only). All pathway hits had p-values <0.1.

We next investigated the effect of cNLP radioprotective treatment on exposures relevant to deep space missions. Differentially expressed genes from GCR exposed samples were run in the DAVID NCBI database to explore relevant biological pathways impacted through either GCR alone or GCR+cNLP radioprotective groups. Overall, there were 559 up-regulated/833 down-regulated genes in the GCR alone group and 429 up-regulated/478 down-regulated genes in the

GCR+cNLP radioprotective group (Figure 4.8). We also identified 110 uniquely up-regulated and 149 uniquely down-regulated genes in the GCR+cNLP group. There were 18 overlapping biological pathways of interest between GCR and GCR+cNLP groups, including cell cycle effects, immune cascades, FoxO signaling, ECM receptor interactions, PI3K-Akt signaling, and Rap1 signaling (Table 4.8). We also found 17 additional biological pathways of interest relevant to GCR+cNLP that did not overlap with GCR alone. These unique pathways impacted meiosis, microRNA regulation, ABC transporter function, immune regulation, as well as metabolism (Appendix Table A.4.7).

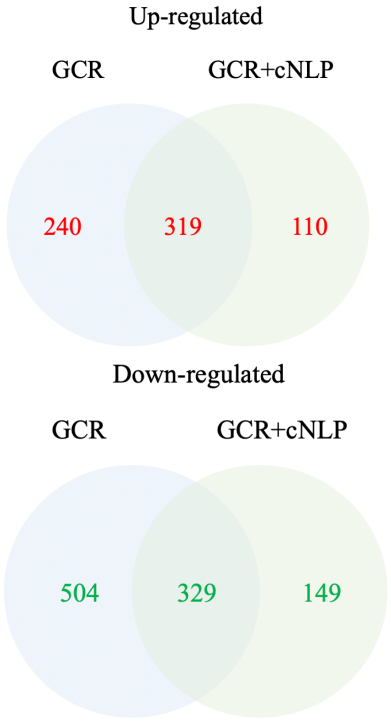

GCR Irradiation (75 cGy) + cNLP Radioprotection			
Gene	**Log_2 Fold Change**	**P-Value**	**FDR**
DEFA1	21.47	2.18E-22	1.63E-20
DEFA1B	21.47	2.18E-22	1.63E-20
DEFA3	19.81	7.26E-22	5.06E-20
C1QB	7.63	4.79E-13	1.35E-11
PIK3R5	7.21	6.55E-04	3.02E-03
C1QC	6.70	3.56E-03	1.28E-02
LTF	6.53	1.18E-03	5.03E-03
SALRNA2	4.92	1.45E-11	3.33E-10
DCSTAMP	4.82	1.29E-18	6.05E-17
GPR183	4.75	4.45E-12	1.10E-10
CCL7	-3.91	3.33E-15	1.17E-13
NR0B1	-3.90	5.64E-06	4.59E-05
KIF20A	-3.77	8.70E-50	5.26E-47
DLGAP5	-3.77	2.99E-57	2.71E-54
TNFSF10	-3.63	5.97E-15	2.04E-13
CEMIP	-3.61	8.16E-36	1.72E-33
CCL11	-3.59	1.94E-20	1.11E-18
NPTX1	-3.58	2.11E-27	2.34E-25
SPC25	-3.54	6.47E-23	5.13E-21
SLC7A14	-3.45	1.13E-17	4.90E-16

Figure 4.8: Differentially expressed genes in GCR irradiated groups with and without cNLP radioprotection treatment. Left: Venn diagrams show differentially expressed genes via RNA sequencing analysis in MRC-5 cells exposed to 75 cGy 5-ion simulated GCR exposures with and without cNLP radioprotection. Right: Top differentially expressed genes in GCR+cNLP radiation protection treatment. Up-regulated genes are in red and down-regulated genes are in green. Differentially expressed genes satisfied the following criteria: log2 fold change (+/-1), $p<0.05$, FDR<0.05.

Biological pathway	GCR alone	GCR+cNLP	Differentially Expressed Genes
hsa04110:Cell cycle	✓	✓	TGFB2, CDKN2B, GADD45B, MCM7, PLK1, BUB1B, TTK, CDC7, CHEK2, CDC6, PKMYT1, CDC25C, CCNA2, CDC20, CCNB2, CCNB1, CDC45, PTTG1, E2F1, CDK1, E2F2, BUB1, MAD2L1
hsa04068:FoxO signaling pathway	✓	✓	PLK4, TGFB2, CDKN2B, PRKAA2, GADD45B, PLK2, BNIP3, PLK1, IRS2, SLC2A4, IGF1, FOXO1, KLF2, IL6, SOD2, FBXO32, PIK3R5, CCNB2, CCNB1, BCL2L11, TNFSF10, IL7R
hsa04512:ECM-receptor interaction	✓	✓	TNXB, VWF, ITGB3, ITGB4, ITGA2, ITGA4, ITGA3, ITGA1, TNC, HMMR, THBS1, THBS4, COL1A1, COMP, VTN, COL2A1, COL4A1, COL4A2, ITGAV, CD36, CHAD, SPP1, ITGA7, ITGA9
hsa04510:Focal adhesion	✓	✓	SHC4, SHC2, TNXB, FLT1, VWF, CAV2, ITGB3, FLT4, ITGA2, ITGA1, PDGFB, IGF1, THBS1, PIK3R5, MYLPF, COMP, COL2A1, COL4A1, CHAD, SPP1, ITGA7, ITGB4, TNC, THBS4, VTN, ITGAV, VASP, ITGA4, CAV2, ITGA3, COL1A1, COL4A2, ITGA9
hsa04060:Cytokine-cytokine receptor interaction	✓	✓	TNFSF18, CSF1R, TGFB2, CCL11, CXCL8, CSF2, TNFRSF12A, LIF, INHBA, TNFRSF1B, GDF5, CXCL2, BMP7, GHR, CXCL12, CCL7, TNFSF4, TNFSF10, IL21R, CCL2, IL12A, IL7R, IL17B, IL20, IL1RAP, CX3CL1, IL6R, IL11, IL34, TNFRSF19, GDF6, PRLR, BMP5, BMP4, BMP2, IL6, INHA, CCL26
hsa05144:Malaria	✓	✓	COMP, TGFB2, CXCL8, ITGB2, TLR9, HBB, CCL2, IL12A, THBS1, IL6, CD36, THBS4
hsa05414:Dilated cardiomyopathy	✓	✓	TGFB2, ACTC1, TNNT2, ITGA2, ITGB3, TPM1, ITGA1, ADCY4, ITGA7, DMD, IGF1, ITGA4, ITGB4, ITGA3, SLC8A1, SGCD, ITGAV, MYH6, CACNG4, ITGA9, MYH7
hsa05205:Proteoglycans in cancer	✓	✓	CAMK2B, TGFB2, WNT2B, CAV2, ITGB3, WNT7B, ITGA2, FZD8, IGF1, THBS1, PIK3R5, TFAP4, WNT11, ERBB3, PLAU, TIMP3, HCLS1, PTPN6, ITPR3, VTN, ITGAV, WNT7B, WNT5A, PLAUR, IGF2, MSN, MIR21, ANK2, COL1A1, HBEGF
hsa04151:PI3K-Akt signaling pathway	✓	✓	CHRM2, CSF1R, FLT1, TNXB, PRKAA2, FLT4, ITGB3, PDGFB, THBS1, PIK3R5, GHR, COMP, BCL2L11, CHAD, SPP1, VWF, ITGA2, ITGA1, IGF1, FGF17, COL2A1, COL4A1, KIT, ITGA7, IL7R, FGF11, ITGB4, TNC, FGF1, EFNA5, AREG, THBS4, VTN, ERBB3, ITGAV, IL6R, ANGPT2, ITGA4, ITGA3, IGF2, PRLR, EREG, COL1A1, NR4A1, IL6, COL4A2, FGFR4, ITGA9
hsa05200:Pathways in cancer	✓	✓	CSF1R, CXCL8, WNT2B, ADCY4, PDGFB, GLI1, CKS1B, PIK3R5, RASGRP3, WNT11, E2F1, E2F2, NKX3-1, TGFB2, CDKN2B, ITGA2, WNT7B, FZD8, IGF1, FGF17, CXCL12, COL4A1, KIT, AGTR1, BIRC5, PPARG, FGF11, F2RL3, FGF1, ETS1, HEY1, PIM1, IL12A, ITGAV, IL6R, EDN1, ITGA3, WNT5A, FOS, COL4A2, CKS2, CAMK2B, NOTCH3, PTGER2, FOXO1, DLL4, BCL2L11, HMOX1, PMAIP1, HES1, RUNX1T1, JAG2, GADD45B, IGF2, BMP4, HEYL, BMP2, IL6, FGFR4, IL7R
hsa04360:Axon guidance	✓	✓	EPHB6, SEMA6B, EPHA5, SEMA7A, CXCL12, UNC5B, SEMA3D, PLXNA2, UNC5C, SLIT2, PLXNC1, EPHB1, ROBO2, CAMK2B, SEMA4A, EPHA4, TRPC6, TRPC4, WNT5A, NFATC2, EFNA5, BMP7, ENAH, EPHB3
hsa04610:Complement and coagulation cascades	✓	✓	C1QB, THBD, VWF, SERPIND1, PLAU, SERPINC1, CFB, C1QC, CFD, ITGB2, SERPINE1, PLAUR, VTN, F2RL3
hsa05323:Rheumatoid arthritis	✓	✓	TGFB2, FLT1, CXCL12, CXCL8, CSF2, ITGB2, MMP3, CCL2, HLA-DOB, IL11, FOS, IL6, ATP6V1E2, HLA-DQA1, HLA-DQB1
hsa04015:Rap1 signaling pathway	✓	✓	CSF1R, FLT1, ITGB3, FLT4, ITGB2, PDGFB, ADCY4, IGF1, THBS1, PIK3R5, RASGRP3, FGF17, ADORA2B, KIT, FGF11, F2RL3, VASP, ANGPT2, FGF1, EFNA5, ENAH, PFN4, FGFR4, MAP2K6
hsa04080:Neuroactive ligand-receptor interaction	✓	✓	CHRM2, GABRB1, NPY4R, HTR1D, HTR2B, HTR1B, PTH1R, TACR1, SSTR2, GRIN2C, GHR, GRIN3B, HTR7, ADORA2B, AGTR1, F2RL1, S1PR5, F2RL3, GRIA4, CHRM3, UCN, CALCRL, CHRNA5, NPY4R, PTGER2, CHRNA7, OPRL1, GRIK4, ADM, ADRA1D, GRIK2, UCN2, P2RY2, NPY, ADORA1, LHCGR, EDN1, PRLR, P2RX6, GAL, NPY4R2
hsa04115:p53 signaling pathway	✓	✓	CCNB2, CCNB1, RRM2, GADD45B, CHEK2, CDK1, IGF1, THBS1, GTSE1, SERPINE1, PMAIP1
hsa04810:Regulation of actin cytoskeleton	✓	✓	CHRM2, ITGB3, ITGA2, ITGB2, ITGA1, PDGFB, IQGAP3, PIK3R5, MYLPF, FGF17, DIAPH3, TMSB4Y, ITGA7, NCKAP1L, FGF11, ACTR3, CHRM3, ITGA4, ITGB4, ITGA3, MSN, FGF1, ENAH, SCIN, CXCL12, PFN4, ITGAV, MYH11, FGFR4, ITGA9
hsa04020:Calcium signaling pathway	✓	✓	CHRM2, CAMK2B, SPHK1, ADCY4, HTR2B, CACNA1A, TACR1, GRIN2C, CACNA1G, HTR7, ERBB3, ADORA2B, AGTR1, RYR1, CHRM3, FLT1, PDE1A, CHRNA7, PDGFB, ADRA1D, ITPR3, FGF1, SLC8A1, LHCGR, TNNC2, MCOLN2, P2RX6, ITPKA, FGFR4

Table 4.8: Biological pathways impacted by differentially expressed genes in GCR IR alone or GCR+cNLP radioprotection treatment. *Note: Differentially expressed gene hits per pathway are colored as follows: Black-*

colored genes (differentially expressed in pathway for both treatment groups), orange-colored genes (differentially expressed in pathway in the GCR+cNLP radioprotection group only), blue-colored genes (differentially expressed in pathway for the GCR alone group only). All pathway hits had p-values <0.1.

Given that the 5-ion simulated GCR exposures is comprised of mostly protons (~74%), we compared the differential expression hits amongst proton+cNLP and GCR+cNLP irradiation groups. We identified 39 overlapping up-regulated and 162 overlapping down-regulated genes between proton+cNLP and GCR+cNLP IR groups (Figure 4.9). The total differentially expressed gene hits in each cNLP radioprotection treatment were then loaded into DAVID NCBI database. We uncovered 9 shared biological pathways of interest between proton+cNLP and GCR+cNLP treatment groups (Table 4.9). The top differentially expressed genes within these shared pathways were involved in cell cycle progression, oocyte meiosis and maturation, and p53 signaling. Interestingly, ABC transporter function was not modulated in proton IR alone or GCR IR alone control groups without cNLP radioprotective treatment (Table 4.9).

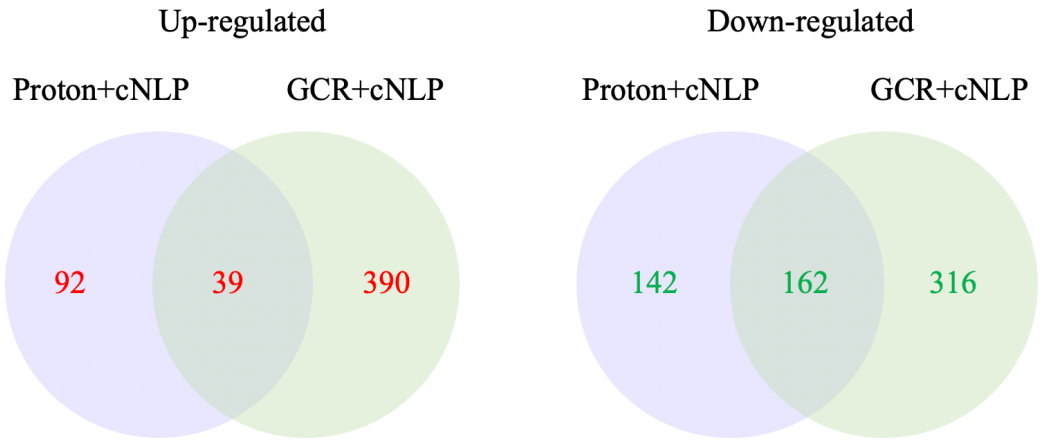

Figure 4.9: Differentially expressed genes comparison of Proton+cNLP and GCR+cNLP groups. Shown are the differentially expressed genes via RNA sequencing in MRC-5 cells exposed to 100 cGy proton exposures with cNLP radioprotective treatment (Proton+cNLP) or 75 cGy 5-ion simulated GCR exposures with cNLP radioprotective treatment (GCR+cNLP). Up-regulated genes are in red and down-regulated genes are in green. Differentially expressed genes satisfied the following criteria: $\log_2$ fold change (+/-1), $p<0.05$, FDR<0.05.

Biological pathways shared amongst Proton+cNLP and GCR+cNLP treatment groups	Differentially expressed genes shared amongst Proton+cNLP and GCR+cNLP treatment groups
hsa04110:Cell cycle	PLK1, BUB1B, TTK, PKMYT1, CDC25C, CCNA2, CDC20, CCNB2, CCNB1, CDC45, PTTG1, CDK1, E2F2, BUB1, MAD2L1
hsa04114:Oocyte meiosis	CAMK2B, CDC20, CCNB2, CCNB1, PTTG1, PLK1, CDK1, PKMYT1, CDC25C, BUB1, MAD2L1
hsa04914:Progesterone-mediated oocyte maturation	CCNA2, CCNB2, CCNB1, PLK1, CDK1, PKMYT1, CDC25C, BUB1, MAD2L1
hsa04115:p53 signaling pathway	CCNB2, CCNB1, RRM2, CDK1, GTSE1
hsa00982:Drug metabolism - cytochrome P450	ADH1C, ADH1B, ADH1A, FMO2
hsa04060:Cytokine-cytokine receptor interaction	TNFSF18, CXCL12, CCL11, CCL7, TNFSF4, TNFSF10
hsa04068:FoxO signaling pathway	PLK4, CCNB2, CCNB1, PLK1, TNFSF10
hsa05214:Glioma	CAMK2B, PDGFB, E2F2
hsa02010:ABC transporters	ABCB1, ABCA8, ABCA13, ABCG1

Table 4.9: Shared biological pathways and differentially expressed genes impacted by Proton+cNLP or GCR+cNLP treatments. *Note: Up-regulated genes are in red and down-regulated transcripts are in green. All pathway hits had p-values <0.1.*

Comparing cNLP radioprotective vs. radiomitigative treatments identifies novel biological pathways of interest

We next evaluated the similarities and differences amongst cNLP radioprotection and radiomitigation treatments following various qualities of IR exposures. Total numbers of differentially expressed genes across radiation mitigation groups can be found in the Appendix (Appendix Table A.4.8). We then inputted the total up-regulated and down-regulated gene lists within each cNLP radiomitigation group into the DAVID NCBI database and identified downstream biological pathways of interest (Table 4.10). In contrast to cNLP radioprotection treatment, where we found two biological pathways (cell cycle and p53 signaling) overlapping in SHAM, gamma, proton, Fe-56, and GCR irradiated groups, we found 5 overlapping biological

pathways in cNLP RM groups (Table 4.10). Top pathway hits in cNLP radiomitigation groups were steroid biosynthesis, ECM receptor interactions, and metabolism. In addition, top biological pathways with curcumin mitigation treatment also included antibiotic synthesis and focal adhesion (Table 4.10).

Biological pathways	Treatment group (+cNLP RM)
hsa00100:Steroid biosynthesis	All (SHAM, gamma, proton, Fe-56, GCR)
hsa01100:Metabolic pathways	All (SHAM, gamma, proton, Fe-56, GCR)
hsa01130:Biosynthesis of antibiotics	All (SHAM, gamma, proton, Fe-56, GCR)
hsa04510:Focal adhesion	All (SHAM, gamma, proton, Fe-56, GCR)
hsa04512:ECM-receptor interaction	All (SHAM, gamma, proton, Fe-56, GCR)
hsa00260:Glycine, serine and threonine metabolism	SHAM, proton, Fe-56, GCR
hsa00900:Terpenoid backbone biosynthesis	SHAM, gamma, proton, Fe-56
hsa04151:PI3K-Akt signaling pathway	SHAM, gamma, Fe-56, GCR
hsa05323:Rheumatoid arthritis	SHAM, gamma, Fe-56, GCR
hsa00561:Glycerolipid metabolism	SHAM, gamma, Fe-56
hsa01040:Biosynthesis of unsaturated fatty acids	SHAM, gamma, Fe-56
hsa01212:Fatty acid metabolism	Gamma, proton, Fe-56
hsa02010:ABC transporters	SHAM, gamma, GCR
hsa04015:Rap1 signaling pathway	SHAM, gamma, Fe-56
hsa04060:Cytokine-cytokine receptor interaction	SHAM, Fe-56, GCR
hsa04115:p53 signaling pathway	SHAM, gamma, GCR
hsa04610:Complement and coagulation cascades	SHAM, proton, Fe-56
hsa04668:TNF signaling pathway	SHAM, Fe-56, GCR
hsa04810:Regulation of actin cytoskeleton	Gamma, Fe-56, GCR
hsa05143:African trypanosomiasis	SHAM, Fe-56, GCR
hsa05144:Malaria	SHAM, Fe-56, GCR
hsa05146:Amoebiasis	SHAM, Fe-56, GCR
hsa05200:Pathways in cancer	SHAM, Fe-56, GCR
hsa05410:Hypertrophic cardiomyopathy (HCM)	SHAM, gamma, Fe-56
hsa05412:Arrhythmogenic right ventricular cardiomyopathy (ARVC)	SHAM, gamma, proton

Table 4.10: Top biological pathways that are shared amongst radiation mitigation treatment groups.

In a direct comparison between cNLP radioprotection and radiomitigation treatments exposed to gamma rays, we found 230 differentially expressed genes in the gamma+cNLP radioprotection timeline and 633 differentially expressed genes in the gamma+cNLP radiomitigation timeline

(Tables A.4.6 and A.4.8). We identified 25 modulated biological pathways in the gamma+cNLP radiomitigation group compared to only 5 biological pathways in the gamma+cNLP radioprotection group (Table 4.11). Overall, we found that p53 signaling and cell cycle effects were the only two biological pathways that overlapped between gamma radioprotection and gamma radiomitigation treatments (Table 4.11).

Gamma+cNLP (Radioprotection)		**Gamma+cNLP (Radiomitigation)**	
Pathway	**P-value**	**Pathway**	**P-value**
Cell cycle*	1.30E-13	Cell cycle*	2.21E-02
p53 signaling pathway*	7.22E-04	p53 signaling pathway*	2.35E-02
Oocyte meiosis	2.09E-08	Steroid biosynthesis	2.73E-15
Progesterone-mediated oocyte maturation	3.61E-06	Biosynthesis of antibiotics	2.72E-08
Hepatitis B	7.03E-02	Terpenoid backbone biosynthesis	6.08E-05
		Metabolic pathways	1.25E-04
		Glycerolipid metabolism	6.07E-04
		Glycolysis / Gluconeogenesis	6.58E-03
		ECM-receptor interaction	8.12E-03
		Hypertrophic cardiomyopathy (HCM)	1.47E-02
		Fructose and mannose metabolism	2.07E-02
		Fatty acid metabolism	2.09E-02
		Dilated cardiomyopathy	2.14E-02
		Arrhythmogenic right ventricular cardiomyopathy (ARVC)	2.35E-02
		Rheumatoid arthritis	2.68E-02
		FoxO signaling pathway	3.43E-02
		PI3K-Akt signaling pathway	3.84E-02
		Biosynthesis of unsaturated fatty acids	3.95E-02
		Bladder cancer	4.63E-02
		Rap1 signaling pathway	4.72E-02
		Regulation of actin cytoskeleton	4.72E-02
		ABC transporters	5.75E-02
		Focal adhesion	8.17E-02
		Circadian entrainment	9.63E-02
		HIF-1 signaling pathway	1.00E-01

Table 4.11: Biological pathways associated with gamma irradiation and either cNLP radioprotective or radiomitigative treatment. *Note: * indicates pathways that were differentially regulated in both radiation protection and radiation mitigation treatments*

In simulated GCR-irradiated samples, we found 907 differentially expressed genes in cells treated with the cNLP radioprotection timeline and 849 differentially expressed genes in the cells treated with the cNLP radiomitigation timeline (Tables A.4.6 and A.4.8). In the GCR+cNLP radioprotection group, there were 35 pathways modulated. In contrast, GCR+cNLP radiation mitigation treatment affected 48 biological pathways, with only 16 (33.3%) overlapping with radioprotection treatment (Table 4.12).

GCR+cNLP (Radioprotection)		**GCR+cNLP (Radiomitigation)**	
Pathway	**P-value**	**Pathway**	**P-value**
ECM-receptor interaction*	3.46E-04	ECM-receptor interaction*	2.87E-03
Focal adhesion*	5.93E-04	Focal adhesion*	4.41E-02
Cytokine-cytokine receptor interaction*	8.27E-04	Cytokine-cytokine receptor interaction*	9.75E-04
Oocyte meiosis*	9.86E-04	Oocyte meiosis*	3.86E-02
Malaria*	1.10E-03	Malaria*	7.70E-04
Progesterone-mediated oocyte maturation*	1.27E-03	Progesterone-mediated oocyte maturation*	6.62E-02
PI3K-Akt signaling pathway*	7.92E-03	PI3K-Akt signaling pathway*	1.92E-03
ABC transporters*	1.12E-02	ABC transporters*	8.70E-03
Pathways in cancer*	1.17E-02	Pathways in cancer*	3.29E-02
Tyrosine metabolism*	1.67E-02	Tyrosine metabolism*	2.72E-03
Rheumatoid arthritis*	3.68E-02	Rheumatoid arthritis*	2.32E-04
Cell adhesion molecules (CAMs)*	4.45E-02	Cell adhesion molecules (CAMs)*	1.37E-02
HTLV-I infection*	4.93E-02	HTLV-I infection*	8.25E-03
p53 signaling pathway*	7.00E-02	p53 signaling pathway*	5.65E-02
Regulation of actin cytoskeleton*	7.28E-02	Regulation of actin cytoskeleton*	9.21E-02
Drug metabolism - cytochrome P450*	7.41E-02	Drug metabolism - cytochrome P450*	5.99E-02
Cell cycle	1.37E-06	Inflammatory mediator regulation of TRP channels	2.18E-03
FoxO signaling pathway	6.24E-05	Glycolysis / Gluconeogenesis	3.67E-04
Hypertrophic cardiomyopathy (HCM)	1.89E-03	Ovarian steroidogenesis	1.43E-04
Dilated cardiomyopathy	3.29E-03	TNF signaling pathway	6.49E-06
Proteoglycans in cancer	6.04E-03	HIF-1 signaling pathway	5.86E-03
Axon guidance	2.19E-02	Transcriptional misregulation in cancer	8.68E-03
Glioma	2.20E-02	Biosynthesis of amino acids	9.05E-03
Complement and coagulation cascades	2.94E-02	NF-kappa B signaling pathway	9.16E-03
Rap1 signaling pathway	3.96E-02	Gastric acid secretion	9.81E-03
MicroRNAs in cancer	4.23E-02	Amoebiasis	1.16E-02
Type II diabetes mellitus	5.60E-02	Biosynthesis of antibiotics	1.38E-02
Neuroactive ligand-receptor interaction	5.64E-02	Chemical carcinogenesis	1.65E-02
Melanogenesis	6.86E-02	Bile secretion	2.26E-02
Natural killer cell mediated cytotoxicity	8.32E-02	cAMP signaling pathway	3.33E-02
Legionellosis	8.41E-02	Circadian entrainment	4.11E-02
Melanoma	8.72E-02	African trypanosomiasis	4.49E-02

GCR+cNLP (Radioprotection) (continued)		GCR+cNLP (Radiomitigation) (continued)	
Pathway	**P-value**	**Pathway**	**P-value**
Aldosterone-regulated sodium reabsorption	8.75E-02	Steroid biosynthesis	4.68E-02
Calcium signaling pathway	8.92E-02	Retinol metabolism	4.69E-02
Nicotine addiction	9.41E-02	Central carbon metabolism in cancer	4.69E-02
		Influenza A	5.45E-02
		PPAR signaling pathway	5.65E-02
		Toll-like receptor signaling pathway	6.98E-02
		Metabolic pathways	7.08E-02
		Leishmaniasis	7.10E-02
		Glycine, serine and threonine metabolism	7.48E-02
		NOD-like receptor signaling pathway	7.92E-02
		Viral myocarditis	8.40E-02
		Cholinergic synapse	8.61E-02
		Maturity onset diabetes of the young	8.93E-02
		Osteoclast differentiation	9.00E-02
		Type I diabetes mellitus	9.27E-02
		MAPK signaling pathway	9.72E-02

Table 4.12: Biological pathways associated with GCR irradiation and cNLP radioprotective or radiomitigative treatment. *Note: * indicates pathways that were differentially regulated in both radiation protection and radiation mitigation treatments*

Targeted qPCR identifies and validates important pathway-specific responses for curcumin as a radioprotectant and radiomitigator

Given that the p53 pathway is canonically activated in response to ionizing radiation exposures and curcumin is a well-known antioxidant, we explored whether targeted genes within the p53 or Nrf2 antioxidant-response-element (ARE) pathways would be modulated in response to cNLP radioprotective or radiomitigative treatments. We calculated gene expression differences on a panel of 6 transcripts linked to p53 pathway (*CDKN1A*, *FDXR*, *BAX*, *BCL2*, *BCL2L1*, and *DDB2*) and 4 transcripts involved in antioxidant response (*NFE2L2* (NRF2), *NQO1*, *KEAP1*, and *HMOX1*) (Table 4.13). Overall, we found that both cNLP radioprotection and radiomitigation up-regulated antioxidant transcripts *HMOX1*, *NQO1*, *NFE2L2* (NRF2), and *KEAP1* across gamma, proton, Fe-56, and GCR irradiation groups compared to curDMSO or DMSO alone controls.

Moreover, cNLP radioprotection up-regulated the p53 transcripts *CDKN1A*, *FDXR*, *DDB2*, and *BAX* over IR alone controls. Interestingly, cNLP radiomitigation treatment decreased *BCL2* and *BCL2L1* transcript expression levels over cNLP radioprotection groups or IR alone controls (Figure 4.10). Individual transcript fold changes across all treatment groups are shown in Appendix (Figure A.4.3).

Gene	Name	Primer No.	Pathways	Biological Processes
GAPDH	Glyceraldehyde-3-phosphate dehydrogenase	Hs02758991		Glycolysis
CDKN1A	Cyclin dependent kinase inhibitor 1A	Hs00355782	TP53, ErbB , HIF1, FoxO, PI3K/AKT	DNA damage repair, Cell cycle arrest, Apoptosis
FDXR	Ferredoxin reductase	Hs00244586	TP53, Metabolism	Electron Transport
BAX	BCL2 Associated X Protein	Hs99999001	TP53	Apoptosis (pro)
BCL2	B-Cell CLL/Lymphoma 2	Hs99999018	NFKB, HIF1, TP53, PI3K/AKT	Apoptosis (anti)
BCL2L1/ BCLXL	BCL2 like 1	Hs00236329	Ras MAPK, NFKB, TP53, PI3K/AKT	Apoptosis (anti)
DDB2	Damage Specific DNA Binding Protein 2	Hs03044953	TP53	Nucleotide Excision Repair
NFE2L2 (NRF2)	NFE2 Like BZIP Transcription Factor 2	Hs00975961	NRF2 survival signaling, HO-1, Antioxidant response, NF-kB	Oxidative stress, Injury, and Inflammation
NQO1	NAD(P)H Quinone Dehydrogenase 1	Hs02512143	Metabolism, NRF2 survival signaling	Oxidative stress, Apoptosis
KEAP1	Kelch Like ECH Associated Protein 1	Hs00202227	NRF2 signaling	Oxidative stress, Autophagy, Ubiquitination
HMOX1	Heme Oxygenase 1	Hs01110250	IL-4, IL-13, NRF2 signaling	Oxidative stress, Inflammation, Thrombosis (anti)

Table 4.13: Selected transcripts of interest for quantitative real-time PCR

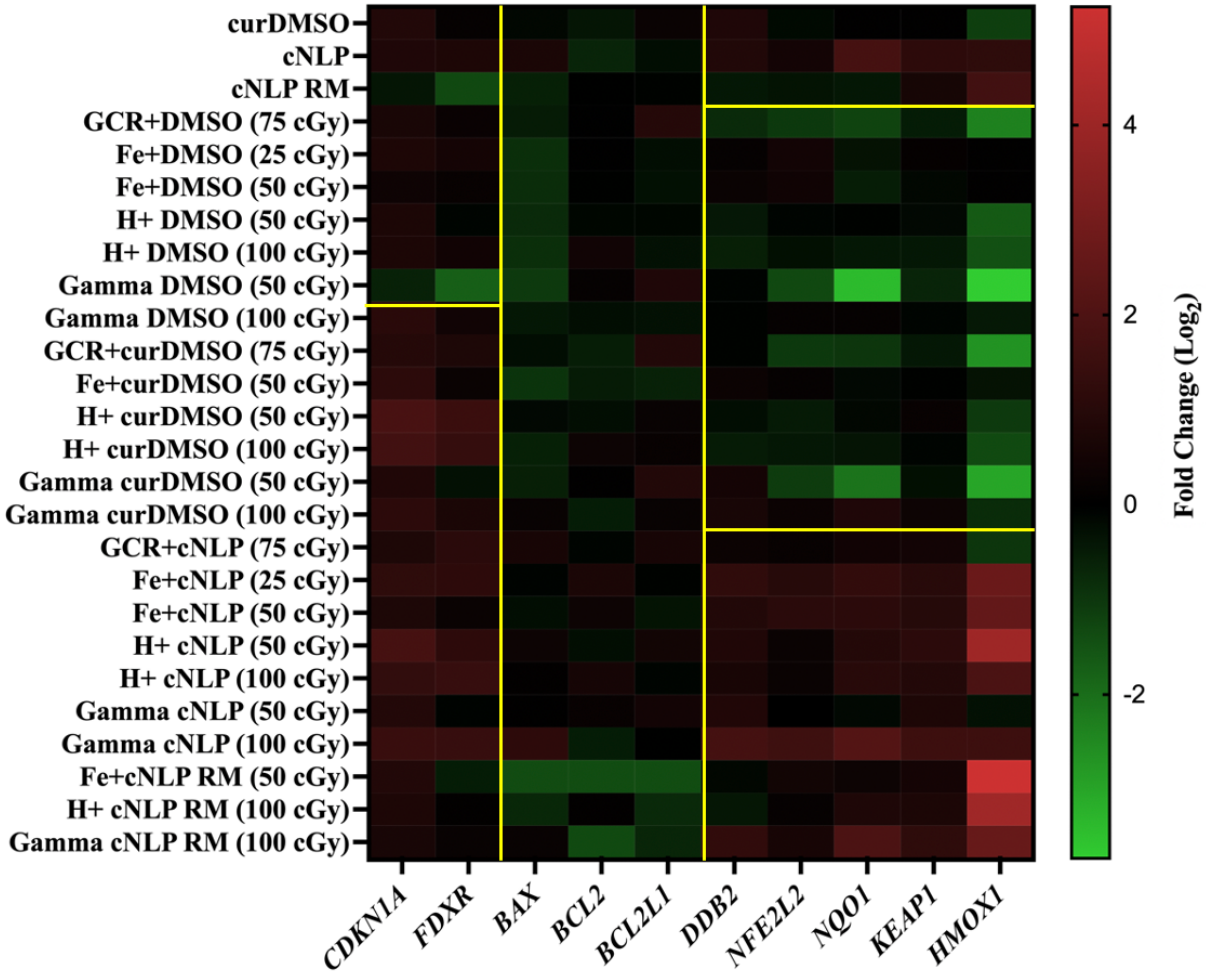

Figure 4.10: Heatmap of DNA damage and antioxidant responding transcripts across various IR groups with and without curcumin treatments. Fold changes are based on qPCR analysis. Shown are the log_2 fold changes compared to GAPDH normalizer gene. The IR alone and curDMSO group fold changes are with respect to SHAM (DMSO) alone control group. The cNLP and cNLP RM group fold changes are with respect to SHAM (no DMSO) control.

4.5 Discussion

The space environment beyond LEO comprises a complex mixture of ion species that pose great risk to human health, particularly for long-term flights (4, 6, 7). For a 3-year Mars mission, astronauts are projected to be exposed to about 1 Gy (1.2 Sv equivalent dose) of radiation through

a combination of GCR particles, solar flares (SPE), as well as Van Allen radiation belts (4, 7). GCR particles, comprised of mostly protons, helium ions, as well as numerous HZE species, are projected to contribute to the majority of IR dose, with an estimated proton particle hitting each of an astronauts' cells every 3 days, a helium ion every few weeks, and a HZE particle every few months (4). Due to the high frequency of particle "hits", both short-term and long-term effects following ionizing radiation exposures constitute significant risks associated with deep space flight. Moreover, understanding the biological pathways induced through these unique exposures will aid in the development of safe and effective radiological countermeasures.

In this chapter, we have shown that the transcriptional profiles and affected biological pathways differ in response to low (gamma, proton), high-LET (Fe-56), or space radiation (GCR) exposures. Most interestingly, for the first time, we illustrate that curcumin radioprotection and radiomitigation treatments following simulated GCR exposures further alter the transcriptional responses of these exposures and resulting biological pathways. We also demonstrate that the timing of cNLP administration plays a dominant role in the way normal human fibroblasts respond to IR exposures, with radiomitigation treatment altering significantly more genes and biological pathways than cNLP radioprotective treatment. Furthermore, our targeted qPCR findings on p53 and antioxidant-response-element transcripts highlighted how cNLP administration drives increased cell-cycle arrest (*CDKN1A*), DNA damage response (*DDB2*), apoptosis (*BCL2*, *BCL2L1*) and antioxidant response genes (*HMOX1*, *NFE2L2*, *KEAP1*, *NQO1*) that regulate anti-inflammatory and cell survival processes. Taken together, our findings illustrate that cNLPs may perform as effective radiological countermeasures throughout a deep space mission.

When looking at the top up- and down-regulated genes per IR quality as determined via RNA sequencing, we found overlapping neural homeostasis pathways and calcium signaling modulation within proton and Fe-56 IR groups (Table 4.4b-c). These findings align with previous reports that Fe-56 exposures may contribute to neurological deficits (17-19) as well as calcium dysfunction as soon as 24 hours after IR exposure (20). Interestingly, we also revealed that G protein-Coupled Receptor (GPCR) pathways were modulated in the top differentially expressed genes within both GCR and proton irradiated groups. This coincides with recent evidence that GPCRs may be critical regulators following DNA damage IR responses (21).

Furthermore, our study emphasized both shared and unique gene ontology processes that occur downstream of IR exposures. We showed that different IR qualities (gamma, proton, Fe-56, and GCR) contribute to similar gene ontology processes including cell cycle arrest, mitotic regulation, and protein phosphorylation (Table 4.5a). We also found that ubiquitin regulation was a predominant biological process following both proton and gamma IR exposures. These findings involving cell cycle arrest correspond with canonical IR responses previously described following cellular stress and genotoxic insult (22). Furthermore, epigenetic modifications, including histone modifications as well as modulation of non-coding RNA molecules, have also been previously well-documented following IR exposures (23). However, we also noticed large variety in the biological functions impacted through differing IR qualities, with low-LET gamma irradiation contributing to the least amount of disturbed biological functions and GCR contributing to the widest range of biological perturbations (Table 4.5a-b).

In looking at the differences in DNA DSBs amongst low and high-LET ion species, we found that the low-LET ion species (gamma, proton) contribute to more DNA DSB per cGy than high-LET species (Fe-56), with about 0.12-0.14 induced foci/cGy in low-LET IR and 0.07 induced

foci/cGy in high-LET IR (Table 4.2, Table 4.6). Our findings correspond with previously published gamma-irradiation experiments which found 0.11-0.21 induced foci/cGy across 25 normal human fibroblast cell lines (24). Furthermore, our findings that higher-LET ions induced fewer foci/cGy than lower-LET counterparts align with our predictions, as the relative particle fluences of these high-LET ions drop by orders of magnitude compared to lower-LET ions (given that more energy is transferred in high-LET ions per unit dose). Our results suggests that although the high-LET ions contributed to lower foci/cGy, these high-LET ion species may lead to increased foci per particle track (and higher RBE) than lower LET counterparts. Desai and colleagues have demonstrated that the biological tracks induced through high-LET radiation are distinctly different than those induced through lower-LET counterparts, with one high-LET particle leading to irradiation "streaks" that are not seen in lower-LET radiations (25). These particle "streaks" induced through high-LET radiation, therefore, led to increased biological damage that is LET-dependent (25). In contrast to Desai and colleagues, where the cells were irradiated with only about a 5% angle difference from the beam, in our study we irradiated our cells perpendicular to the IR beam. Thus, although we found less DNA DSB per cGy in the higher LET ions, it is possible that this is due to less visibility of the high-LET particle "streaks" within cell nuclei, essentially missing the extent of the biological damage that may occur with exposure to high-LET ions.

In Chapter 3 of this dissertation, we demonstrated that curcumin nanolipoprotein particle discs (cNLPs) display limited survival benefit in Cs-137 irradiated cell cultures over DMSO-solubilized curcumin and robust survival benefit over empty NLP controls, particularly at higher doses. In this chapter, we expanded upon these studies and illustrated potential transcriptomic responses at play given cNLP radiation protection or radiomitigation treatments following a space relevant IR exposure with direct comparison to gamma rays. Firstly, our findings suggest cNLPs administered

as a radioprotection agent may partially protect against gamma ray exposures through regulating oxidative damage responses, as cNLP radiation protection groups had ~8x more up-regulated genes and ~1.4x more down-regulated genes than gamma IR alone as well as higher expression levels of antioxidant response genes *NFE2L2*, *NQO1*, *KEAP1*, and *HMOX1* over curDMSO or IR alone controls (Figures 4.7 and 4.10). We also found less biological pathway modulations following gamma+cNLP irradiation than gamma IR alone, suggesting that cNLPs may protect against downstream biological perturbations (Table 4.7). In addition, in space relevant IR groups (GCR), our findings suggest that curcumin NLP pre-treatment may similarly protect against IR exposures through transcriptional up-regulation of antioxidant response genes *NFE2L2*, *NQO1*, *KEAP1*, and *HMOX1* over IR alone controls (Figure 4.10, Appendix Figure A.4.3). Moreover, we illustrate that cNLP radiation protection treatment may alter additional biological pathways independent of GCR irradiation which may be useful for combating downstream IR-induced toxicities. For example, we have shown that GCR+cNLP radioprotection groups led to unique biological pathway modulation involving ABC transporters, metabolism, immune regulation, and microRNA regulation that were not significant in GCR alone groups (Table A.4.7). Comparing our findings to other studies highlights that curcumin similarly modulates the activity of ABC transporters, enabling reversal of drug resistance in breast cancer cells or in mouse models (26, 27). Moreover, curcumin has been shown to modulate a multitude of miRNAs as well as metabolic processes *in vitro* and *in vivo* (28, 29). Furthermore, we also found that cell cycle and FoxO signaling pathways had more differentially expressed genes associated with GCR+cNLP than GCR alone, suggesting that cNLPs may be modulating mitotic arrest, apoptosis, or oxidative stress responses in an independent manner outside of the effects of GCR irradiation, as has been demonstrated previously (30-32) (Table 4.8) .

We found that certain biological pathways impacted by curcumin radioprotection treatment were consistent between GCR and proton IR exposures, including p53 signaling, mitotic and meiotic arrests, as well as drug metabolism (Table 4.9). Within the qPCR validation studies, we confirmed an elevated p53 response due to up-regulated *CDKN1A*, *FDXR,* and *DDB2* mRNA levels in cells treated with cNLP over IR alone controls, as well as slight modulation on apoptosis-regulating transcripts (*BAX*, *BCL2, BCL2L1*) following cNLP radiation protection treatment (Figure 4.10, Figure A.4.3). Interestingly, in our study, it appears as if apoptosis played less of a role in the gene expression responses, as the fold changes for *BAX*, *BCL2*, and *BCL2L1* were less differentially regulated (~0.5-1 fold) compared to cell cycle arrest and DNA damage biomarkers *CDKN1A*, *FDXR*, and *DDB2* (~2-3 fold). These findings suggest that the predominant p53 mechanisms at play with curcumin radiation protection treatment may be further initiating prolonged cell cycle arrest or the persistence of sublethal DNA damage/DNA repair over cells without curcumin pre-treatment. In essence, cNLP pre-treatment may be priming the p53 pathway for activation. Our results align with previous reports that curcumin can initiate apoptosis (31) and mitotic arrest (33, 34). However, our findings differ in that we see the cell cycle effects and persistence in DNA damage predominate the p53-response over the initiation of apoptosis following cNLP pre-treatment.

The variability of curcumin to act as a radiation protective or radiation sensitization agent has been previously reported and has been thought to be due to state of the cell cycle, with curcumin addition on G0/G1 cultures leading to radioprotection and curcumin addition to actively dividing cultures leading to radiosensitization (32). This coincides with the state of the cell cultures in our experiments (confluent G0/G1 state rather than active mitotic state) prior to cNLP treatment and the fact that we are utilizing a normal human fibroblast line instead of a cancer cell line (with faster

cell metabolism). Although we see apoptosis effects to a lesser extent than would be seen in a cancer cell line, our findings nonetheless align with previous reports displaying that curcumin modulates the p53 pathway through cell cycle, DNA damage, and apoptosis mechanisms (33, 34).

Our findings also suggest that curcumin may serve as a radiation protector in normal human cells through additional mechanisms outside of p53, namely through increased transcription of antioxidant-response genes in the Nrf2 pathway (Figure 4.10, Figure A.4.3). In addition, we showed that the up-regulation of antioxidant-response genes following curcumin radiation protection treatment may transcend across a range of IR qualities and LETs (Figure 4.10, Figure A.4.3). In this study, we displayed that *NFE2L2*, *KEAP1*, *NQO1*, and *HMOX1* transcripts were all consistently up-regulated compared to groups that did not receive cNLP radioprotection treatment in gamma, proton, Fe-56, and GCR IR groups (Figure A.4.3). We also demonstrated that even in the absence of IR exposures, cNLP pre-treated cells had increased antioxidant responses over curcumin dissolved in DMSO (Figure 4.10). These data suggest that cNLPs may similarly be priming the Nrf2 pathway to increase transcription of antioxidant-response genes, even before IR exposures (Figure 4.11). Taken together, our studies show that cNLPs may be priming both the p53 as well as Nrf2 pathways to initiate a radioprotective effect against IR exposures (Figure 4.12).

Interestingly, we did not see a consistent decrease in DNA damage associated foci in the irradiation groups pre-treated with cNLPs (only gamma+cNLP and O-16+cNLP groups had decreased foci at the 15-minute time point, although this was not consistent across all fixation time points). Moreover, we see increased expression of DDB2, a biomarker of DNA damage, persist in cells treated with cNLP as a radioprotectant. These findings suggest that curcumin's role in decreasing DNA repair efficiency and increasing antioxidant gene transcription through p53 and

Nrf2 pathways may dominate over reducing DNA damage associated foci as it pertains to a radiological protectant.

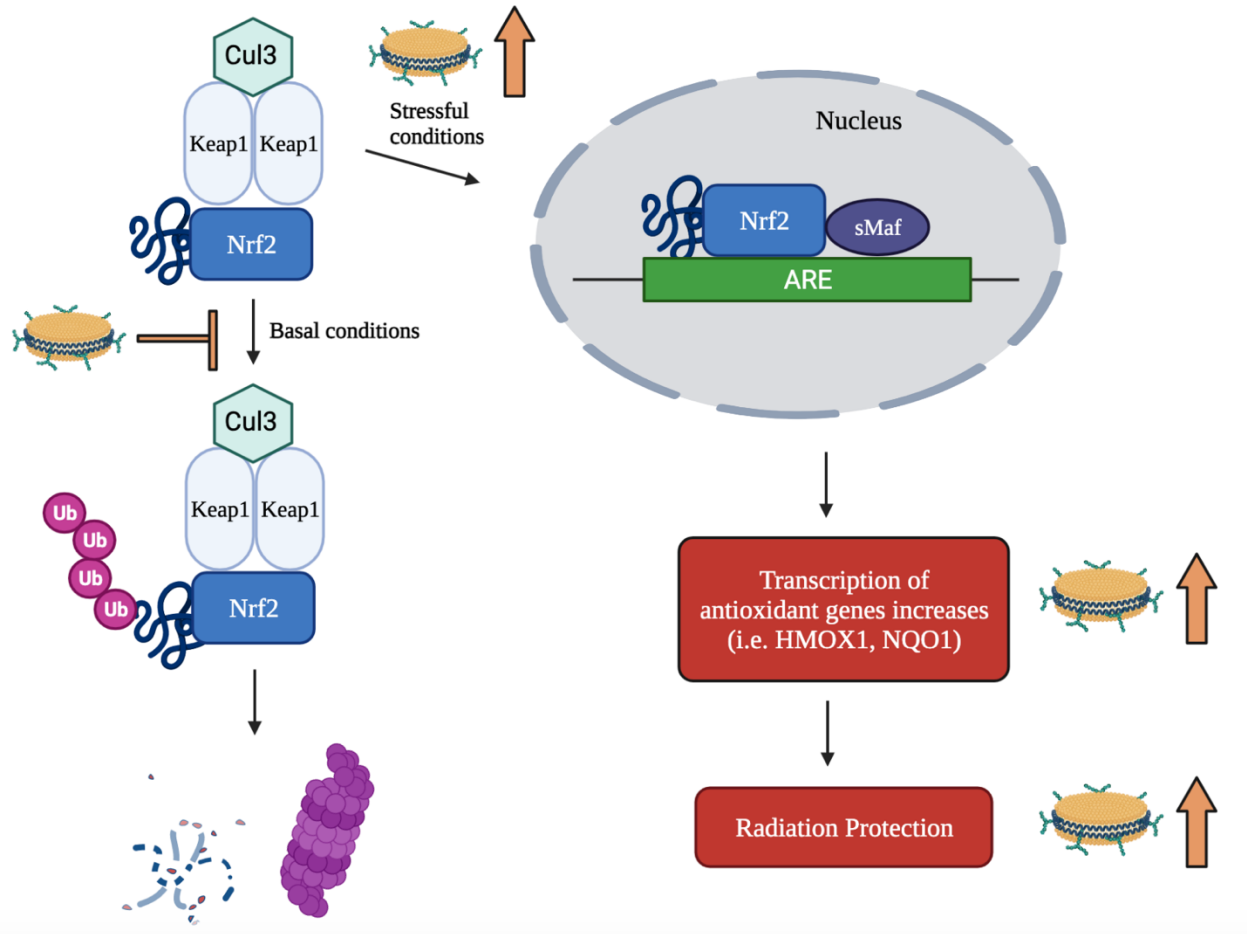

Figure 4.11: Priming of Nrf2 pathway for activation may serve as a mechanism of cNLP-induced radiation protection. Under basal conditions, Nrf2 is bound to a Keap1 complex, poly-ubiquitinated via Cul3, and subsequently degraded within the proteasome. Under stressful conditions, Nrf2 dissociates from the Keap1 complex and translocates to the nucleus, where it dimerizes with small Maf family (sMaf) members and serves as a transcription factor for antioxidant response element (ARE) genes. As a transcription factor, Nrf2 increases the expression of numerous antioxidant response genes, such as HMOX1 and NQO1. We suggest that our cNLPs may be increasing the dissociation of Nrf2 from its bound Keap1 complex, thus increasing Nrf2 translocation to the nucleus and the transcription of antioxidant genes. We hypothesize that cNLPs may be priming the Nrf2 pathway for activation as a mechanism of radiation protection.

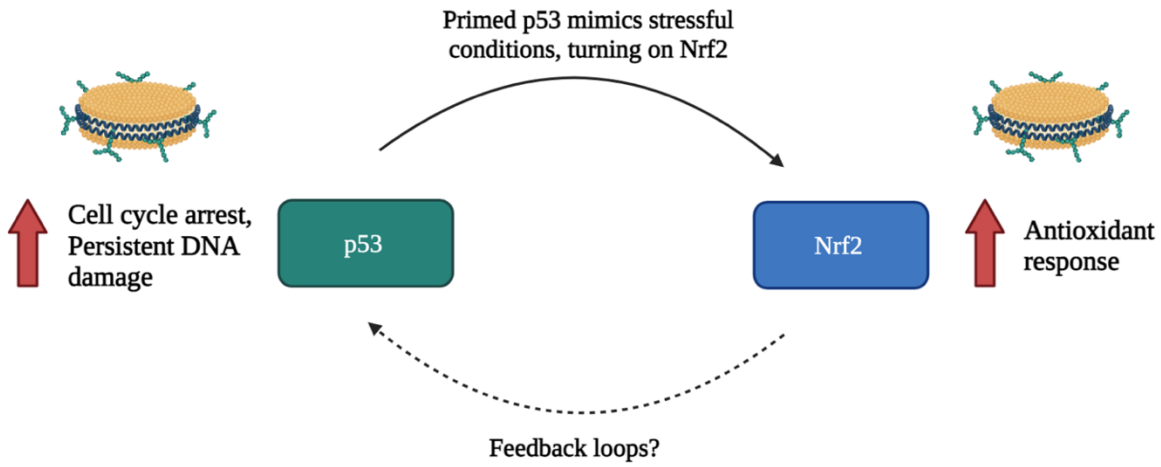

Figure 4.12: cNLP radiation protection treatment reveals relationships between p53 and Nrf2 pathways. Upon cNLP pre-treatment, cells increase p53 activation which leads to increased cell cycle arrest and persistent DNA damage. Similarly, upon cNLP pre-treatment, antioxidant response genes within the Nrf2 pathway increase. Taken together, there may be a relationship between p53 and Nrf2 that is regulated by cNLP pre-treatment. This dichotomy may be priming the cells for subsequent IR exposures and serve as a radiation protective effect.

Furthermore, we found that curcumin radiation mitigation treatment has a distinct transcriptional response that is different than curcumin radiation protection treatment. First, curcumin radiomitigation treatment alters many more biological pathways than radioprotection treatment as shown in both gamma and GCR-irradiated groups (Table 4.11 and Table 4.12). Moreover, we found that the cNLPs had a more consistent role in the affected biological pathways following the radiomitigation treatment timeline than the radioprotection treatment timeline. Namely, steroid biosynthesis, metabolism, antibiotic biosynthesis, focal adhesion, and ECM-receptor interactions were consistently differentially regulated in all the cNLP radiomitigation groups tested (SHAM, gamma, proton, Fe-56, and GCR) (Table 4.10). Our results coincide with previous reports that curcumin modulates steroid biosynthesis and metabolic pathways (28, 35). In addition, our findings suggest that despite various radiological qualities of exposure (or SHAM

unirradiated controls), curcumin's mechanism of action as a radiomitigator demonstrates similar downstream biological pathway activity.

As has been previously shown, the impact of space radiation on human cells and tissues is quite complex and varies across cells and organ systems (36). In particular, environmental changes on mitochondrial activity predominate space flight risks and may lead to secondary problems such as cell cycle, immune regulation, and lipid metabolism alterations (36). Due to the recent opening of the NSRL's simplified 5-ion GCR simulator or full 33-ion simulator GCR beams, there are limited published studies to date regarding the RBE of GCR irradiation. However, one of the first published records utilizing the NSRL beam indicated that GCR irradiation does not seem to alter nutritional food content (including vitamin A, beta carotene, and folates) following 0.5 or 5 Gy irradiation up to 1 year after IR exposures (37). Regarding *in vivo* data, it was also recently published that cognitive deficits in mice were seen following irradiation with the full 33-ion simulated GCR beam, including impaired social novelty characteristics up to 6 months after GCR-sim exposures (38). Interestingly, however, this study found no differences in sociability, locomotion, or anxiety-like behaviors in these GCR irradiated mice over SHAM controls, nor did they find improved response rates on social novelty characteristics when mice were administered a Nrf2-ARE activator, CDDO-ethyl amide, as a radiation protection agent either before, during, or shortly after GCR-simulated exposures (38). It was also recently shown that the simplified 5-ion GCR simulator beam can result in increased bone loss, osteoclast differentiation, mitochondrial respiration alterations and metabolic reprogramming within a mouse model system (39). These studies demonstrate the need for exploring pharmaceutical radiation countermeasures against GCR exposures.

Our data demonstrates that curcumin NLPs may serve as an ideal pharmaceutical countermeasure to protect against space radiation exposures. We show that our cNLPs may serve as safe and effective radioprotective agents by up-regulating p53 and Nrf2 antioxidant-response genes against GCR-simulated exposures in a normal human fibroblast model system. Limitations of this study include that the lack of a comparative *in vivo* model system to date, where the complexity of organs and organ systems may alter the metabolism of a curcumin NLP, its half-life, as well as its overall impact as a transcriptional regulator on p53 and Nrf2-ARE pathways. Another limitation involves the overall design of the NSRL beam, which irradiates biological samples through a serial, "fractionated" total dose over several minutes. At NSRL, each unique ion species is administered "in tandem", rather than a combined "all-in-one" dose as would be seen in space. Moreover, although the doses applied at NSRL accurately reflect total doses of exposure an astronaut may experience in space, the rate at which this dose is administered is in a matter of minutes versus a chronic, low-dose exposure over a matter of months or years while on the spacecraft. This allows for potential confounders in DNA damage and DNA repair kinetics and subsequent pathway activation based on the order of ion species seen in each sample as well as the duration of exposure.

Overall, these findings illustrate the feasibility of cNLPs to potentially perform as effective radiological countermeasures against IR exposures throughout a future Mars mission.

4.6. Acknowledgements

This work was supported by the Translational Research Institute for Space Health through Cooperative Agreement NNX16AO69A. Work was also performed under the auspices of the U.S.

Department of Energy by Lawrence Livermore National Laboratory under contract DE-AC52-07NA27344. Funding was also supported by LLNL LDRD 18-ERD-045.

Chapter 4 References:

1. Montesinos CA, Khalid R, Cristea O, Greenberger JS, Epperly MW, Lemon JA, et al. Space Radiation Protection Countermeasures in Microgravity and Planetary Exploration. Life (Basel). 2021;11(8).
2. Obrador E, Salvador R, Villaescusa JI, Soriano JM, Estrela JM, Montoro A. Radioprotection and Radiomitigation: From the Bench to Clinical Practice. Biomedicines. 2020;8(11).
3. Singh VK, Beattie LA, Seed TM. Vitamin E: tocopherols and tocotrienols as potential radiation countermeasures. J Radiat Res. 2013;54(6):973-88.
4. Nelson GA. Space Radiation and Human Exposures, A Primer. Radiat Res. 2016;185(4):349-58.
5. Zeitlin C, Hassler DM, Cucinotta FA, Ehresmann B, Wimmer-Schweingruber RF, Brinza DE, et al. Measurements of energetic particle radiation in transit to Mars on the Mars Science Laboratory. Science. 2013;340(6136):1080-4.
6. Sihver L, Mortazavi SMJ. Biological Protection in Deep Space Missions. J Biomed Phys Eng. 2021;11(6):663-74.
7. Simonsen LC, Slaba TC, Guida P, Rusek A. NASA's first ground-based Galactic Cosmic Ray Simulator: Enabling a new era in space radiobiology research. PLoS Biol. 2020;18(5):e3000669.
8. Chancellor JC, Scott GB, Sutton JP. Space Radiation: The Number One Risk to Astronaut Health beyond Low Earth Orbit. Life (Basel). 2014;4(3):491-510.
9. Giaccia EJHaAJ. Radiobiology for the Radiologist. Wolters Kluwer, Lippincott Williams & Wilkins; 2012. p. 114-28.
10. Rodman C, Almeida-Porada G, George SK, Moon J, Soker S, Pardee T, et al. In vitro and in vivo assessment of direct effects of simulated solar and galactic cosmic radiation on human hematopoietic stem/progenitor cells. Leukemia. 2017;31(6):1398-407.
11. Almeida-Porada G, Rodman C, Kuhlman B, Brudvik E, Moon J, George S, et al. Exposure of the Bone Marrow Microenvironment to Simulated Solar and Galactic Cosmic Radiation Induces Biological Bystander Effects on Human Hematopoiesis. Stem Cells Dev. 2018;27(18):1237-56.
12. Barnette BL, Yu Y, Ullrich RL, Emmett MR. Mitochondrial Effects in the Liver of C57BL/6 Mice by Low Dose, High Energy, High Charge Irradiation. Int J Mol Sci. 2021;22(21).
13. Jagetia GC. Radioprotection and radiosensitization by curcumin. Adv Exp Med Biol. 2007;595:301-20.
14. Edmondson DA, Karski EE, Kohlgruber A, Koneru H, Matthay KK, Allen S, et al. Transcript Analysis for Internal Biodosimetry Using Peripheral Blood from Neuroblastoma Patients Treated with (131)I-mIBG, a Targeted Radionuclide. Radiat Res. 2016;186(3):235-44.
15. Luo Z, Li D, Luo X, Li L, Gu S, Yu L, et al. Curcumin may serve an anticancer role in human osteosarcoma cell line U-2 OS by targeting ITPR1. Oncol Lett. 2018;15(4):5593-601.
16. Toegel S, Huang W, Piana C, Unger FM, Wirth M, Goldring MB, et al. Selection of reliable reference genes for qPCR studies on chondroprotective action. BMC Mol Biol. 2007;8:13.
17. Allen AR, Raber J, Chakraborti A, Sharma S, Fike JR. (56)Fe Irradiation Alters Spine Density and Dendritic Complexity in the Mouse Hippocampus. Radiat Res. 2015;184(6):586-94.

18. Vlkolinsky R, Krucker T, Smith AL, Lamp TC, Nelson GA, Obenaus A. Effects of lipopolysaccharide on 56Fe-particle radiation-induced impairment of synaptic plasticity in the mouse hippocampus. Radiat Res. 2007;168(4):462-70.
19. Vlkolinsky R, Titova E, Krucker T, Chi BB, Staufenbiel M, Nelson GA, et al. Exposure to 56Fe-particle radiation accelerates electrophysiological alterations in the hippocampus of APP23 transgenic mice. Radiat Res. 2010;173(3):342-52.
20. Shtifman A, Pezone MJ, Sasi SP, Agarwal A, Gee H, Song J, et al. Divergent modification of low-dose (5)(6)Fe-particle and proton radiation on skeletal muscle. Radiat Res. 2013;180(5):455-64.
21. Leysen H, van Gastel J, Hendrickx JO, Santos-Otte P, Martin B, Maudsley S. G Protein-Coupled Receptor Systems as Crucial Regulators of DNA Damage Response Processes. Int J Mol Sci. 2018;19(10).
22. Giaccia EJHaAJ. Radiobiology for the Radiologist. Wolters Kluwer, Lippincott Williams & Wilkins; 2012. p. 54-66.
23. Belli M, Tabocchini MA. Ionizing Radiation-Induced Epigenetic Modifications and Their Relevance to Radiation Protection. Int J Mol Sci. 2020;21(17).
24. Wilson PF, Nham PB, Urbin SS, Hinz JM, Jones IM, Thompson LH. Inter-individual variation in DNA double-strand break repair in human fibroblasts before and after exposure to low doses of ionizing radiation. Mutat Res. 2010;683(1-2):91-7.
25. Desai N, Davis E, O'Neill P, Durante M, Cucinotta FA, Wu H. Immunofluorescence detection of clustered gamma-H2AX foci induced by HZE-particle radiation. Radiat Res. 2005;164(4 Pt 2):518-22.
26. Shukla S, Zaher H, Hartz A, Bauer B, Ware JA, Ambudkar SV. Curcumin inhibits the activity of ABCG2/BCRP1, a multidrug resistance-linked ABC drug transporter in mice. Pharm Res. 2009;26(2):480-7.
27. Wen C, Fu L, Huang J, Dai Y, Wang B, Xu G, et al. Curcumin reverses doxorubicin resistance via inhibition the efflux function of ABCB4 in doxorubicinresistant breast cancer cells. Mol Med Rep. 2019;19(6):5162-8.
28. Aggarwal BB. Targeting inflammation-induced obesity and metabolic diseases by curcumin and other nutraceuticals. Annu Rev Nutr. 2010;30:173-99.
29. Liu Y, Sun H, Makabel B, Cui Q, Li J, Su C, et al. The targeting of noncoding RNAs by curcumin: Facts and hopes for cancer therapy (Review). Oncol Rep. 2019;42(1):20-34.
30. Karunagaran D, Rashmi R, Kumar TR. Induction of apoptosis by curcumin and its implications for cancer therapy. Curr Cancer Drug Targets. 2005;5(2):117-29.
31. Martinez-Castillo M, Villegas-Sepulveda N, Meraz-Rios MA, Hernandez-Zavala A, Berumen J, Coleman MA, et al. Curcumin differentially affects cell cycle and cell death in acute and chronic myeloid leukemia cells. Oncol Lett. 2018;15(5):6777-83.
32. Verma V. Relationship and interactions of curcumin with radiation therapy. World J Clin Oncol. 2016;7(3):275-83.
33. Hu A, Huang JJ, Zhang JF, Dai WJ, Li RL, Lu ZY, et al. Curcumin induces G2/M cell cycle arrest and apoptosis of head and neck squamous cell carcinoma in vitro and in vivo through ATM/Chk2/p53-dependent pathway. Oncotarget. 2017;8(31):50747-60.
34. Talib WH, Al-Hadid SA, Ali MBW, Al-Yasari IH, Ali MRA. Role of curcumin in regulating p53 in breast cancer: an overview of the mechanism of action. Breast Cancer (Dove Med Press). 2018;10:207-17.

35. Rodriguez Castano P, Parween S, Pandey AV. Bioactivity of Curcumin on the Cytochrome P450 Enzymes of the Steroidogenic Pathway. Int J Mol Sci. 2019;20(18).
36. da Silveira WA, Fazelinia H, Rosenthal SB, Laiakis EC, Kim MS, Meydan C, et al. Comprehensive Multi-omics Analysis Reveals Mitochondrial Stress as a Central Biological Hub for Spaceflight Impact. Cell. 2020;183(5):1185-201 e20.
37. Douglas GL, Cooper MR, Wu H, Gaza R, Guida P, Young M. Impact of galactic cosmic ray simulation on nutritional content of foods. Life Sci Space Res (Amst). 2021;28:22-5.
38. Kiffer FC, Luitel K, Tran FH, Patel RA, Guzman CS, Soler I, et al. Effects of a 33-ion sequential beam galactic cosmic ray analog on male mouse behavior and evaluation of CDDO-EA as a radiation countermeasure. Behav Brain Res. 2022;419:113677.
39. Kim HN, Richardson KK, Krager KJ, Ling W, Simmons P, Allen AR, et al. Simulated Galactic Cosmic Rays Modify Mitochondrial Metabolism in Osteoclasts, Increase Osteoclastogenesis and Cause Trabecular Bone Loss in Mice. Int J Mol Sci. 2021;22(21).

Chapter 4 Appendix

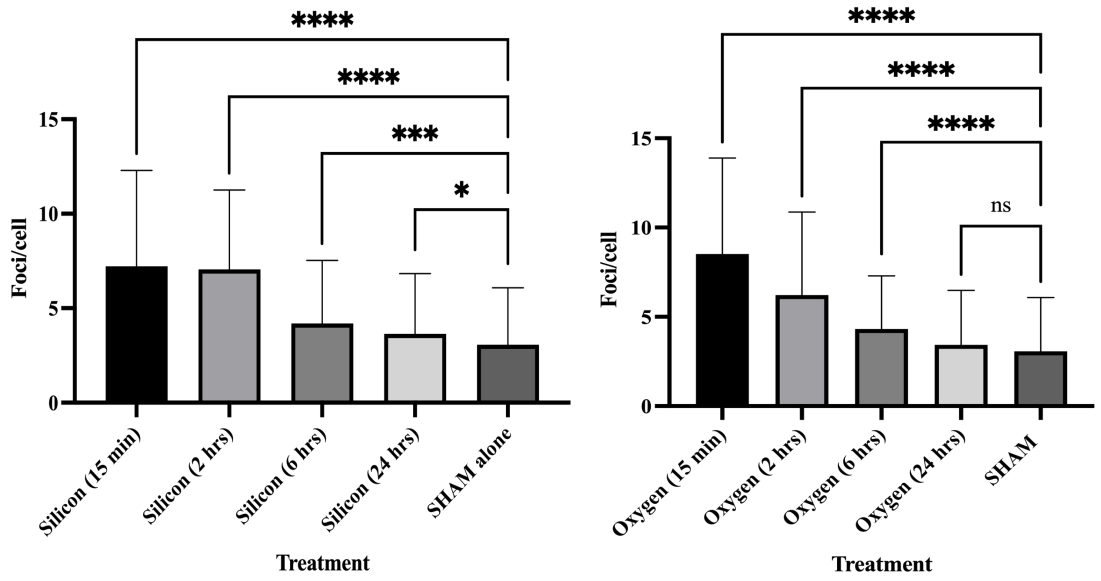

Figure A.4.1: DNA damage foci counts of Si-28 (50 cGy) and O-16 (50 cGy) when fixed 15 min-24 hours after ionizing radiation exposures. Shown are the gamma H2AX/53BP1 overlapping foci/cell averages with standard deviation. Analysis is One-way ANOVA with Dunnett's multiple comparisons test (all groups compared to SHAM). Quantification of the foci counts in all IR groups can be found in the Appendix (Table A.4.1).

Gamma (50 cGy)					
	15 min	2 hrs	6 hrs	24 hrs	SHAM
Mean	8.987	7.07	4.781	3.734	3.07
Std. Deviation	7.247	4.569	3.619	3.02	3.013
Std. Error of Mean	0.415	0.2045	0.1573	0.1383	0.09048
Number of values	305	499	529	477	1109
Proton (50 cGy)					
	15 min	2 hrs	6 hrs	24 hrs	SHAM
Mean	10.18	3.93	3.117	3.275	3.07
Std. Deviation	5.36	3.305	2.856	2.687	3.013
Std. Error of Mean	0.3951	0.2638	0.2129	0.2124	0.09048
Number of values	184	157	180	160	1109
Fe (50 cGy)					
	15 min	2 hrs	5 hrs	24 hrs	SHAM
Mean	6.644	5.504	4.147	3.582	3.07
Std. Deviation	4.425	3.865	3.11	3.24	3.013
Std. Error of Mean	0.2389	0.2051	0.1704	0.1803	0.09048
Number of values	343	355	333	323	1109
GCR (75 cGy)					
	15 min	2 hrs	6 hrs	24 hrs	SHAM
Mean	10.74	6.991	3.605	3.114	3.07
Std. Deviation	6.904	5.082	3.179	2.67	3.013
Std. Error of Mean	0.2598	0.195	0.1968	0.1156	0.09048
Number of values	706	679	261	533	1109
Silicon (50 cGy)					
	15 min	2 hrs	6 hrs	24 hrs	SHAM
Mean	7.218	7.058	4.187	3.639	3.07
Std. Deviation	5.075	4.196	3.329	3.192	3.013
Std. Error of Mean	0.2346	0.1917	0.2337	0.1445	0.09048
Number of values	468	479	203	488	1109
Oxygen (50 cGy)					
	15 min	2 hrs	6 hrs	24 hrs	SHAM
Mean	8.518	6.222	4.322	3.435	3.07
Std. Deviation	5.378	4.646	2.976	3.043	3.013
Std. Error of Mean	0.2316	0.1992	0.1641	0.1338	0.09048
Number of values	539	544	329	517	1109

Table A.4.1: Raw average (mean) gamma H2AX/53BP1 overlapping foci/cell with SD in cells treated with IR alone. ***Note: The number of values refers to number of cells counted at each fixation time point.***

IR	Dose (cGy)	Time point	Average foci/cell	Induced foci/cell	Induced foci/cGy
Oxygen	50	15 min	8.5	5.4	0.109
Silicon	50	15 min	7.2	4.1	0.083

Table A.4.2: Induced DNA DSB foci kinetics on human MRC-5 fibroblasts treated with Oxygen or Silicon IR-alone.

IR type	Dose (cGy)	Up-regulated DEG	Down-regulated DEG	Total DEG
Oxygen	50	11	53	64
Silicon	50	32	71	103

Table A.4.3: Total numbers of differentially expressed genes in silicon and oxygen irradiated samples as determined via RNA sequencing.

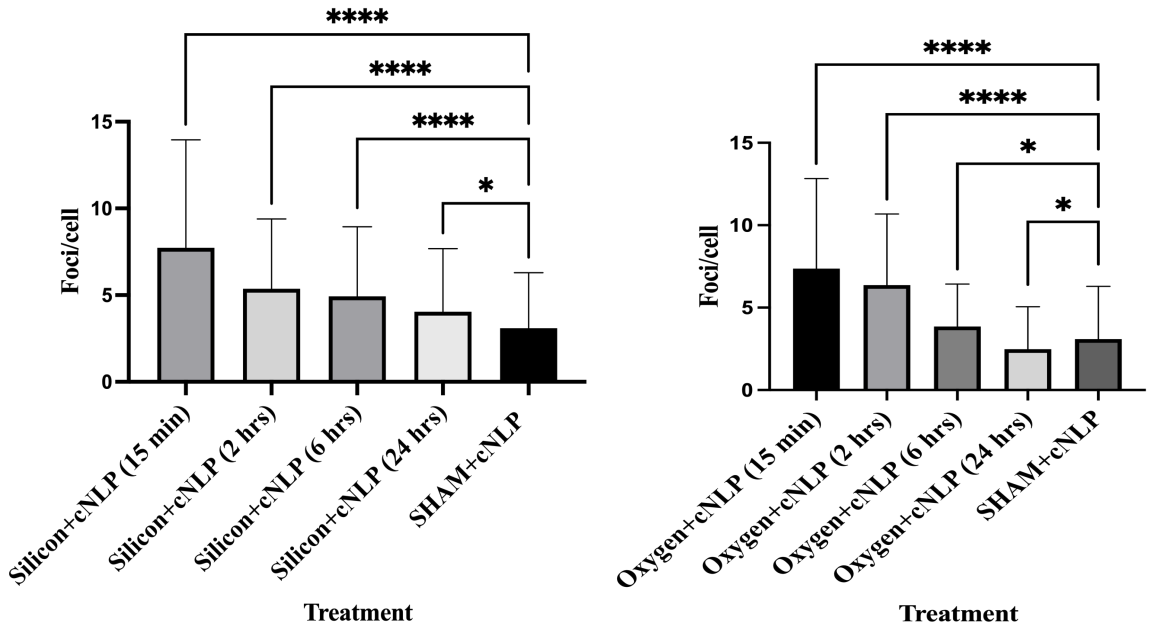

Figure A.4.2: DNA damage foci counts of Si-28+cNLP (50 cGy) and O-16+cNLP (50 cGy) radioprotection treatment when fixed 15 min-24 hours after ionizing radiation exposures. Shown are the gamma H2AX/53BP1 overlapping foci/cell averages with standard deviation. Analysis is One-way ANOVA with Dunnett's multiple comparisons test (all groups compared to SHAM). Quantification of the foci counts in all IR groups+cNLP can be found in the Appendix (Table A.4.4).

Gamma (50 cGy)+cNLP					
	15 min	2 hrs	6 hrs	24 hrs	SHAM +cNLP
Mean	7.462	7.4	5.186	3.316	3.089
Std. Deviation	6.936	6.001	4.303	3.173	3.205
Std. Error of Mean	0.3024	0.2607	0.1915	0.1438	0.1029
Number of values	526	530	505	487	970

Proton (50 cGy)+cNLP					
	15 min	2 hrs	6 hrs	24 hrs	SHAM +cNLP
Mean	9.689	3.193	3.216	3.519	3.089
Std. Deviation	6.033	3.047	3.137	3.901	3.205
Std. Error of Mean	0.4711	0.2488	0.2536	0.3065	0.1029
Number of values	164	150	153	162	970

Fe (50 cGy)+cNLP					
	15 min	2 hrs	5 hrs	24 hrs	SHAM +cNLP
Mean	5.889	4.555	3.661	3.324	3.089
Std. Deviation	3.52	3.198	2.601	2.259	3.205
Std. Error of Mean	0.2502	0.2314	0.2007	0.1675	0.1029
Number of values	198	191	168	182	970

GCR (75 cGy)+cNLP					
	15 min	2 hrs	6 hrs	24 hrs	SHAM +cNLP
Mean	11.5	8.018	6.99	6.101	3.089
Std. Deviation	10.46	7.885	6.215	4.156	3.205
Std. Error of Mean	0.9668	0.7385	0.6065	0.4676	0.1029
Number of values	117	114	105	79	970

Silicon (50 cGy)+cNLP					
	15 min	2 hrs	6 hrs	24 hrs	SHAM +cNLP
Mean	7.726	5.369	4.935	4.039	3.089
Std. Deviation	6.226	4.02	4.014	3.639	3.205
Std. Error of Mean	0.5359	0.3178	0.3087	0.2932	0.1029
Number of values	135	160	169	154	970

Oxygen (50 cGy)+cNLP					
	15 min	2 hrs	6 hrs	24 hrs	SHAM +cNLP
Mean	7.373	6.369	3.86	2.48	3.089
Std. Deviation	5.464	4.315	2.567	2.581	3.205
Std. Error of Mean	0.2985	0.23	0.2004	0.1166	0.1029
Number of values	335	352	164	490	970

Table A.4.4: Raw average (Mean) gamma H2AX/53BP1 overlapping foci/cell with SD in cells treated with IR +cNLP radioprotective treatment.

Treatment	Dose (cGy)	Time point	Average foci/cell	Induced foci/cell	Induced foci/cGy
Oxygen	50	15 min	8.5	5.4	0.109
Oxygen+cNLP	50	15 min	7.4*	4.3	0.086
Silicon	50	15 min	7.2	4.1	0.083
Silicon+cNLP	50	15 min	7.7	4.6	0.093

Table A.4.5: Comparison of induced DNA DSB foci kinetics on human MRC-5 fibroblasts treated with O-16 or Si-28 IR alone or IR+cNLP radiation protection treatment. *Note: *Oxygen+cNLP foci counts were significantly different than Oxygen IR alone at the 15-minute time point as determined by One-Way ANOVA with Turkey's multiple comparisons test ($p<0.01$).*

Treatment	Dose (cGy)	Up-regulated DEG	Down-regulated DEG	Total DEG
SHAM+cNLP	0	252	516	768
Gamma+cNLP	100	69	161	230
Proton+cNLP	100	131	304	435
Fe+cNLP	50	343	826	1169
GCR+cNLP	75	429	478	907
Oxygen+cNLP	50	363	896	1259
Silicon+cNLP	50	683	612	1295

Table A.4.6: Total numbers of differentially expressed genes in all irradiated samples with cNLP radioprotection treatment as determined via RNA sequencing.

Biological pathway	GCR+cNLP	Differentially Expressed Genes
hsa04114:Oocyte meiosis	✓	CAMK2B, PLK1, ADCY4, IGF1, PKMYT1, CDC25C, SGO1, CDC20, CCNB2, CCNB1, PTTG1, CDK1, BUB1, MAD2L1
hsa04914:Progesterone-mediated oocyte maturation	✓	CCNA2, CCNB2, CCNB1, PLK1, ADCY4, CDK1, IGF1, PKMYT1, CDC25C, BUB1, MAD2L1, PIK3R5
hsa05410:Hypertrophic cardiomyopathy (HCM)	✓	TGFB2, ACTC1, PRKAA2, TNNT2, ITGA2, ITGB3, TPM1, ITGA1, ITGA7, DMD, IGF1
hsa02010:ABC transporters	✓	ABCC3, ABCB1, ABCA6, ABCA7, ABCA8, ABCA13, ABCG1
hsa00350:Tyrosine metabolism	✓	ALDH1A3, ADH1C, ADH1B, ADH1A, TYRP1, AOX1
hsa05214:Glioma	✓	CAMK2B, SHC4, SHC2, PDGFB, E2F1, E2F2, IGF1, PIK3R5
hsa05206:MicroRNAs in cancer	✓	SHC4, TGFB2, TNXB, ABCB1, ITGB3, CDCA5, TPM1, PDGFB, IRS2, CDC25C, THBS1, BCL2L11, SOCS1, ERBB3, PLAU, E2F1, TIMP3, E2F2, HMOX1, BMF
hsa04514:Cell adhesion molecules (CAMs)	✓	CLDN11, CNTNAP2, CLDN20, PTPRC, CDH2, ITGB2, NRXN3, ESAM, CLDN1, HLA-DOB, NECTIN3, ICOSLG
hsa05166:HTLV-I infection	✓	TGFB2, CDKN2B, WNT2B, CSF2, WNT7B, ITGB2, PDGFB, ADCY4, FZD8, BUB1B, PIK3R5, CDC20, WNT11, PTTG1, E2F1, E2F2, HLA-DOB, MAD2L1
hsa04930:Type II diabetes mellitus	✓	SOCS1, CACNA1A, IRS2, SLC2A4, CACNA1G, PIK3R5
hsa04916:Melanogenesis	✓	CAMK2B, EDN1, WNT11, WNT2B, WNT7B, KIT, TYRP1, ADCY4, FZD8
hsa00982:Drug metabolism - cytochrome P450	✓	ALDH1A3, ADH1C, ADH1B, ADH1A, AOX1, FMO2, CYP3A5
hsa04650:Natural killer cell mediated cytotoxicity	✓	SHC4, ZAP70, SHC2, CSF2, ITGB2, TNFSF10, PTPN6, ULBP2, ULBP1, PIK3R5
hsa05134:Legionellosis	✓	CXCL8, BNIP3, ITGB2, HSPA6, IL12A, CXCL2
hsa05218:Melanoma	✓	FGF17, PDGFB, E2F1, E2F2, IGF1, FGF11, PIK3R5
hsa04960:Aldosterone-regulated sodium reabsorption	✓	ATP1A3, NEDD4L, IGF1, NR3C2, PIK3R5
hsa05033:Nicotine addiction	✓	GABRB1, GRIN3B, CACNA1A, GRIN2C, GRIA4

Table A.4.7: Biological pathways hits impacted by differentially expressed genes in GCR+cNLP radioprotection treatment group that were not found in GCR alone groups.

Treatment	Dose (cGy)	Up-regulated DEG	Down-regulated DEG	Total DEG
SHAM+cNLP RM	0	1158	1384	2542
Gamma+cNLP RM	100	313	320	633
Proton+cNLP RM	100	274	282	556
Fe+cNLP RM	50	567	823	1390
GCR+cNLP RM	75	444	405	849
Oxygen+cNLP RM	50	344	515	859
Silicon+cNLP RM	50	502	248	750

Table A.4.8: Total numbers of differentially expressed genes in all irradiated samples with cNLP mitigation treatment as determined via RNA sequencing.

Figure A.4.3: Transcriptional analysis on DNA damage and antioxidant response genes following IR exposures (with and without curcumin treatment). All groups with DMSO were normalized to SHAM (DMSO) treatment. All groups without DMSO were normalized to SHAM (no DMSO) treatment. GAPDH was used as the normalizer gene across all samples.

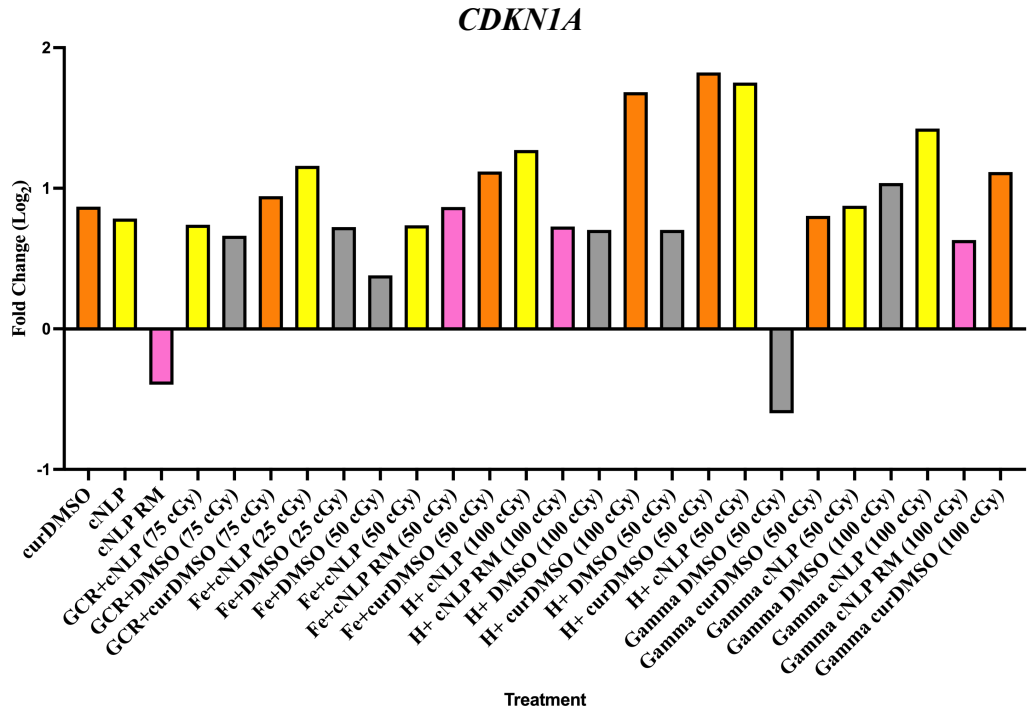

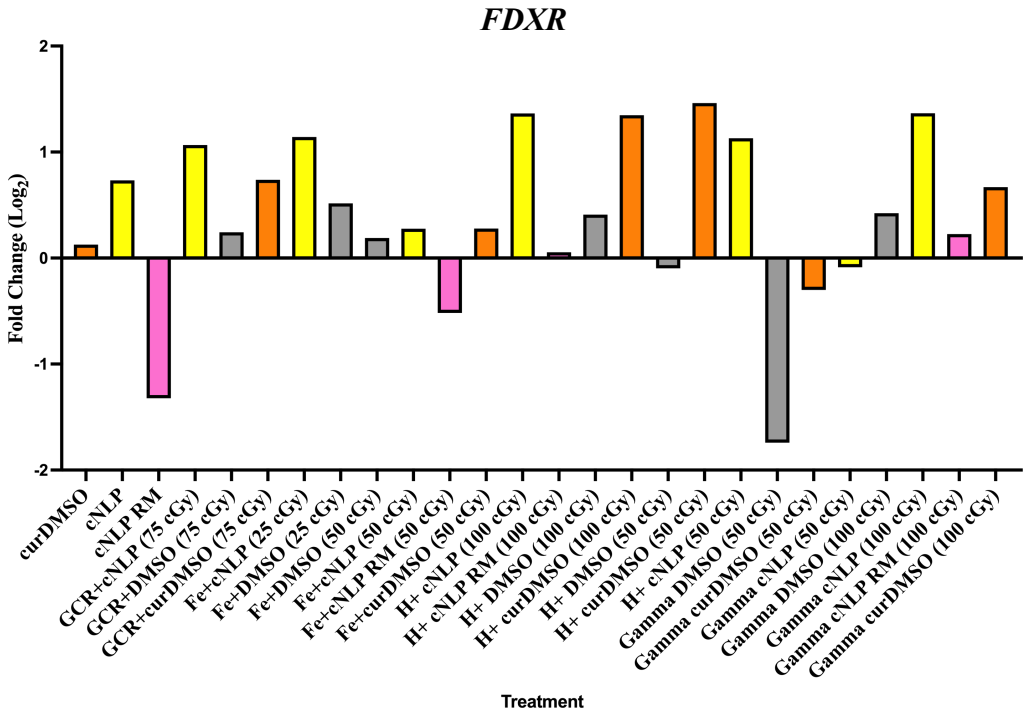

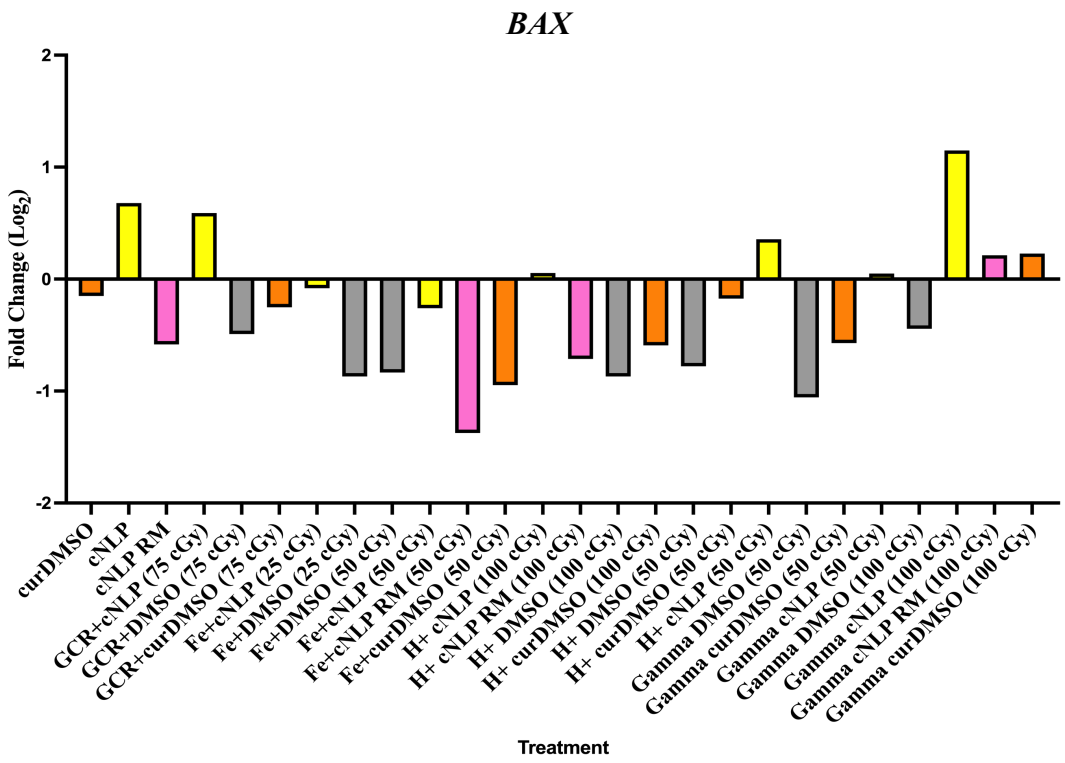
BAX
Fold Change (Log2)
2
1
0
-1
-2
curDMSO
cNLP
cNLP RM
GCR+cNLP (75 cGy)
GCR+DMSO (75 cGy)
GCR+curDMSO (75 cGy)
Fe+cNLP (25 cGy)
Fe+DMSO (25 cGy)
Fe+cNLP (50 cGy)
Fe+DMSO (50 cGy)
Fe+cNLP RM (50 cGy)
Fe+curDMSO (50 cGy)
H+ cNLP (100 cGy)
H+ cNLP RM (100 cGy)
H+ DMSO (100 cGy)
H+ curDMSO (100 cGy)
H+ cNLP (50 cGy)
H+ DMSO (50 cGy)
H+ curDMSO (50 cGy)
Gamma cNLP (50 cGy)
Gamma curDMSO (50 cGy)
Gamma DMSO (50 cGy)
Gamma cNLP (100 cGy)
Gamma DMSO (100 cGy)
Gamma cNLP RM (100 cGy)
Gamma curDMSO (100 cGy)
Treatment

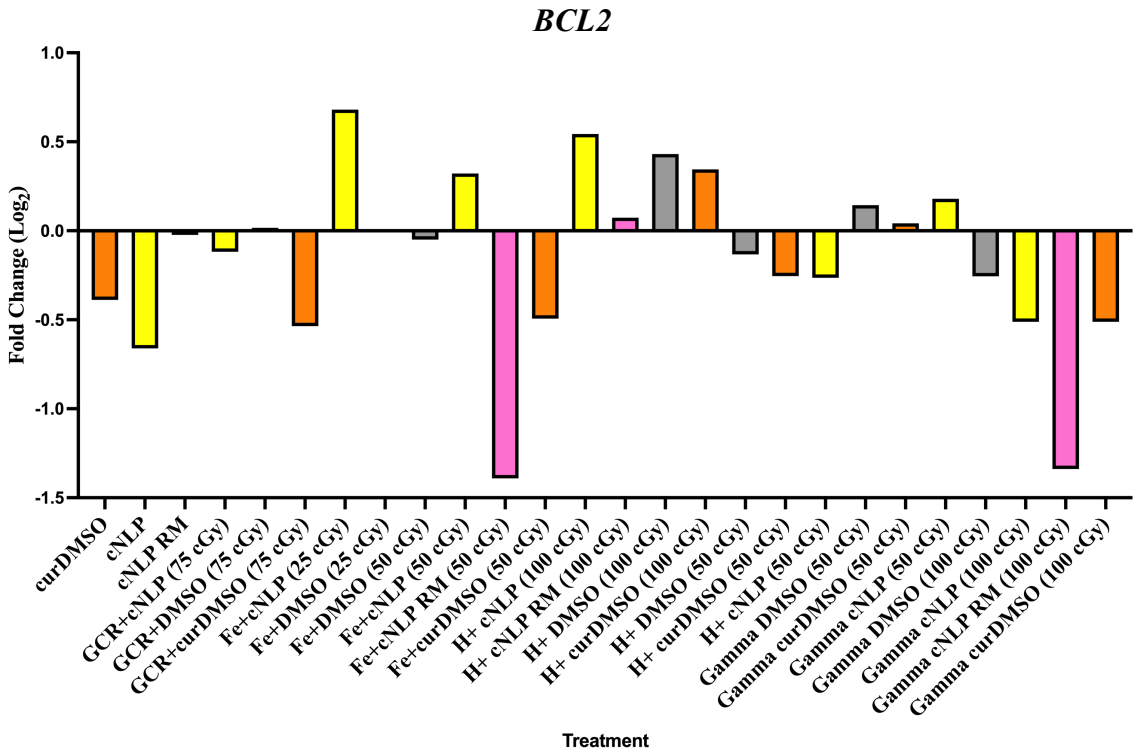
BCL2
Fold Change (Log2)
1.0
0.5
0.0
-0.5
-1.0
-1.5
curDMSO
cNLP
cNLP RM
GCR+cNLP (75 cGy)
GCR+DMSO (75 cGy)
GCR+curDMSO (75 cGy)
Fe+cNLP (25 cGy)
Fe+DMSO (25 cGy)
Fe+cNLP (50 cGy)
Fe+DMSO (50 cGy)
Fe+cNLP RM (50 cGy)
Fe+curDMSO (50 cGy)
H+ cNLP (100 cGy)
H+ cNLP RM (100 cGy)
H+ DMSO (100 cGy)
H+ curDMSO (100 cGy)
H+ DMSO (50 cGy)
H+ curDMSO (50 cGy)
H+ cNLP (50 cGy)
Gamma DMSO (50 cGy)
Gamma curDMSO (50 cGy)
Gamma cNLP (50 cGy)
Gamma DMSO (100 cGy)
Gamma cNLP (100 cGy)
Gamma cNLP RM (100 cGy)
Gamma curDMSO (100 cGy)
Treatment

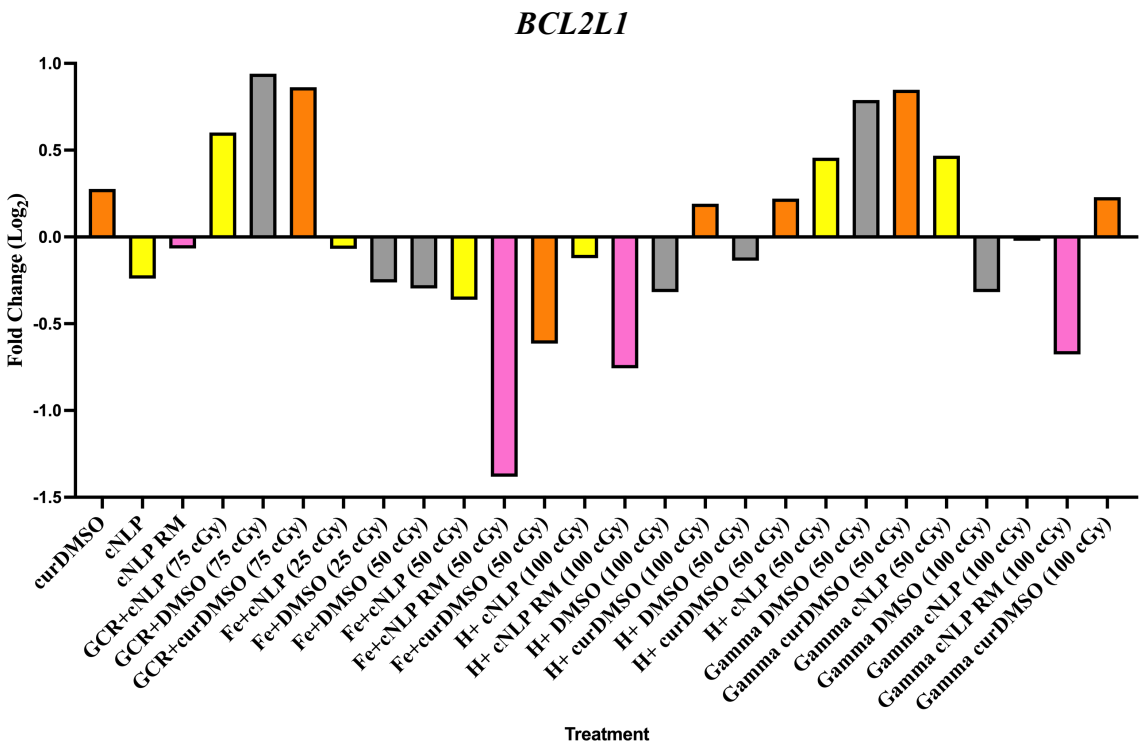
BCL2L1
Fold Change (Log2)
1.0
0.5
0.0
-0.5
-1.0
-1.5
curDMSO
cNLP
cNLP RM
GCR+cNLP (75 cGy)
GCR+DMSO (75 cGy)
GCR+curDMSO (75 cGy)
Fe+cNLP (25 cGy)
Fe+DMSO (25 cGy)
Fe+DMSO (50 cGy)
Fe+cNLP (50 cGy)
Fe+cNLP RM (50 cGy)
Fe+curDMSO (50 cGy)
H+ cNLP (100 cGy)
H+ cNLP RM (100 cGy)
H+ DMSO (100 cGy)
H+ curDMSO (100 cGy)
H+ DMSO (50 cGy)
H+ curDMSO (50 cGy)
H+ cNLP (50 cGy)
Gamma DMSO (50 cGy)
Gamma curDMSO (50 cGy)
Gamma cNLP (50 cGy)
Gamma DMSO (100 cGy)
Gamma cNLP (100 cGy)
Gamma cNLP RM (100 cGy)
Gamma curDMSO (100 cGy)
Treatment

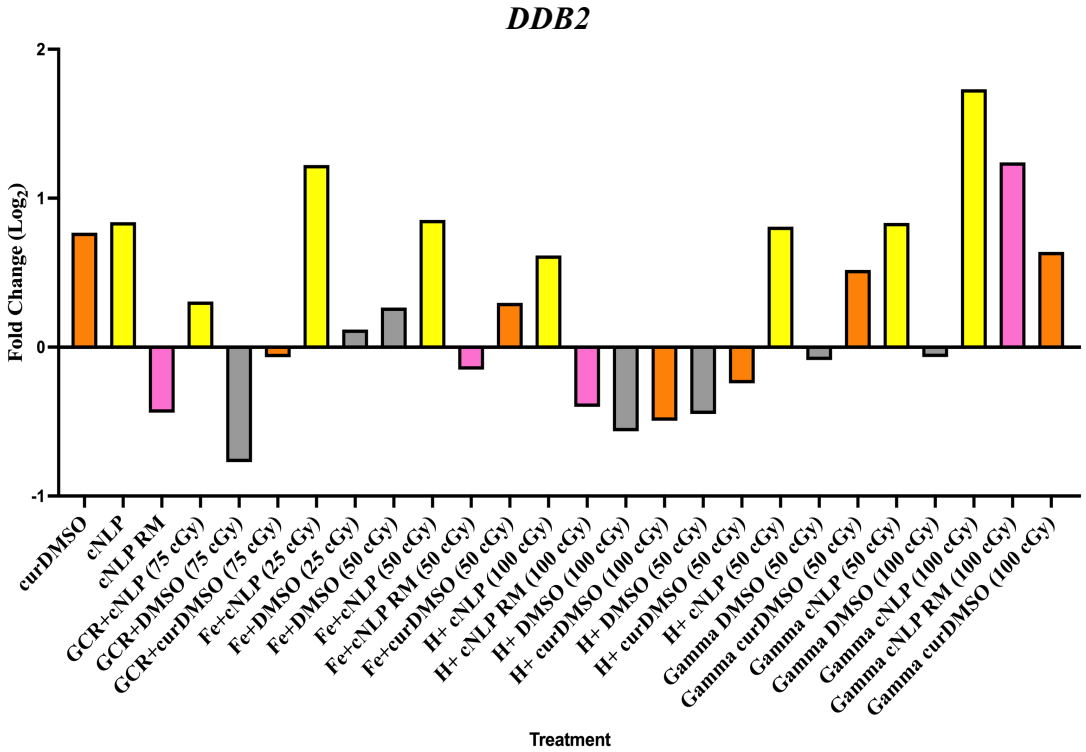
DDB2
Fold Change (Log2)
2
1
0
-1
curDMSO
cNLP
cNLP RM
GCR+cNLP (75 cGy)
GCR+DMSO (75 cGy)
GCR+curDMSO (75 cGy)
Fe+cNLP (25 cGy)
Fe+DMSO (25 cGy)
Fe+DMSO (50 cGy)
Fe+cNLP (50 cGy)
Fe+cNLP RM (50 cGy)
Fe+curDMSO (50 cGy)
H+ cNLP (100 cGy)
H+ cNLP RM (100 cGy)
H+ DMSO (100 cGy)
H+ curDMSO (100 cGy)
H+ DMSO (50 cGy)
H+ curDMSO (50 cGy)
H+ cNLP (50 cGy)
Gamma DMSO (50 cGy)
Gamma curDMSO (50 cGy)
Gamma cNLP (50 cGy)
Gamma DMSO (100 cGy)
Gamma cNLP (100 cGy)
Gamma cNLP RM (100 cGy)
Gamma curDMSO (100 cGy)
Treatment

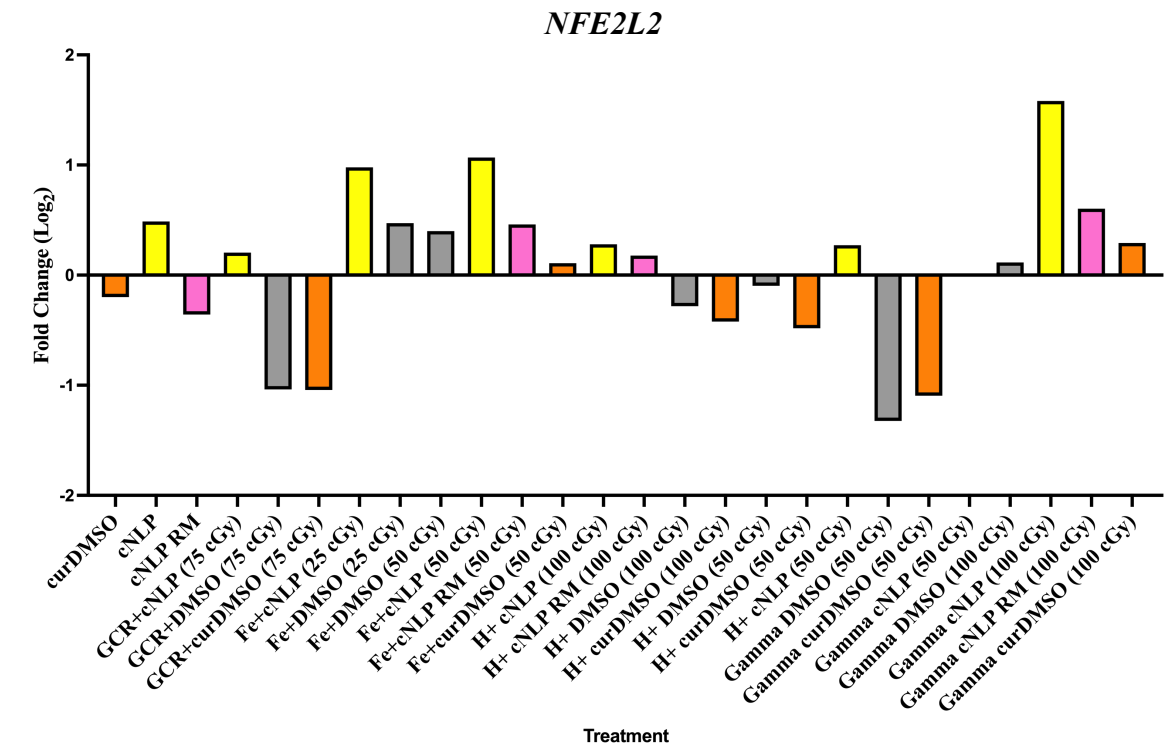
NFE2L2
Fold Change (Log2)
2
1
0
-1
-2
curDMSO
cNLP
cNLP RM
GCR+cNLP (75 cGy)
GCR+DMSO (75 cGy)
GCR+curDMSO (75 cGy)
Fe+cNLP (25 cGy)
Fe+DMSO (25 cGy)
Fe+DMSO (50 cGy)
Fe+cNLP (50 cGy)
Fe+cNLP RM (50 cGy)
Fe+curDMSO (50 cGy)
H+ cNLP (100 cGy)
H+ cNLP RM (100 cGy)
H+ DMSO (100 cGy)
H+ curDMSO (100 cGy)
H+ DMSO (50 cGy)
H+ curDMSO (50 cGy)
H+ cNLP (50 cGy)
Gamma DMSO (50 cGy)
Gamma curDMSO (50 cGy)
Gamma cNLP (50 cGy)
Gamma DMSO (100 cGy)
Gamma cNLP (100 cGy)
Gamma cNLP RM (100 cGy)
Gamma curDMSO (100 cGy)
Treatment

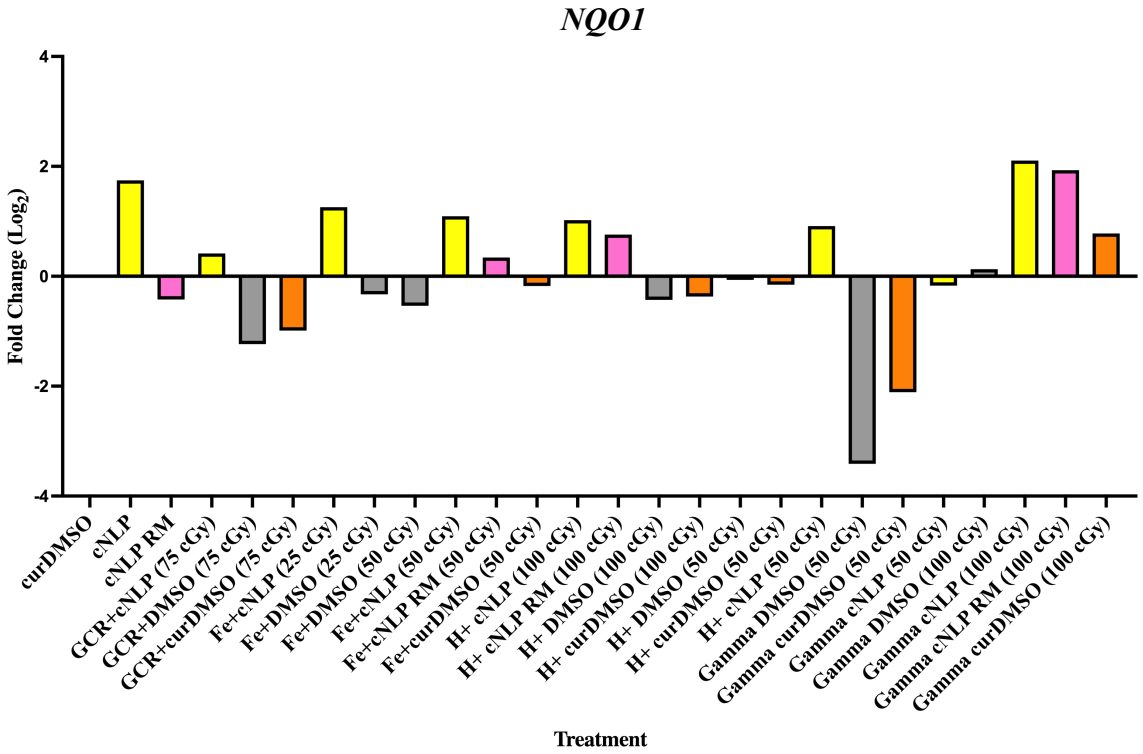
NQO1
Fold Change (Log2)
4
2
0
-2
-4
curDMSO
cNLP
cNLP RM
GCR+cNLP (75 cGy)
GCR+DMSO (75 cGy)
GCR+curDMSO (75 cGy)
Fe+cNLP (25 cGy)
Fe+DMSO (25 cGy)
Fe+DMSO (50 cGy)
Fe+cNLP (50 cGy)
Fe+cNLP RM (50 cGy)
Fe+curDMSO (50 cGy)
H+ cNLP (100 cGy)
H+ cNLP RM (100 cGy)
H+ DMSO (100 cGy)
H+ curDMSO (100 cGy)
H+ DMSO (50 cGy)
H+ curDMSO (50 cGy)
H+ cNLP (50 cGy)
Gamma DMSO (50 cGy)
Gamma curDMSO (50 cGy)
Gamma cNLP (50 cGy)
Gamma DMSO (100 cGy)
Gamma cNLP (100 cGy)
Gamma cNLP RM (100 cGy)
Gamma curDMSO (100 cGy)
Treatment

KEAP1

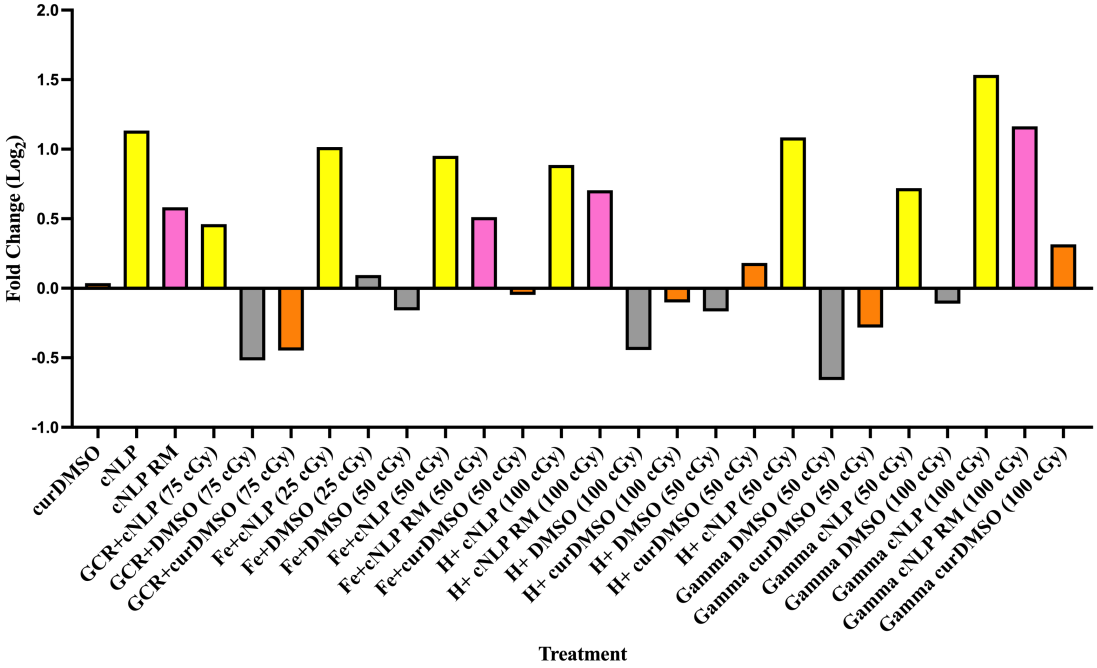
Fold Change (Log2)
2.0
1.5
1.0
0.5
0.0
-0.5
-1.0
curDMSO
cNLP
cNLP RM
GCR+cNLP (75 cGy)
GCR+DMSO (75 cGy)
GCR+curDMSO (75 cGy)
Fe+cNLP (25 cGy)
Fe+DMSO (25 cGy)
Fe+DMSO (50 cGy)
Fe+cNLP (50 cGy)
Fe+cNLP RM (50 cGy)
Fe+curDMSO (50 cGy)
H+ cNLP (100 cGy)
H+ cNLP RM (100 cGy)
H+ DMSO (100 cGy)
H+ curDMSO (100 cGy)
H+ DMSO (50 cGy)
H+ curDMSO (50 cGy)
H+ cNLP (50 cGy)
Gamma DMSO (50 cGy)
Gamma curDMSO (50 cGy)
Gamma cNLP (50 cGy)
Gamma DMSO (100 cGy)
Gamma cNLP (100 cGy)
Gamma cNLP RM (100 cGy)
Gamma curDMSO (100 cGy)
Treatment

HMOX1

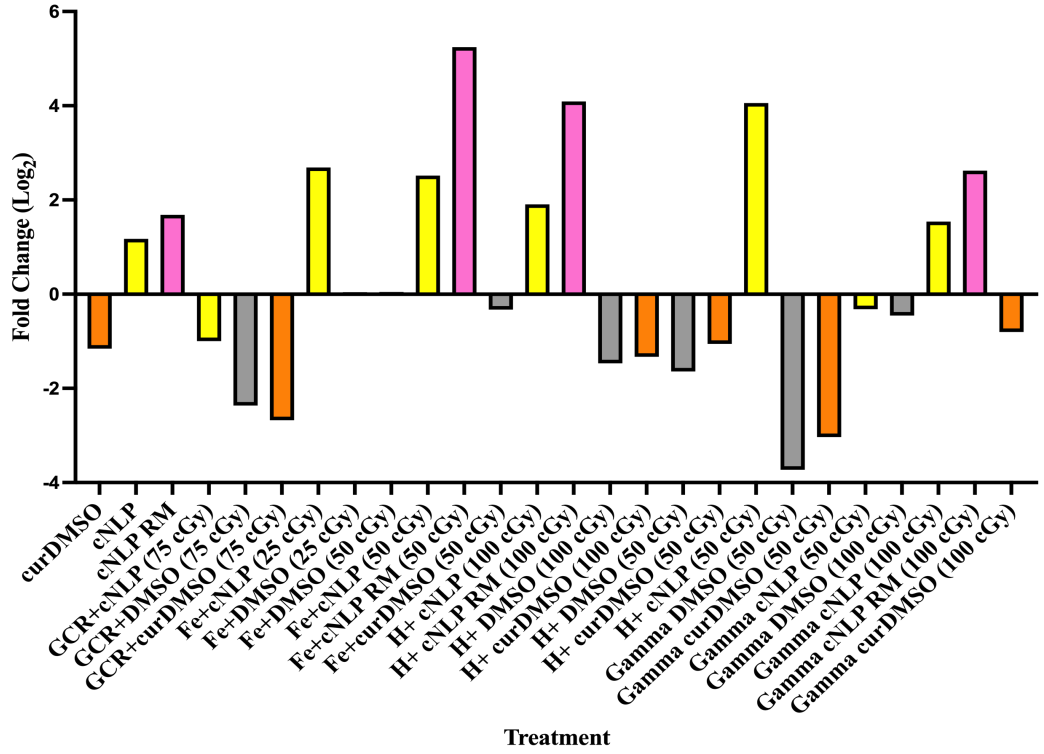
Fold Change (Log2)
6
4
2
0
-2
-4
curDMSO
cNLP
cNLP RM
GCR+cNLP (75 cGy)
GCR+DMSO (75 cGy)
GCR+curDMSO (75 cGy)
Fe+cNLP (25 cGy)
Fe+DMSO (25 cGy)
Fe+DMSO (50 cGy)
Fe+cNLP (50 cGy)
Fe+cNLP RM (50 cGy)
Fe+curDMSO (50 cGy)
H+ cNLP (100 cGy)
H+ cNLP RM (100 cGy)
H+ DMSO (100 cGy)
H+ curDMSO (100 cGy)
H+ DMSO (50 cGy)
H+ curDMSO (50 cGy)
H+ cNLP (50 cGy)
Gamma DMSO (50 cGy)
Gamma curDMSO (50 cGy)
Gamma cNLP (50 cGy)
Gamma DMSO (100 cGy)
Gamma cNLP (100 cGy)
Gamma cNLP RM (100 cGy)
Gamma curDMSO (100 cGy)
Treatment

Chapter 5: Summary

5.1 Conclusions

This dissertation describes the biological effects following various qualities of ionizing radiation as seen through the lens of the human transcriptome. Throughout this work, we tested the gene expression fluctuations induced through various qualities of ionizing radiation exposures (low and high-LET components), validated targeted gene expression within the p53 and Nrf2-ARE pathways, and identified DNA damage and DNA repair alterations based on the presence or absence of curcumin NLPs as radiation medical countermeasures.

In Chapter 2, exposures to ^{131}I in children undergoing radiation therapy for high-risk neuroblastoma resulted in gene expression fluctuations that can be seen in the peripheral blood out to 15 days post-treatment. This chapter expanded upon our previously published biodosimetry panel of transcripts (Edmondson et al., 2016) and identified novel peripheral blood biomarkers responding to ^{131}I treatment up to 2 weeks after a single radionuclide injection. This data validated that patients serve as a unique model system of ^{131}I exposures and also that previously studied biomarkers of external IR exposures can be applied to internal exposures of ^{131}I between 3 and 15 days after treatment. Moreover, our radiation-responsive biomarker panel can differentiate between ~2 Gy exposures and unexposed individuals out to 15 days which may be useful for biodosimetry purposes and medical triage after an unwarranted nuclear incident, such as a dirty bomb. Clinically, it also may identify biomarkers corresponding to patient outcome, in this case children with high-risk neuroblastoma, following his or her IR therapy regimen.

In Chapter 3, we explored curcumin, a natural anti-inflammatory and antioxidant polyphenol, as an additive nutripharmaceutical solubilized within a nanodisc environment and showed that curcumin NLPs (cNLPs) improved curcumin bioavailability within a human fibroblast cell line

model system. We then explored the novel application of using these cNLPs as a radiological protectant *in vitro*. We found that although the range of protection enhancement varied by dose, importantly, the cNLPs demonstrated radioprotection over empty NLP discs and curcumin dissolved in DMSO following up to 6 Gy gamma IR exposures. This chapter serves to showcase the feasibility and ease by which a new antioxidant-loaded NLP can be made along with revealing a new application for curcumin NLPs to be used as radiation countermeasure agents. These findings may serve as models for exploring additional antioxidant-loaded NLPs against radiation exposures *in vitro* or against various tissue targets of interest *in vivo*.

Throughout the final data-rich chapter of my dissertation (Chapter 4), I described how environmental radiation exposures in space are comprised of complex mixtures of IR species and may prove detrimental to human health throughout a long-term Mars mission. Within Chapter 4, I outlined differences in the transcriptomic responses of normal human fibroblasts following simulated galactic cosmic radiation (GCR) exposures with and without curcumin NLP radiation protection or radiation mitigation treatments. Furthermore, I also compared the transcriptomic responses following GCR exposures to additional IR qualities relevant to deep space flight, including HZE Fe-56 particles as well as low-LET proton ions and standard-of-care gamma rays. Within this chapter, I demonstrated that curcumin NLPs show promise as radiological countermeasures which may act through mechanisms involving oxidative stress response, cell cycle arrest, and apoptosis. This study is unique in that it appears to be the first study reporting transcriptomic alterations in normal human fibroblasts following NSRL's simulated 5-ion GCR simulator beam along with direct comparison to additional high and low-LET ion species. Moreover, this is the first study demonstrating that cNLPs may serve as effective biological countermeasures against space relevant IR exposures.

5.2 Impact of this work

This dissertation describes the gene expression fluctuations following a range of ionizing radiation exposures in humans and human cell lines as it pertains to radiation therapy treatment or environmental exposures throughout deep space. Moreover, we have demonstrated a safe and effective curcumin-loaded NLP which may, in theory, serve as a safe and effective countermeasure against these IR-induced toxicities in humans.

In principle, this data may serve as a model that can also be applied to other DNA damaging agents other than radiation, as well as epigenetic alterations that may ultimately impact the human transcriptome and result in biological damage over time. Taken together, this data supports the idea that humans may benefit from deriving additional natural product-based therapies to protect against other stressors of interest (environmental toxins, drug side effects, inflammation, and aging) that currently impact humans worldwide. Moreover, natural products provide health benefits that can be used for youth and adults alike, and these benefits may also transcend beyond Earth's atmosphere for use during human space travel.

5.3 Next Steps

Utilizing gene expression methodology is a robust and high-throughput technique that can be informative for biodosimetry estimation, biological pathway perturbation, or identifying downstream mechanisms at play following ionizing radiation exposures. Within the context of the clinical neuroblastoma patient project, the next steps include combining our gene expression findings within the context of the entire patient clinical dataset. This data may inform biomarkers associated with outcome and potentially improve the standard-of-care for future high-risk neuroblastoma patient cohorts.

Regarding the cNLP studies, the solubility and characterization techniques applied in the context of curcumin NLPs can be optimized for additional antioxidant molecules of interest which may prove useful in decreasing disease burden within the context of radiation protection or mitigation. Future directions may also include performing proteomic analyses on curcumin NLP exposed samples in ≥2 normal human cell lines to validate Nrf2-ARE pathways, anti-inflammatory responses, and p53 pathway modulation with respect to radiation protection or radiation mitigation treatments. Moreover, examining various routes of exposure of curcumin NLPs in the context of animal model systems *in vivo*, including parenteral or oral administration, may provide insight to curcumin metabolic processes, cell targeting, or radioprotective abilities within various tissues of interest.

Importantly, the methods of utilizing antioxidant-loaded nanodiscs as countermeasures to IR exposures may also be studied against additional biological stressors of interest, such as environmental toxins or endogenous stressors, that result in DNA damage or unwanted side effects in humans. In theory, the methods used for solubilizing antioxidant-rich curcumin within an NLP can be optimized for multiple antioxidant compounds of interest. These antioxidant-loaded NLPs may also serve as protection agents against excess oxidative stress induced throughout daily life, such as environmental triggers or hyperactive immune responses and inflammatory reactions, as is seen in humans with autoimmune diseases. Although my studies did not address the impact of curcumin NLPs on inflammation specifically, it would be interesting to test the impact of cNLPs on endogenous stressors, such as autoimmune diseases, chronic inflammation, and aging, as a corollary dataset to our findings following exogenous exposures to ionizing radiation.